2-2009

The Role of Stellar Feedback in Galaxy Evolution

Li Zhiyuan

University of Massachusetts Amherst, zyli@astro.umass.edu

THE ROLE OF STELLAR FEEDBACK IN GALAXY EVOLUTION

A Dissertation Presented

by

ZHIYUAN LI

Submitted to the Graduate School of the
University of Massachusetts Amherst in partial fulfillment
of the requirements for the degree of

DOCTOR OF PHILOSOPHY

February 2009

Astronomy

THE ROLE OF STELLAR FEEDBACK IN GALAXY EVOLUTION

A Dissertation Presented

by

ZHIYUAN LI

Approved as to style and content by:

_____

Q. Daniel Wang, Chair

_____

Laura Cadonati, Member

_____

Neal S. Katz, Member

_____

Stephen E. Schneider, Member

_____

Ronald L. Snell, Department Chair
Astronomy

To my family

ACKNOWLEDGMENTS

ABSTRACT

THE ROLE OF STELLAR FEEDBACK IN GALAXY EVOLUTION

FEBRUARY 2009

ZHIYUAN LI

B.Sc., NANJING UNIVERSITY

M.Sc., NANJING UNIVERSITY

Ph.D., UNIVERSITY OF MASSACHUSETTS AMHERST

Directed by: Professor Q. Daniel Wang

Aiming at understanding the role of stellar feedback in galaxy evolution, I present a study of the hot interstellar medium in several representative galaxies, based primarily on X-ray observations as well as theoretical modelling.

I find that, in the massive disk galaxies NGC2613 and M104, the observed amount of hot gas is much less than that predicted by current galaxy formation models. Such a discrepancy suggests a lack of appropriate treatments of stellar/AGN feedback in these models.

I also find that stellar feedback, primarily in the form of mass loss from evolved stars and energy released from supernovae, and presumably consumed by the hot gas, is largely absent from the inner regions of M104, a galaxy of a substantial content of evolved stars but little current star formation. A natural understanding of this phenomenon is that the hot gas is in the form of a galactic-scale outflow, by which

the bulk of the stellar feedback is transported to the outer regions and perhaps into the intergalactic space. A comparison between the observed sub-galactic gas structures and model predictions indicate that this outflow is probably subsonic rather than being a classical supersonic galactic wind. Such outflows are likely prevalent in most early-type galaxies of intermediate masses in the present-day universe and thus play a crucial role in the evolution of such galaxies.

For the first time I identify the presence of diffuse hot gas in and around the bulge of the Andromeda Galaxy (M31), our well-known neighbor. Both the morphology and energetics of the hot gas suggest that it is also in the form of a large-scale outflow.

Assisted with multiwavelength observations toward the circumnuclear regions of M31, I further reveal the relation between the hot gas and other cooler phases of the interstellar medium. I suggest that thermal evaporation, mostly likely energized by Type Ia supernovae, acts to continuously turn cold gas into hot, a process that naturally leads to the inactivity of the central supermassive blackhole as well as the launch of the hot gas outflow. Such a mechanism plays an important role in regulating the multi-phase interstellar medium in the circumnuclear environment and transporting stellar feedback to the outer galactic regions.

TABLE OF CONTENTS

LIST OF TABLES

LIST OF FIGURES

xvii

CHAPTER 1

INTRODUCTION

In this general introduction I aim to outline the scientific background, methodology and content of my dissertation, a work consisting of several closely related projects. More specific introductions will be given in the following chapters for individual projects.

1.1 The hot interstellar medium and stellar feedback

A central issue in the study of galaxy evolution is the understanding of physical processes in the interstellar medium (ISM). In particular, the hot phase of this medium, with temperatures of 10^6-10^7 Kelvin, has long been theorized and thought to play an essential role in consuming and distributing the energy and metals produced by evolved stars, shaping the cooler phases of the ISM, and feeding back to the intergalactic medium (IGM). Thanks to the advances of modern X-ray observations, with a history back to the 1980s signalled by the launch of the *Einstein Observatory*, the general presence of such a hot interstellar medium (HISM) in normal galaxies is now established.

It is generally believed that the HISM, when it exists, originates either externally from gravitational accretion of the IGM or internally from heated stellar ejecta. The former case, for instance, is prevalent in very massive elliptical galaxies typically found in the centers of groups and clusters of galaxies (e.g., Ellis & O'Sullivan 2006), a phenomenon conventionally referred to as a *cooling flow* (e.g., a review by Mathews & Brighenti 2003). Existing galaxy formation models also hold the standard view that

disk galaxies are formed from the mist of accreted IGM owing to radiative cooling, and hence the presence of a hot gaseous halo is a generic feature in such models. The model-predicted amount of hot gas in the halo, and thus its X-ray emission, is a strong function of the host galaxy's mass (e.g., Toft et al. 2002). However, observational searches for such X-ray-emitting halos around massive disk galaxies remain unsuccessful. While continuing effort need to be made in searching for the X-ray signals, modifications of the current galaxy formation models are probably needed to reconcile the observational results.

A more promising origin of the HISM is *stellar feedback*, primarily in the form of stellar winds and supernovae (SNe). In galaxies with active star formation typically concentrated in a disk of cold gas, stellar feedback manifests itself mainly in terms of Type II SNe, heating the surrounding ISM and driving it into the halo. Such phenomena, sometimes called *superwinds*, are readily observed in archetype starburst galaxies such as M82 (Lehnert, Heckman & Weaver 1999) and NGC253 (Strickland et al. 2000, 2002). It is naturally expected that such superwinds may even reach into intergalactic space, depositing energy, mass and metals there, a process that has been conceived in the above mentioneda galaxy formation models. However, starburst galaxies are infrequent in the local universe and have typically short timescales. When the strength of star formation decreases the importance of such feedback decreases, too. On the other hand, a relatively modest but long-lasting form of feedback could arise from old stellar populations, characterized by energy supplied by Type Ia SNe, mass supplied by stellar ejecta, in particular in terms of red giant winds and planetary nebulae, and metal-enrichment by both the SNe and stellar ejecta. Such stellar feedback is expected to play a crucial role in regulating the evolution of galaxies, particularly early-type galaxies in which star formation has faded out.

Similar to the studies of starburst galaxies and superwinds, it is conceivable to relate the physical properties of the HISM in early-type galaxies, as inferred from

2

X-ray observations, to the feedback from old stellar populations. Studies of this kind would shed light on key open questions such as how effeciently is the ISM heated near sites of feedback, how are the thermal, dynamical and chemical states of the HISM regulated by the feedback, and how does the feedback ultimately interacts with the IGM?

1.2   Outline of the projects

The central effort of my dissertation has been to seek clues and answers to the above questions, by carrying out several elaborate case studies of well-suited nearby galaxies that have been extensively observed in X-ray. The understanding of the observational results, aided with tentative theoretical modelling of the stellar feeback, are presented in the following chapters. Each chapter is based on an indepedent paper published in or submitted to peer-reviewed journals. Those are,

Paper I: *An XMM-Newton Observation of the Massive Edge-on Sb Galaxy NGC 2613* (Li Z., Wang Q.D., Irwin J.A., Chaves T., 2006, MNRAS, 371, 147);

Paper II: *Chandra and XMM-Newton Detection of Large-scale Diffuse X-ray Emission from the Sombrero Galaxy* (Li Z., Wang Q.D., Hameed, S. 2007, MNRAS, 376, 960);

Paper III: *Chandra detection of diffuse hot gas in and around the M 31 bulge* (Li Z., & Wang Q.D. 2007, ApJ, 688, L39)

Paper IV: *M31* and its circumnuclear environment* (Li Z., Wang Q.D., Wakker, B.P. 2008, submitted to MNRAS).

Here I outline the motivations and major results of the individual projects. Hereafter the conventional term "hot gas" is used to represent "HISM" introduced so far. Also "we" instead of "I" will be used to reflect the contribution of various collaborators in these studies. I beg readers' pardon for any confusion caused.

- *Testing disk galaxy formation theories*

  Hot gas in the halos of disk galaxies could arise from accretion of cooled IGM. While remaining an open issue, current models of galaxy formation predict a substantial amount of hot gas cooling around present-day massive disk galaxies, the X-ray emission from which is within the detectable range of modern X-ray observations. With an extensive effort in searching for the predicted X-ray signals, we have analyzed *XMM-Newton* and *Chandra* data of several nearby massive disk galaxies, including NGC2613 (§ 2) and M104 (§ 3), which have circular rotation speeds over 300 km s^{-1}. While significant extraplanar diffuse X-ray emission is detected in these galaxies, the observed luminosities of a few 10^{39} ergs s^{-1} are at least 10 times lower than that predicted by numerical models for such massive galaxies. Hence the X-ray signature of accreted hot gas around disk galaxies remains to be seen. On the other hand, the over-prediction is likely a generic problem of current galaxy formation models, reflecting the lack of an appropriate treatment of stellar/AGN feedback that should substantially reduce or even cease the IGM accretion.

- *Diffuse hot gas in early-type galaxies*

  In early-type galaxies without much current star-forming and/or nuclear activities, feedback from old stellar populations could compete against IGM accretion to build up an extended halo of hot gas. Had most of the stellar feedback been retained within the halo, the observed amount of hot gas should be proportional to the total stellar mass. Our joint *Chandra* and *XMM-Newton* analysis of the bulge-dominated Sa galaxy M104 (§ 3) indicates that this is *not* the case. The observed diffuse X-ray luminosity of M104 accounts for only a few percent of the expected energy input from SNe Ia; the inferred mass and metal content of the gas are also substantially less than those expected from stellar ejecta. A "missing stellar feedback" problem seems to prevail in early-type galaxies,

4

perhaps except for very massive, X-ray-bright elliptical galaxies. We argue that this indicates an outflow of hot gas, in which the bulk of the stellar feedback is transported into a large-scale halo or beyond, leaving only a small fraction detected in the visible regions of the host galaxy.

A quantitative test for the galactic outflow scenario with current X-ray observations, an important step toward understanding the thermodynamical structures of hot gas, has surprisingly not yet been made. To facilitate a direct test, we have constructed a spherically symmetric *galactic wind* model (see Appendix), accounting for mass input from evolved stars and energy input from SNe Ia as well as the gravitational potential of stars and dark matter in determining the gas dynamics. Thermal emission of the modeled gas is calculated under the assumption of collisional ionization equilibrium and tabulated for use in fitting the observed X-ray data. Our results indicate that in M104 the inferred outflow of hot gas is likely subsonic, dynamically distinguished from the classical supersonic *galactic wind*.

- *A Chandra survey of hot gas in the M31 bulge*

  M31, being the nearest spiral galaxy that is similar to our own Galaxy, provides an ideal testbed for studying various X-ray-emitters, in particular diffuse hot gas in a galactic bulge. We have carried out a *Chandra* survey of the M31 bulge by utilizing 31 archival observations (§ 4). The superb spatial resolution and sensitivity afforded by these observations allow for detection and isolation of relatively bright X-ray sources with luminosities above 10^{35} ergs s^{-1}, opening up the possibility of studying the nature of fainter X-ray sources and diffuse hot gas. In particular, we have for the first time identified the truly diffuse X-ray emission of hot gas in and around the M31 bulge, after isolating the X-ray emission of stellar objects, both resolved and unresolved. The diffuse emission appears to be concentrated within a galactocentric radius of ~2 kpc and elongated

5

approximately along the minor-axis at large radii, morphologically reminiscent of a bi-polar outflow from the inner bulge. The observed diffuse X-ray luminosity is only 1% of the expected energy release from SNe Ia, further suggesting an outflow of hot gas that removes the bulk of the stellar feedback from the bulge.

- *The role of stellar feedback in the circumnuclear environment of M31*

  Our successful isolation of the truly diffuse X-ray emission in the M31 bulge in turn allows us to advance the high-resolution study of hot gas in the circumnuclear regions (the central $\sim$500 pc), where different phases of the ISM as well as stars are present in a dense state and likely interacting with each other. Such interactions play a crucial role in regulating the activity of the central super-massive black hole (SMBH) as well as the evolution of the host galaxy on large scales. We have carried out a multiwavelength investigation for this circumnuclear environment of M31 (§ 5), utilizing data obtained by *Chandra*, FUSE, *GALEX*, HST, *Spitzer* and ground-based observations. In particular, the presence of hot gas, traced by diffuse X-ray emission, and its interaction with cooler gas residing in the nuclear spiral, traced by optical line emission and infrared emission, are revealed. We discuss how thermal evaporation, most likely energized by Type Ia SNe, could effectively turn cold gas into hot, leading to the inactivity of the SMBH as well as the outflow of hot gas from the inner bulge. Such a previously overlooked mechanism might be prevalent in similar circumnuclear environments and thus play an important role in the evolution of the host galaxies. Based on significantly improved statistics, X-ray emission of the SMBH, i.e., M31*, is also quantified.

1.3   X-ray observatories and X-ray data analysis

X-ray emission is the best tracer for hot gas at a characteristic temperature of a few millions of Kelvin. In a general sense, the X-ray bandpass covers an energy

range of 0.1-100 keV (1 keV $\simeq 1.16 \times 10^7$ K), or a wavelength range of 0.12-120 Å. The Earth's atmosphere is opaque to X-ray emission, a fact that is crucial to the biology but also demands an extra effort in X-ray astronomy. Consequently, all X-ray observatories are space-based, functioning on-board rockets, ballons and satellites. The two current major X-ray observatories are the *Chandra X-ray Observatory* and *X-ray Multi-Mirror Mission*, both launched in 1999.

Chandra is one of ths NASA's great observatories[1], which is remarkable for its sub-arcsec resolution, good sensitivity from 0.1 to 10 keV, and the capability for moderate spectral resolution observations over most of this energy range. There are two major instruments on-board *Chandra*. One is the High Resolution Camera (HRC), capable of high resolution imaging, fast timing measurements, and observations requiring a combination of both. The second instrument, the Advanced CCD Imaging Spectrometer (ACIS), is made of two-dimentional arrays of charged coupled devices (CCD). ACIS does simultaneous imaging and spectroscopy, a favorable tool for the study of extended objects. All *Chandra* data utilized in this dissertation are obtained by ACIS. ACIS is comprised of two CCD arrays, a square 4-chip array called ACIS-I, and a linear 6-chip array called ACIS-S. There are two types of CCD chips: front-illuminated (FI) CCDs and back-illuminated (BI) CCDs. The FI CCD response is more efficient at higher energies but the energy resolution varies with position. The BI CCDs response extends to lower energies than the FI CCDs and the energy resolution is mostly independent of position. Each CCD chip provides a field of view (FOV) of $\sim 8'$ by $8'$. ACIS-I is comprised of front-illuminated (FI) CCDs. ACIS-S is comprised of 4 FI and 2 BI CCDs, one of which (S3) is at the best focus position.

XMM-Newton[2] is an X-ray observatory launched by the European Space Agency (ESA), which offers so far the largest collecting area for X-rays in the 0.1 to 10 keV

---

[1]http://cxc.harvard.edu/

[2]http://xmm.vilspa.esa.es/

range. *XMM-Newton*'s main instrument is the European Photon Imaging Camera (EPIC). Like the *Chandra* ACIS, EPIC performs both imaging and spectroscopy. It is actually three CCD cameras in one, employing three different detectors to receive X-rays. Two of the detectors are called Metal Oxide Semiconductor (MOS) CCDs, and the other is called a p-n (PN) CCD. Each of the MOS detectors consists of seven CCD chips with one in the center surrounded by the other six, altogether providing a circular FOV of ∼30′ in diameter. The MOS detectors have a time resolution of 1.5 milliseconds and a spatial resolution of one arcsec. The PN consists of two rows of 6 CCD chips, offering a square FOV with a size similar to that of the MOS. The PN has a superb time resolution of 0.03 milliseconds. As a trade-off, its angular resolution is four times lower than that of the MOS (the actual spatial resolution of the EPIC, ∼6 arcsec, is limited by the performance of the mirrors of *XMM-Newton*). The PN also has larger collecting area than the MOS. Overall, the *XMM-Newton* EPIC has larger collecting area, larger FOV, higher time resolution, but lower spatial resolution, as compared to the *Chandra* ACIS.

X-ray detectors are photon-counting in contrast to detectors for most other wavebands that measure incoming flux. Consequently X-ray data consist of lists of events, i.e., incoming photons, tagged with basically four-dimension information: time of arrival, position (2-D) and energy. When filtered according to certain tag(s), the events can be projected onto 2-D or 1-D subspaces to give images, energy spectra, or lightcurves (time series). Depending on the way the data are projected, different calibrations need to be applied. In imaging (spatial) analysis, these are exposure maps, i.e., corrections for the mirror and detector sensitivity across the FOV, and point spread function (PSF), i.e., the probability that an incident photon of given energy and position is registered in a given CCD pixel. In spectral analysis, these are response matrices, i.e., the probability that a photon of given intrinsic energy is

registered in a given detector energy channel, and the auxiliary response files (ARF) which are similar to the exposure maps.

Standard softwares and calibration files for data processing and analysis are usually provided by specific X-ray facilities. For *Chandra*, this is the Chandra Interactive Analysis of Observations (CIAO); For *XMM-Newton*, this is the Science Analysis Software (SAS). A few general tools are also widely used in the X-ray community, e.g., the X-Ray Spectral Fitting Package (XSPEC) for spectral analysis.

CHAPTER 2

AN *XMM-NEWTON* OBSERVATION OF NGC 2613: HOT GAS IN MASSIVE DISK GALAXIES

2.1 Introduction

X-ray observations of extraplanar hot gas ($T \gtrsim 10^6$ K) around nearby edge-on disk galaxies are essential in the study of the galactic ecosystem in many aspects, particularly the disk-halo interaction. Such observations have helped establish the prevalence of galactic superwinds in starburst galaxies, e.g., NGC 253 (Strickland et al. 2000, 2002) and NGC 4666 (Dahlem, Weaver & Heckman 1998), among others. Extraplanar X-ray-emitting gas has also been detected unambiguously around several "normal" late-type galaxies with little evidence for nuclear starbursts: NGC 891 (Sb; Bregman & Houck 1997), NGC 4631 (Scd; Wang et al. 2001), NGC 3556 (Sc; Wang, Chaves & Irwin 2003) and NGC 4634 (Scd; Tüllmann et al. 2006). In these galaxies (except for NGC 4634 which currently lacks direct evidence), extraplanar hot gas is clearly linked to outflows from recent massive star-forming regions in galactic disks. The global X-ray properties of extraplanar gas in these "normal" star-forming galaxies, when scaled with the star formation rate of the host galaxies, appear similar to those found in starburst galaxies (Strickland et al. 2004a, b; Wang 2005). Nevertheless, this needs to be confirmed by extended X-ray observations of "normal" star-forming galaxies.

On the other hand, current galaxy formation models also predict the existence of hot gaseous halos surrounding present-day disk galaxies, which arise from gravitational infall from the IGM (e.g., Toft et al. 2002 and references therein). The

Table 2.1.   Basic information of NGC 2613

Parameter	NGC 2613
Morphology[a]	SA(s)b
Optical size[a]	$7'.2 \times 1'.8$
Inclination angle[b]	$79°$
Position angle[c]	$113°$
Center position[a]	R.A. $08^{h}33^{m}22^{s}.84$
(J2000)	Dec. $-22°58'25''.2$
B-band magnitude [a]	11.16
V-band magnitude [a]	10.25
K-band magnitude [c]	6.82
60 μm flux (Jy)[d]	7.48
100 μm flux (Jy)[d]	25.86
Circular speed (km s^{-1})[b]	304
Distance (Mpc)[b]	25.9
....	($1' \cong$ 7.53kpc)
Redshift[a]	0.00559
Galactic foreground N_{HI} (10^{20} cm^{-2})[e]	6.8

References. — *a*. NED; *b*. Chaves & Irwin (2001); *c*. Jarrett et al. (2003); *d*. Sanders et al. (2003); *e*. Dickey & Lockman (1990).

predicted extraplanar X-ray luminosity strongly depends on the mass of the host galaxy. X-ray observations thus have long been expected to detect such gaseous halos around nearby massive, typically earlier-type disk galaxies. However, there is so far little direct observational evidence for the presence of this kind of X-ray-emitting halo. Benson et al. (2000) analyzed X-ray emission from the outer halos ($\gtrsim 5'$) of primarily two early-type spirals NGC 2841 (Sb) and NGC 4594 (Sa), using *ROSAT* PSPC observations. No significant diffuse emission was detected, although the upper limits to the diffuse X-ray luminosities are consistent with the current predictions (Toft et al. 2002). Therefore, more dedicated searches for the X-ray signals of IGM accretion around disk galaxies are needed.

Here we present a study of an *XMM-Newton* observation toward NGC 2613, an edge-on Sb galaxy with "normal" star formation. We focus on probing the spatial and spectral properties of its large-scale X-ray emission. This galaxy (Table 2.1) is a good candidate to probe the presence of hot gas, in the sense that: 1) it is very massive and thus expected to contain a large amount of hot gas; 2) its high inclination ($\sim 79°$) allows the possibility of detecting extraplanar emission, either from a halo of accreted gas or a large-scale outflow; 3) its moderately large distance (25.9 Mpc) places the galaxy and its ~ 50 kpc vicinity in the FOV of a typical *XMM-Newton* observation, offering a good opportunity of studying the large-scale distribution of gas, and 4) it is known to show extraplanar features at other wavebands, specifically the radio continuum and HI (Chaves & Irwin 2001; Irwin & Chaves 2003) as well as earlier HI observations (Bottema 1989).

2.2 Observations and Data Reduction

We obtained two *XMM-Newton* observations on NGC 2613. The first observation (Obs. ID 0149160101), taken on April 23/24, 2003 with a 40 ks exposure, suffered heavily from background flares. Consequently, another observation (Obs. ID 0149160201) with a 33 ks exposure was taken on May 20/21, 2003. In our analysis, we only used data obtained from the second observation.

We used SAS, version 6.1.0, together with the latest calibration files for data reduction. For the MOS data, we selected only events with patterns 0 through 12 and applied flag filters XMMEA_EM, XMMEA_2, XMMEA_3 and XMMEA_11. For the PN data, we selected only events with patterns 0 through 4 and applied flag filters XMMEA_EP, XMMEA_2, XMMEA_3 and XMMEA_11. According to light curves of the MOS and the PN, we further excluded time intervals with high background rates by setting good time interval thresolds of 2.0 cts/s for the MOS in the 0.3-12 keV range and 6.0 cts/s for the PN in the 0.3-15 keV range, respectively. The resulting

net exposure time is 23.5 ks for the MOS and 18.7 ks for the PN. We used the *skycast* program to generate the "blank-sky" background for our observation. Same event filters were applied to the "blank-sky" event files, resulting in exposures of 791, 759 and 294 ks for the MOS1, MOS2 and PN, respectively. We then constructed images and exposure maps at the 0.2-0.5, 0.5-1, 1-2, 2-4.5 and 4.5-7.5 keV bands for each detector. For spectral analysis, we selected only events with FLAG = 0.

2.3 Analysis and Results

2.3.1 Discrete X-ray Sources

We perform source detection on the PN images of the soft (S, 0.5-2 keV), hard (H, 2-7.5 keV) and broad (B=S+H) bands. As detailed in Wang (2004), the source detection procedure, optimized to detect point-like sources, uses a combination of detection algorithms: wavelet, sliding-box and maximum likelihood centroid fitting. The source detection uses a detection aperture of the 50% PSF encircled energy radius (EER). Multiple detections with overlapping 2σ centroid error circles are considered to be the same source, and the centroid position with the smallest error is adopted. The accepted sources all have a local false detection probability $P \leq 10^{-7}$. We detect a total of 67 discrete sources on the PN images (Fig. 2.1), 5 of which are located within the $I_B = 25$ mag arcsec^{-2} isophote of the galaxy.

The prominent nucleus of NGC 2613 is readily seen in Fig. 2.2a. The nucleus is the only source detected within the central $30''$, suggesting that this emission may represent an active galatic nucleus (AGN). To investigate this further, we perform a spectral analysis on the nuclear emission. Due to the relatively low spatial resolution and short exposure time of the observation as well as the relatively large distance to NGC 2613, the spectrum extraction of the nucleus is a compromise between having better counting statistics and suffering less contamination from non-nuclear emission around the nucleus. To assess the contribution from non-nuclear emission, we extract
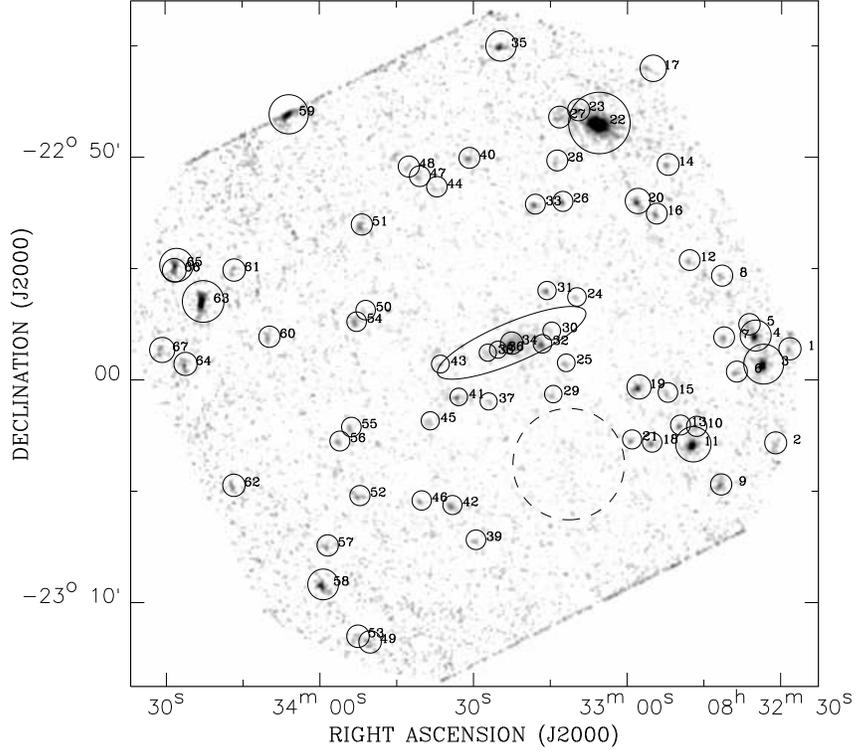
Figure 2.1 EPIC-PN intensity image in the 0.5-7.5 keV band after flat-fielding. An adaptively smoothed background has been subtracted from the image to highlight the discrete sources, which are marked by circles with radii of twice the 50% EER. The ellipse illustrates the optical $I_B = 25$ mag arcsec^{-2} isophote ($7'.2 \times 1'.8$) of NGC 2613. The dashed circle outlines the region where the local background spectrum is extracted for spectral analysis.

two spectra from circles with radii of $10''$ and $16''$ around the galactic center, for each detector. The $10''$ ($16''$) radius corresponds to a physical scale of $\sim$1.2 (2.0) kpc at the distance of NGC 2613 and represents an enclosed energy fraction (EEF) of $\sim$0.50 (0.65) in the PN and $\sim$0.55 (0.70) in the MOS. We extract a background spectrum for each detector from a circle with a $2'.5$ radius at $\sim 6'$ to the south of the galactic disk (Fig. 2.1). This background region is chosen because it shows a low X-ray intensity and is at an off-axis angular distance comparable to that of the disk. We then bin the source spectra to achieve a background-subtracted signal-to-noise ratio ≥ 2.
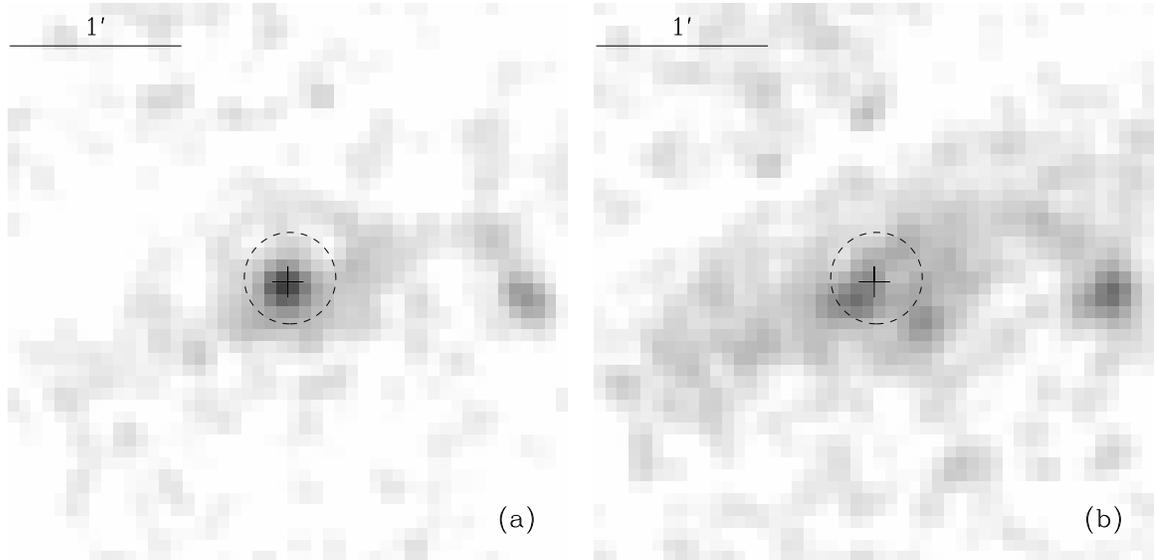
Figure 2.2 EPIC-PN intensity images around the galactic center in the 2-7.5 (a) and 0.5-2 (b) keV bands. The nucleus is prominent only in the hard band. The plus sign marks the optical center of NGC 2613. The dashed circle with a 16″ radius illustrates the region for the spectrum extraction.

The spectra from the 16″ circle show a prominent broad bump at energies $\sim$ 4-5 keV (Fig. 2.3), which can also be seen in the spectra from the 10″ circle. This is further evidence that the nuclear region contains an AGN since the spectra can naturally be explained by a combination of a heavily absorbed power-law from an AGN and a softer contribution from non-nuclear emission. We jointly fit the PN, MOS1 and MOS2 spectra in the 0.3-12 keV range with XSPEC. Owing to the lack of obvious features below 3 keV in the spectra, a composite model of *wabs[zwabs(PL)+PL]* is applied, where the first power-law component (PL1) with intrinsic absorption characterizes the nuclear emission and the second power-law component (PL2) represents the non-nuclear emission. In the fit, we require that the amount of foreground absorption be at least that supplied by the Galactic foreground (as specified in *wabs*: $N_{HI} \geq 6.8 \times 10^{20}$ cm^{-2}). Fit results for the 10″ and 16″ spectra are consistent with each other within the uncertainty ranges. We list in Table 2.2 the fit results to the 16″ spectra, the implications of which will be discussed in § 2.4.1. All quoted errors in the

Table 2.2. Spectral fit to the nuclear emission[a]

Parameter	Value
χ^2/d.o.f.	64.6/65
[b]N_{HI} (10^{20} cm^{-2}) ..	6.8 (<11.4)
[c]N_{HI} (10^{22} cm^{-2}) ..	$12.3^{+12.3}_{-5.7}$
Photon index (PL1)	$2.1^{+1.8}_{-0.3}$
Photon index (PL2)	$1.7^{+0.5}_{-0.3}$
[d]$f_{0.3-10}$ (PL1)	41
[d]$f_{0.3-10}$ (PL2)	4.2

Note. — a. See text for model description; b. Foreground column density; c. Intrinsic column density; d. Intrinsic 0.3-10 keV flux in units of 10^{-14} ergs cm^{-2} s^{-1}.

tables are at the 90% confidence level. The best-fit two-component model is shown in Fig. 2.3.

We note that in the PN spectrum there is some hint of excess over the best-fit two-component model at $\sim$0.9 keV, which might be physically due to the presence of diffuse hot gas around the nucleus. We thus try to include a thermal plasma component (APEC in XSPEC) in the fit to probe the existence of an additional thermal component. While the best-fit temperature of this component is, as expected, $\sim$0.9 keV, the fit is not significantly improved according to an F-test, and the range of the fitted temperature could not be well constrained. Therefore we consider this potential thermal component insignificant in the spectra.

Given the relatively high source detection limit ($\sim 2 \times 10^{38}$ ergs s^{-1}) and the relatively low spatial resolution, the bulk of expected galactic X-ray sources of NGC 2613 are still embedded in unresolved emission. Indeed, only four sources (in addition to the nucleus) are detected within the D_{25} ellipse of the galaxy. We jointly fit the ac-
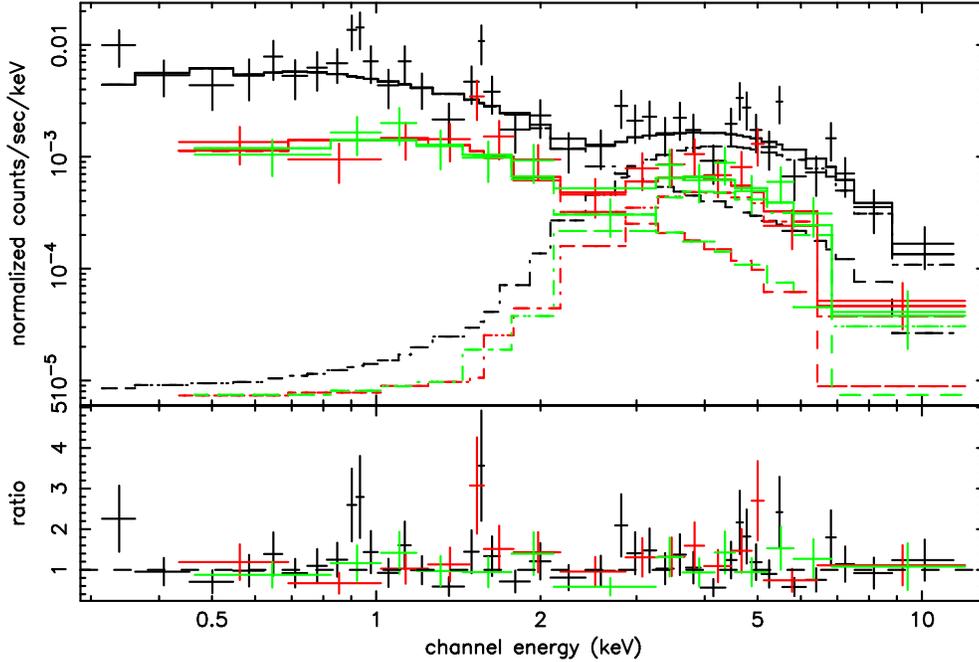
Figure 2.3 EPIC spectra (Black: PN spectrum; Red: MOS1 spectrum; Green: MOS2 spectrum) of the nucleus of NGC 2613 extracted from a 16″ circle. The best-fit model (solid curve) consisting of two absorbed power-law components (dashed and dash-dot curves, respectively) is also plotted. The lower panel shows the data-to-model ratios.

cumulated spectra of these four sources extracted from individual detectors. Circles with radii of twice the 50% EER around individual sources are used to accumulate the spectra. Corresponding background spectra are extracted from the source-removed D_{25} ellipse. We find that an absorbed power-low model fits the spectra well, giving a best-fit photon index of $1.80^{+0.30}_{-0.27}$ and an intrinsic 0.3-10 keV luminosity of 4.3×10^{39} ergs s^{-1}. The slope of the power-law is typical for X-ray binaries. Given their high luminosities ($\gtrsim 10^{39}$ ergs s^{-1}), on average, these sources are likely ultra-luminous X-ray binaries.

2.3.2 Unresolved X-ray emission

2.3.2.1 Spatial distribution

As an overview, Fig. 2.4 shows the large scale 0.5-2 keV X-ray emission around NGC 2613 and its similarity with the optical disk. Along the major axis of the disk, the emission appears rather smooth and is confined within ~2.5 from the galactic center. Whereas along the direction perpendicular to the disk, some extended features are present, forming well-defined structures. To the north of the disk (Fig. 2.4) is a "bubble-like" feature, which is referred to as the 'north bubble' in the following. This feature follows the minor axis fairly well and has a maximum extent of $\sim 100''$ (13 kpc) from the nucleus. Immediately on the opposite side of the nucleus is another extension that is somewhat smaller, reaching $\sim 1'$. This feature will be called the 'south extension'. A third feature protrudes from the south side of the major axis but west of the minor axis. This feature will be called the 'south-west feature'. Finally two very large extensions are seen to the east of the major axis with emission peaks located at RA= $08^h33^m37^s$, DEC= $-22°59'19''$ (north arc), and RA= $08^h33^m33^s$, DEC= $-23°0'51''$ (south arc). These have the appearance of arising from the eastern tip of the X-ray disk and will be called the 'eastern extensions' consisting of northern and southern arcs. The above features are labelled in Fig. 2.4 for ease of reference. Most of these features extend significantly beyond the optical disk. Given the extent of the X-ray emission along the major axis and the inclination of the disk, the projected in-disk emission along the minor axis should be within $45''$, whereas most of the extended features show an extent larger than $1'$. Therefore, we suggest that these features are truly extraplanar. Their origin will be further discussed in § 2.4.

We remove the detected discrete sources, except for the nucleus, to study the spatial properties of the unresolved soft X-ray emission. The nucleus is kept because it is heavily obscured (§ 2.3.1) and contributes few photons to the emission below 2 keV. For each faint source with a count rate $(CR) \leq 0.01$ cts s^{-1}, we exclude a
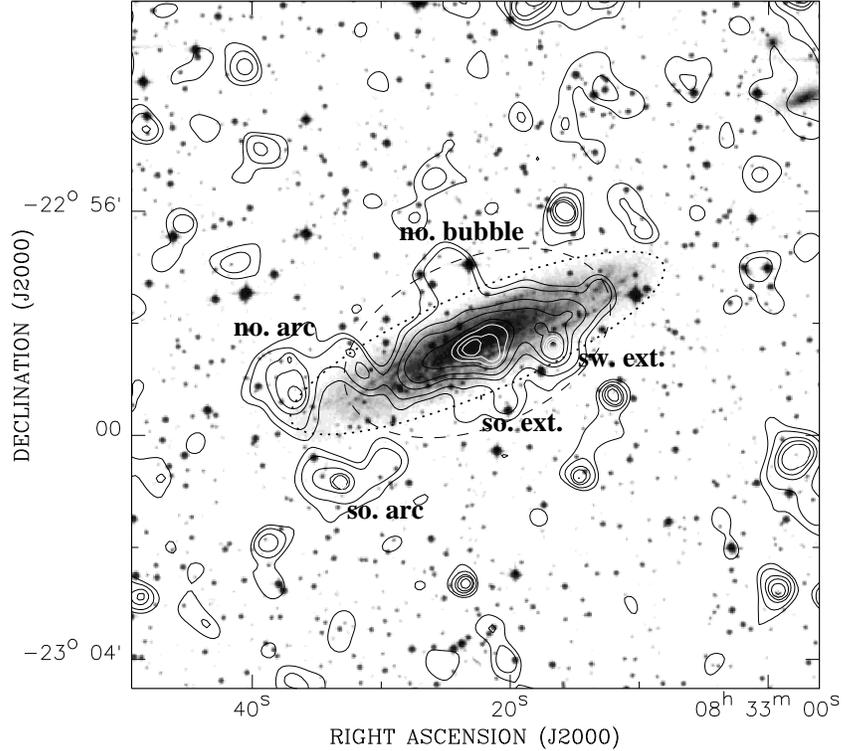
Figure 2.4 EPIC-PN 0.5-2 keV intensity contours overlaid on the digitized sky-survey (first generation) image of NGC 2613. The X-ray intensity is adaptively smoothed with CIAO *csmooth* to achieve a signal-to-noise ratio of ~3. The contour levels are at 4.1, 5.0, 7.0, 8.8, 13, 16, 22 and 32 $\times 10^{-3}$ cts s^{-1} arcmin^{-2}. The dotted ellipse represents the optical $I_B = 25$ mag arcsec^{-2} isophote of the galaxy. The dashed ellipse ($5' \times 3'$) illustrates the region where spectra of unresolved X-ray emission are extracted.

circular region with a radius of twice the 50% enclosed energy radius (EER). For sources with $CR > 0.01$ cts s^{-1}, the radius is multiplied by an additional factor of $1+\log(CR/0.01)$. The choice of the adopted radii is a compromise between removing the bulk of the source contribution and preserving a sufficient field for the study of unresolved emission. Thus 75-80% of photons from each detected source is removed according to our criteria.

We construct the "blank-sky" background-subtracted, exposure-corrected 0.5-2 keV intensity profile from the source-removed PN image, as a function of off-center

distance along the minor axis. The full width along the direction parallel to the major axis used for averaging the intensity is $5'$ ($\sim 0.7 D_{25}$), approximately the maximal extent of the unresolved emission along the major axis (Fig. 2.4). The profile is shown in Fig. 2.5. We characterize the profile by an exponential law: $I(R) = I_0\, e^{-|z|/z_0}$, where $|z|$ is the vertical distance from the center, z_0 is the scale height and I_0 is the central intensity. A constant intensity I_b is included in the fit to account for the discrepancy between the local background and the subtracted "blank-sky" background, and it turns out to be negligible. The results are listed in Table 2.3. The best-fit model is also plotted in Fig. 2.5 (black dashed curve). There is an excess over the best-fit model at a vertical distance of $\sim 1'$-$1\rlap{.}'5$, which can be attributed to the extraplanar features apparent in Fig. 2.4. The total count rate produced by this extraplanar excess is $\sim 5.2 \times 10^{-3}$ cts s^{-1}.

The unresolved emission should consist of two components: 1) emission from truly diffuse gas, and 2) collective discrete contributions from sources below our detection limit plus some residual counts spilled outside our source removal regions. To constrain the source component, we assume that it follows the distribution of the NIR K-band light of the galaxy, which can be determined from the 2MASS K-band map (Jarrett et al. 2003). We remove from the map bright foreground stars and convolve it with the PSF of the PN. Circular regions used for removing the discrete X-ray sources are also excluded from the map. The K-band vertical profile is then produced in the same manner as for the X-ray profile. To compare the two profiles, we normalize the K-band profile to match the X-ray intensity at the center (Fig. 2.5). This requires a normalization factor of 3.0×10^{-3} cts s^{-1} arcmin^{-2}/(MJy sr^{-1}). Within a vertical distance of $1'$, the K-band profile traces the X-ray profile quite well. An excess over the K-band profile, however, remains at a vertical distance of $\sim 1'$-$1\rlap{.}'5$. This is evidence for the presence of extraplanar X-ray-emitting gas.
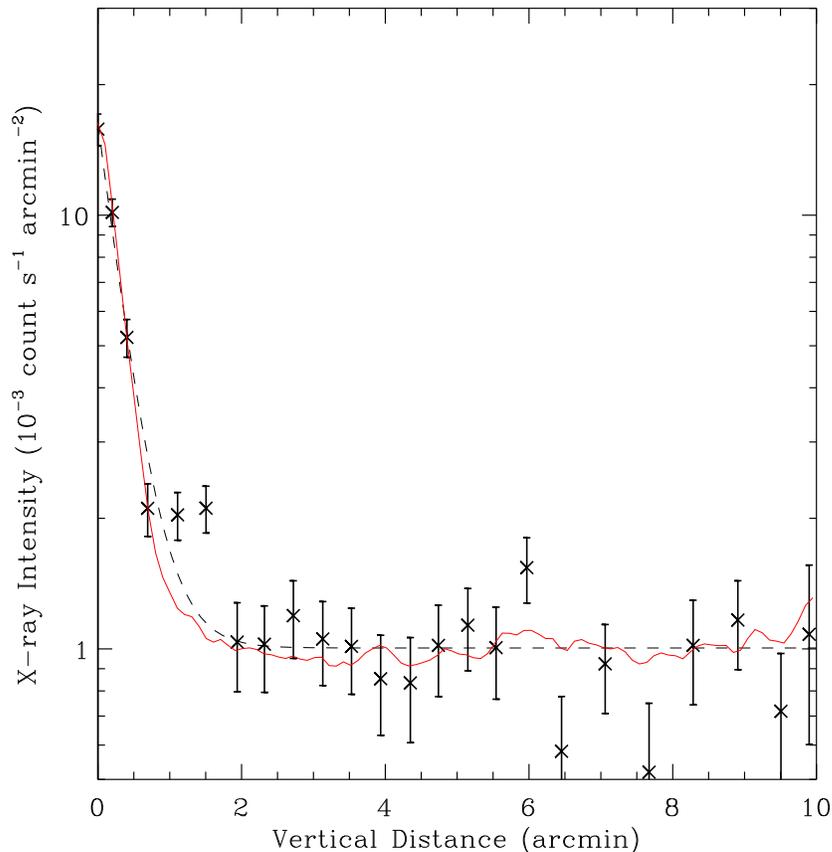
Figure 2.5 EPIC-PN 0.5-2 keV intensity profile (black crosses) along the direction perpendicular to the disk of NGC 2613. A "blank-sky" background has been subtracted and discrete sources have been removed, except for the nucleus. The full width used for averaging the intensity is $5'$. Spatial binning is adaptively adjusted to achieve a count-to-noise ratio greater than 12, with a minimum step size of $12''$. The black dashed curve is a fit to the profile using an exponential law plus a constant local background. The red solid curve shows the 2MASS K-band profile convolved with the PN PSF and normalized by a factor of 3.0×10^{-3} cts s^{-1} arcmin^{-2}/(MJy sr^{-1}) (see text). A constant of 10^{-3} cts s^{-1} arcmin^{-2} has been added to all data points to avoid negative values improper for a logarithmic plot.

We also construct a 0.5-2 keV radial intensity profile for the unresolved emission. Elliptical photometry is applied, with a minor-to-major axis ratio of 0.29 and a position angle of 113° (Jarrett et al. 2003). We again fit the radial profile with an exponential law and list the results in Table 2.3. The X-ray profile together with the best-fit model is plotted in Fig. 2.6. Also plotted is the normalized 2MASS K-band

21

radial profile produced in the same way as is done for the X-ray profile. The K-band and X-ray profiles closely trace with each other within a semi-major radius of $\sim 3'$. At semi-major radii $\sim 4'$-$6'$, corresonding to semi-minor radii $\sim 1\rlap{.}'1$-$1\rlap{.}'7$, a bump is present, again most likely due to the extraplanar features. The total count rate of this bump is consistent with the extraplanar excess seen in the vertical intensity profile.
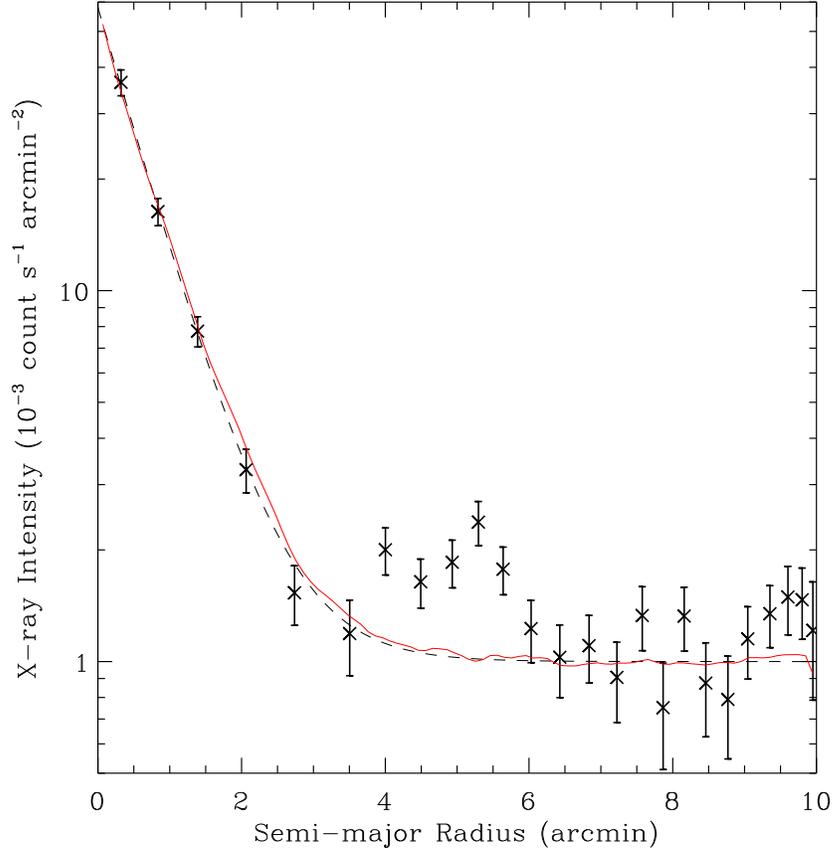
Figure 2.6 Similar to Fig. 2.5 but for the radial profile, generated with the elliptical photometry (see text). A constant of 10^{-3} cts s^{-1} arcmin^{-2} has been added to all data points to avoid negative values improper for a logarithmic plot.

2.3.2.2   Spectral properties

Guided by the X-ray morphology (Fig. 2.4), a galactocentric $5' \times 3'$ ellipse with a position angle of $113°$ is adopted to extract the spectra of unresolved emission for individual detectors. The limited number of counts prevents us from further

Table 2.3.   Fit to 0.5-2 keV surface intensity distributions

Parameter	Vertical distribution	Radial distribution
χ^2/d.o.f.	42.4/24	65.2/23
[a]I_0 (10^{-3} cts s^{-1} arcmin^{-2})	$15.3^{+1.8}_{-1.8}$	$57.0^{+8.4}_{-9.1}$
[b]z_0 (r_0) (arcmin)	$0.32^{+0.04}_{-0.04}$	$0.65^{+0.06}_{-0.06}$
[c]I_b (10^{-3} cts s^{-1} arcmin^{-2})	$0.0^{+1.0}_{-1.0}$	[d]0.0

Note. — a. Central intensity; b. Scale height (length) of the exponential law; c. Local background intensity above the already subtracted "blank-sky" background; d. Fixed at the value obtained from the vertical fit.

dividing the spectra according to different regions of interest, e.g., the disk and the halo. Discrete sources are removed in the way as described above, except for the nucleus, for which we exclude a circular region with a radius of $40''$ ($\sim$87% EER) to further reduce the contamination from the hard nuclear emission. We use the same background spectra as applied in § 2.3.1.

We jointly fit the PN, MOS1 and MOS2 spectra in the 0.3-8 keV range (Fig. 2.7). Overall, the spectra are much softer than those from the nuclear region, showing clear features at $\sim$ 0.9 keV, corresponding to the Fe L-shell complex, and at $\sim$ 0.5 keV. These features further indicate the presence of diffuse hot gas. At energies above 2 keV the spectra are dominated by a collective contribution from unresolved discrete sources, most likely LMXBs (see § 2.4.2). We account for this contribution with a power-law (PL) with a photon index fixed at 1.56, as found by Irwin, Athey & Bregman (2003) for the accumulated spectra of galactic LMXBs. This PL, combined with a thermal plasma component (APEC) is then used to fit the spectra. Foreground absorption is again required to be at least the Galactic value. The fit is initialized by fixing the plasma metal abundance at solar. The model, however, yields a poor fit to the spectra, in particular failing to simultaneously account for the features at

Table 2.4.   Spectral fit to the unresolved emission

Model	N_{HI} [a]	α [b]	Temperature[c]	Abundance	Flux[d]	χ^2/d.o.f.
PL+APEC	6.8 (<7.9)	1.56	$0.78^{+0.18}_{-0.14}$	1.0[e]	7.5 (PL), 1.3	81.1/66
PL+APEC	6.8 (<17.9)	1.56	$0.84^{+0.25}_{-0.49}$	0.02 (<0.05)	3.2 (PL), 4.4	57.9/65
PL+2APEC	6.8 (<21.9)	1.56	$0.08^{+0.12}_{-0.03}$, $0.81^{+0.19}_{-0.11}$	1.0[e]	6.5 (PL), 3.2, 1.4	62.5/64

Note. — a. Column density in units of 10^{20} cm^{-2}, minimum sets at the Galactic foreground value of 6.8; b. Power-law photon index, fixed at the uniform value for LMXBs found by Irwin et al. (2003). c. In units of keV; d. Intrinsic 0.3-10 keV fluxes in units of 10^{-14} ergs cm^{-2} s^{-1}; e. In units of solar, fixed.

$\sim$0.9 keV and $\sim$0.5 keV. By allowing the metal abundance to be fitted, we obtain a statistically better fit but the resulting abundance is low ($\lesssim$ 0.05 solar). Such an extremely sub-solar abundance is unphysical and practically often encountered in the X-ray spectral analysis for galaxies (e.g., NGC 253, Strickland et al. 2002; NGC 4631, Wang et al. 2001). We thus add to the model a second APEC component. A two-temperature plasma is effective in characterizing the diffuse spectra of some star-forming disk galaxies (e.g., Strickland et al. 2004a; Tüllmann et al. 2006). The abundances for both thermal components are fixed at solar. The fit is acceptable, resulting in a cool component with $kT \sim$0.08 keV and a hot component with kT $\sim$0.8 keV. The 0.3-10 keV X-ray luminosities are 5.2, 2.6 and 1.1$\times$10^{39} ergs s^{-1} for the three components, namely the discrete sources, the low temperature gas and the high temperature gas, respectively. The above results are summarized in Table 2.4. We adopt the two-temperature fit as the best-fit model in the following and plot it in Fig. 2.7.

2.4   Discussion

2.4.1   The nature of the nuclear X-ray emission

Our two-component spectral fit for the nucleus (§ 2.3.1; Table 2.2) indicates that the intrinsic neutral hydrogen column density is $\sim$1.2$\times$10^{23} cm^{-2}. This is much higher than the beam-averaged HI column density of $\sim$2 $\times$ 10^{21} cm^{-2} found by Chaves &
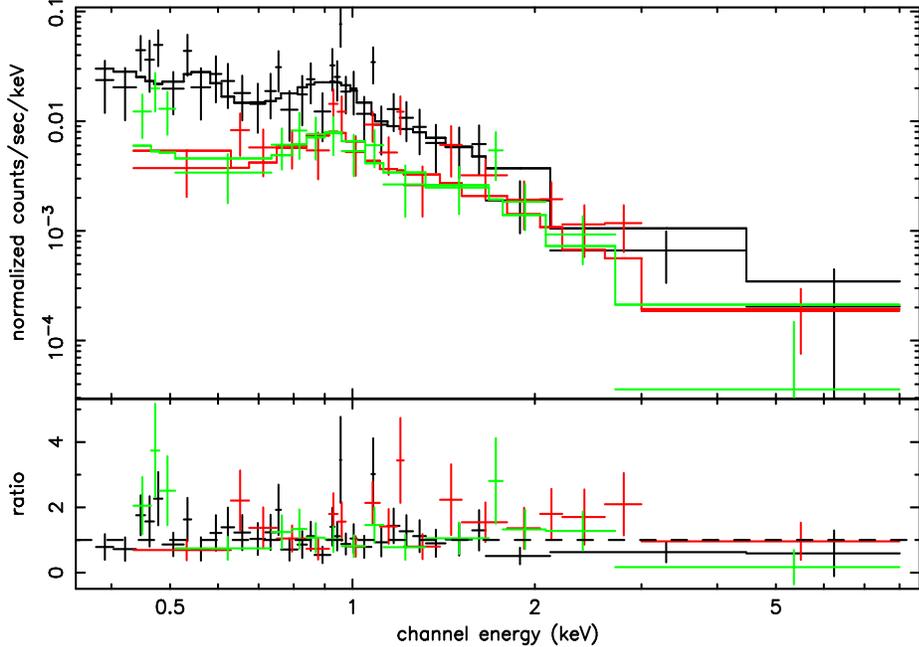
Figure 2.7 EPIC spectra of unresolved X-ray emission (Black: PN spectrum; Red: MOS1 spectrum; Green: MOS2 spectrum) of NGC 2613 and the best-fit *wabs(PL+2APEC)* model. The spectra are binned to achieve a background-subtracted signal-to-noise ratio better than 2. The lower panel shows the data-to-model ratios.

Irwin (2001), but it is typical of values found for molecular circumnuclear disks. Ott et al. (2001), for example, find a molecular column density of order 10^{23} cm^{-2} for NGC 4945. Molecular data are not yet available for NGC 2613, but our results suggest that a substantial molecular component should be present in this galaxy.

For the nuclear component, the modelled intrinsic flux given in Table 2.2 leads to an intrinsic X-ray luminosity of $\sim 3.3 \times 10^{40}$ ergs s^{-1} in the 0.3-10 keV range. The photon index of this component is ~ 2, a typical value found in the X-ray spectra of AGNs (e.g. Pellegrini, Fabbiano & Kim 2003). No radio core was detected by Irwin, Saikia & English (2000), putting a 3σ upper limit of 4.5×10^{27} ergs s^{-1} Hz^{-1} on the radio spectral power at 1.425 GHz within the same 16″ region. Using the above luminosity over the 0.3-10 keV range, we derive an upper limit of $\alpha = 0.62$ on the energy spectral index ($S_\nu \propto \nu^{-\alpha}$) between the radio and X-ray bands. Although the X-ray nucleus is heavily obscured, these values nevertheless suggest that the

energy spectral index is likely flat or possibly rising at the low frequencies, a fact again consistent with the interpretation of the nuclear source as an AGN. Thus, we conclude that the nuclear X-ray source represents an AGN in this galaxy, the first evidence that this is the case.

The non-nuclear component, characterized by the second power-law (PL2), shows a photon index of ~ 1.7 and an intrinsic 0.3-10 keV luminosity of 3.4×10^{39} ergs s^{-1}. Irwin et al. (2003) showed that the accumulated spectra of LMXBs in early-type galaxies can be uniformly described by a power-law model with a best-fit photon index of 1.56 ± 0.02. By using a sample of nearby galaxies of various morphological types, Gilfanov (2004) studied the relation between the collective luminosity of LMXBs and the K-band luminosity, L_K, of the underlying stellar content. He found that, for LMXBs with luminosity higher than 10^{37} ergs s^{-1}, their collective luminosity $L_X = (3.3 - 7.5) \times 10^{39}$ ergs s$^{-1} L_K/10^{11} L_{\odot,K}$. Assuming that the spatial distribution of LMXBs follows that of the K-band star light (Jarrett et al. 2003), we estimate that the collective luminosity of LMXBs within the 16″ circle is $\sim (1.8 - 4.2) \times 10^{39}$ ergs s^{-1}. Thus the non-nuclear component is consistent with the collective emission of unresolved LMXBs. We note that high-mass X-ray binaries (HMXBs) are expected to be present in star-forming disk galaxies and their composite spectral properties are somewhat similar to that of the LMXBs, thus the collective contribution of HMXBs may also be partly responsible for the non-nuclear component. We show below that in NGC 2613 the relative contribution of HMXBs is small as compared to that of LMXBs.

2.4.2 The collective X-ray emission of discrete sources

It is known that X-ray binaries, including LMXBs and HMXBs, dominate the X-ray source populations with luminosities $\gtrsim 10^{35}$ ergs s^{-1} in galaxies. Owing to their distinct evolution time-scales, the numbers and thus the collective contributions

of long-lived LMXBs and short-lived HMXBs to the X-ray emission of a galaxy are expected to be proportional to its stellar mass and star formation rate (SFR), respectively. Colbert et al. (2004) analyzed *Chandra* observations of X-ray sources in a sample of nearby galaxies of various morphological types and SFRs. They found that the collective X-ray luminosity of point sources L_{XP} is linearly correlated with the total stellar mass $M_\star$ and the SFR of the host galaxy as

$$L_{XP} \ (\text{ergs s}^{-1}) \ = \ (1.3 \pm 0.2) \times 10^{29} \ \text{M}_\star \ (\text{M}_\odot)$$
$$+ (0.7 \pm 0.2) \times 10^{39} \ \text{SFR} \ (\text{M}_\odot \ \text{yr}^{-1}). \tag{2.1}$$

We use this relation to assess the relative importance of LMXBs and HMXBs in contributing to the X-ray emission of NGC 2613. The total stellar mass can be estimated from the K-band luminosity L_K and the $B - V$ color index via (Bell & de Jong 2001)

$$\log(M_\star/L_K) = -0.692 + 0.652(B - V), \tag{2.2}$$

where L_K is in units of the K-band Solar luminosity. The SFR can be estimated from the far-infrared (FIR) luminosity L_{FIR} via (Kennicutt 1998)

$$\text{SFR} \ = \ 4.5 \times 10^{-44} \ \text{L}_{\text{FIR}} \ (\text{ergs s}^{-1}). \tag{2.3}$$

L_{FIR} is measured according to (Lonsdale, Helou & Good 1989)

$$L_{FIR} = 3.1 \times 10^{39} \ D^2 \ (2.58 \ S_{60} + S_{100}), \tag{2.4}$$

where D is the distance of the galaxy in units of Mpc, S_{60} and S_{100} are the flux densities in units of Jy at 60 μm and 100 μm, respectively. With the available photometric data for NGC 2613 (Table 2.1), we estimate that the total stellar mass

is 2.1×10^{11} M$_\odot$ and the SFR is 4.2 M$_\odot$ yr^{-1}. Based on Eq. (2.1), the contributions of LMXBs and HMXBs to the collective X-ray emission of discrete sources is $\sim$ 2.7×10^{40} ergs s^{-1} and $\sim 2.9 \times 10^{39}$ ergs s^{-1}, respectively, with the latter being about 10% of the former.

In the disk of NGC 2613, we find that the 0.5-2 keV unresolved emission is spatially correlated with the K-band star light. Therefore, the normalization factor for the K-band profile (§ 2.3.2.1) should represent the collective X-ray emissivity of the underlying old stellar population. Using the power-law model given by Irwin et al. (2003) for the accumulated spectrum of LMXBs, we convert the observed 0.5-2 keV count rate into the intrinsic luminosity in the 0.3-10 keV band). The K-band flux density is also converted into intrinsic luminosity according to the 2MASS K-band photometry. The normalization factor, 3.0×10^{-4} cts s^{-1} arcmin^{-2}/(MJy sr^{-1}), is then equivalent to an X-ray emissivity of $L_X = 4.2 \times 10^{39}$ ergs s$^{-1} L_K/(10^{11} L_{\odot,K})$, or a luminosity ratio of $L_X/L_K \sim 7.5 \times 10^{-4}$. Gilfanova (2004) found that the collective X-ray luminosity of galactic LMXBs is related to the underlying K-band luminosity following $L_X = (3.3 - 7.5) \times 10^{39}$ ergs s$^{-1} L_K/(10^{11} L_{\odot,K})$, i.e., a luminosity ratio of $L_X/L_K \sim (5.8 - 13.2) \times 10^{-4}$. Therefore the collective X-ray emissivity of unresolved discrete sources inferred for NGC 2613 is consistent with that of the galactic LMXBs, and we conclude that the collective X-ray emission of LMXBs dominates the soft emission of NGC 2613 in its disk region.

2.4.3 The origin of extraplanar gas

Presence of diffuse gas in NGC 2613 is evident by the soft X-ray excess over the K-band light. We consider two possible origins of the diffuse gas: 1) the continuously accreted IGM (Toft et al. 2002) and 2) the outflow from the galactic disk (Irwin & Chaves 2003).

2.4.3.1 An accreted gaseous halo?

Toft et al. (2002) calculated global X-ray properties (e.g., luminosity, effective temperature and intensity distribution) of hot gaseous halos, based on their simulated galaxies. The predicted luminosity strongly depends on the circular speed of the host galaxy. The most massive galaxies in their simulations have circular speeds similar to that of NGC 2613 (~ 300 km s^{-1}). The predicted 0.2-2 keV luminosity for such a galaxy is $\sim 8 \times 10^{40}$ ergs s^{-1} (Fig. 3 in Toft et al. 2002). From our best-fit spectral models of the spectra of unresolved emission, we derive an intrinsic 0.2-2 keV luminosity of $\sim 8 \times 10^{39}$ ergs s^{-1} for the sum of the thermal and power-law components, and $\sim 6 \times 10^{39}$ ergs s^{-1} for the thermal components only. We note that the unresolved emission outside our spectral extraction region contributes little to the total luminosity. The simulated luminosity of gas emission by Toft et al. (2002) is at least an order of magnitude higher than the observed value for NGC 2613. We therefore conclude that the simulations as presented by Toft et al. (2002) substantially over-predict the X-ray emission from the cooling inflow of the IGM, if this is what is occurring in NGC 2613.

This over-prediction is related to the so-called over-cooling problem in current theories of galaxy formation. We speculate that the over-cooling problem is a result of an inappropriate treatment of stellar and/or AGN feedback. For example, the mechanical energy input from Type Ia supernovae (SNe) is typically not included in galaxy formation simulations, partly due to the difficulty in treating the astrophysics related to gaseous flows. Qualitatively, Type Ia SNe, which tend to occur in low-density hot environments, provide an especially effective mechanism for large-scale distributed heating, required to reduce the cooling of gas in galactic bulges and halos (Tang & Wang 2005). Massive stars in galactic disks may also serve as sources of mechanical energy that could produce outflows into halos and help slow down the cooling of the accreted gas. For example, with a star formation rate of $\sim 4.2\, M_\odot$ yr^{-1}

for stars between 0.1 and 100 $M_\odot$, and assuming a Salpeter IMF and that stars with mass > 8 $M_\odot$ become core-collapse SNe, the rate of total energy release from the star-forming regions of NGC 2613 is $L_{SNII} \sim 1.0 \times 10^{42}$ ergs s^{-1}. Our spatial and spectral analyses suggest that the extraplanar gas is responsible for the thermal emission (§ 2.3.2) and has a total 0.3-10 keV luminosity of $\lesssim 5 \times 10^{39}$ ergs s^{-1}. Thus, SNe can provide enough energy to explain the X-ray emission of the extraplanar gas in NGC 2613.
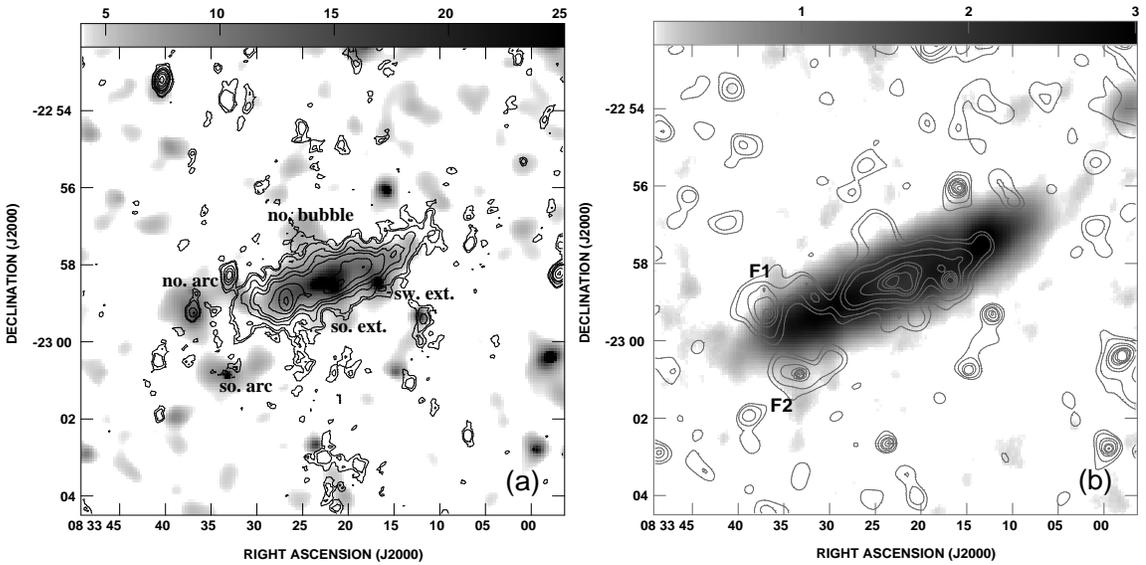
Figure 2.8 (a) VLA C+D configuration continuum contours overlaid on the same X-ray intensity image (grey scale) as contoured in Fig. 2.4 and in (b) of this figure. The contour levels are 0.18, 0.27, 0.56, 0.84, 1.1, 1.7, 2.3, 3.2 mJy beam^{-1} and the beam is $22'' \times 15''$ at a position angle of $-8\overset{\circ}{.}2$. A few X-ray extraplanar features are labelled (see text). (b) The same X-ray intensity contours as in Fig. 2.4 overlaid on a greyscale image of the total intensity VLA C+D configuration HI map. The grey scale range (shown with a square root transfer function) is in units of 10^3 Jy beam^{-1} m s^{-1} and the beam is $47'' \times 32''$ at a position angle of $-8\overset{\circ}{.}2$. F1 and F2 refer to two HI extensions identified by Chaves & Irwin (2001).

2.4.3.2 Multiwavelength extraplanar features

In Fig. 2.8a and b, we compare the X-ray emission with the radio continuum emission and HI total intensity emission, respectively. Of the two radio images, the

radio continuum morphology more closely resembles the X-ray morphology in the sense that: a) the north bubble has a radio continuum counterpart; b) the south extension also has a radio continuum counterpart; c) the south-west feature shows a small radio continuum protrusion; and d) the peaks of the large eastern extensions (north and south) also show radio emission.

The HI total intensity map shown here does not show all of the extended features identified by Chaves & Irwin (2001), but two of their features, F1 and F2 clearly extend above and below the galactic plane and are labelled in Fig. 2.8b. These two features might be related with the northern and southern arc of the eastern extensions seen in the X-ray.

It is not wise to read too much into these correlations, given the limited S/N of the maps. However, the relationship with the radio continuum is sufficiently strong that the X-ray emission in the extraplanar features, representing hot diffuse gas, is very likely associated with the radio continuum emission which represents predominantly the non-thermal component.

We further consider the energetics of a specific feature, namely the "north bubble", which is the only extraplanar feature that can be cleanly isolated from the ambient emission. Guided by Fig. 2.9, we approximate the volume occupation of the bubble by a cylinder with $1'$ in diameter and $0.8'$ in height, the center of which is $1.2'$ above the galactic center. Hence the volume of the bubble is $\sim 2.7 \times 10^2$ kpc^3. We find a total 0.5-2 keV count rate of 2.4×10^{-3} cts s^{-1} within the bubble. In the best-fit model to the spectra of unresolved emission, the high and low temperature components predict a 0.5-2 keV count rate of 7.5×10^{-3} cts s^{-1} and 2.0×10^{-3} cts s^{-1}, respectively. Therefore the north bubble is unlikely to be due to the low temperature component alone. Instead, it could be dominated by the high temperature component. Taking an effective temperature of ~ 0.8 keV, we estimate the mean density of the bubble to be $\sim \eta^{-1/2} \times 10^{-3}$ cm^{-3}, where η is the filling factor of the hot gas inside the bubble. The
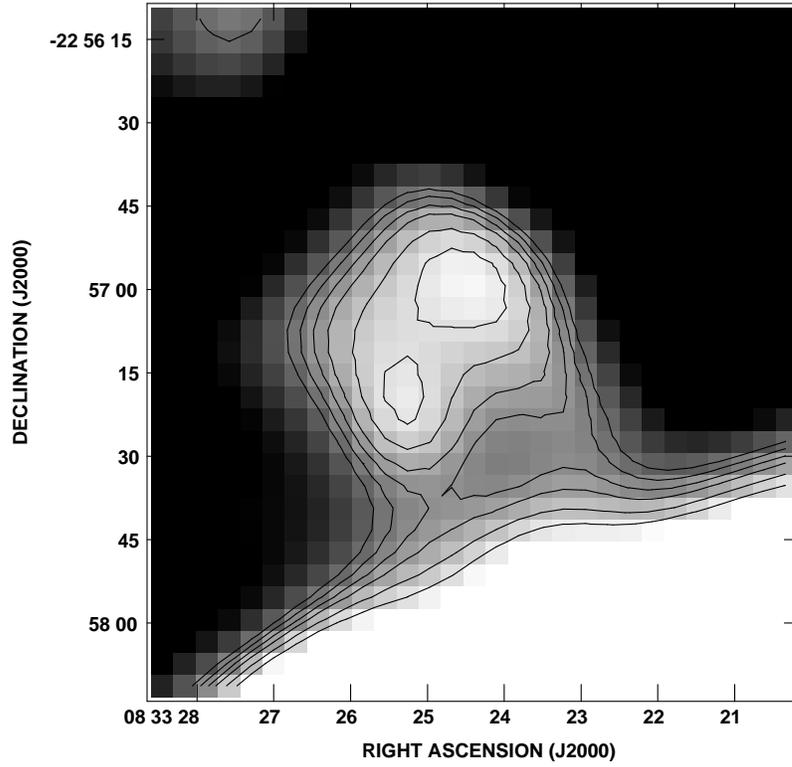
Figure 2.9 The X-ray-emitting bubble to the north of the nucleus. The same X-ray intensity image as in Fig. 2.4 is used. Contour levels are at 5, 5.2, 5.4, 5.6, 5.9, and 6.2×10^{-3} cts s^{-1} arcmin^{-2}.

total thermal energy of the bubble is $E_{th} \simeq 3.6\eta^{-1/2} \times 10^{55}$ ergs s^{-1}, and the work done to steadily lift up the bubble against gravity is $E_g \simeq 1.7\eta^{-1/2} \times 10^{55}$ ergs s^{-1}, given the gravitational potential introduced by the exponential disk of the galaxy (Irwin & Chaves 2003). Given the morphology and the position of the bubble, we speculate that it was produced near the nuclear region, either by a nuclear starburst or the AGN. If the bubble's total amount of thermal and gravitational energy is obtained from a starburst, it takes a time of $\tau \simeq (E_{th} + E_g)/(fL_{SNII}) \simeq 1.7\eta^{-1/2} \times 10^7$ yr to form the present structure, where f is a geometrical factor taken to be 0.1 to reflect a fractional star formation rate of the central 1 kpc in the disk. This timescale is typical for massive stars to become SN explosions. On the other hand, assuming the flux

density of the AGN follows $S_\nu \propto \nu^{-\alpha}$ between the radio and X-ray bands, the total bolometric luminosity over this frequency range is $\sim 4.5 \times 10^{40}$ ergs s^{-1} with $\alpha = 0.62$ adopted (§ 2.4.1). It is uncertain what fraction of the AGN energy can be taken to energize the ambient gas, but we consider that the AGN might also be capable of producing this feature. For example, the locations of the north bubble and south extension immediately on either side of the nucleus are reminiscent of extraplanar loops or lobes seen in nuclear outflow galaxies like NGC 3079 (e.g. Cecil et al. 2002) which is known to have an AGN.

2.5 Summary

We have analyzed an *XMM-Newton* observation of the massive edge-on Sb galaxy NGC 2613. We find a deeply embedded AGN in this galaxy. The X-ray spectrum of this AGN can be characterized by a power-law model with a photon-index of $\sim$2 and a 0.3-10 keV intrinsic luminosity of 3.3×10^{40} ergs s^{-1}. Linking the X-ray spectral properties of the AGN with the current upper limit at radio frequencies indicates a spectral flattening of the AGN at low frequencies.

The 0.5-2 keV unresolved X-ray emission is found to closely trace the near-IR emission in the disk region, and the X-ray to near-IR luminosity ratio is consistent with that inferred from galactic LMXBs. These two facts together indicate that the bulk of the unresolved emission is produced by the old stellar population of the galaxy, predominantly LMXBs.

A few extraplanar diffuse X-ray features are present in addition to the collective emission from discrete sources traced by the near-IR light. These features can be explained by the presence of hot gas, which can be spectrally characterized by a two-temperature plasma with $kT \sim$0.08 keV and $\sim$0.8 keV. The total X-ray luminosity of hot gas is at least an order of magnitude lower than that predicted by current

simulations of IGM accretion based on disk galaxy formation models. Thus the extraplanar features are very unlikely to result from IGM accretion.

Instead, morphologically most of these extraplanar features have extended radio counterparts, which are believed to arise from disk-related events. Also, energetically the extraplanar features can be generated by either supernova explosions or the AGN, the latter possibly related to the bubbles above and below the nucleus. Therefore, we conclude that the extraplanar features are most likely formed from outflows from the galactic disk.

Our observation suggests that a proper inclusion of galactic feedback is essential, not only to understanding galaxy formation, but also to its continued evolution. NGC 2613 and galaxies like it provide nearby laboratories that may help to understand the over-cooling problem existing in current galaxy formation simulations.

CHAPTER 3

CHANDRA AND *XMM-NEWTON* DETECTION OF LARGE-SCALE DIFFUSE X-RAY EMISSION FROM THE SOMBRERO GALAXY

3.1   Introduction

Galactic bulges are an important component of early-type spiral galaxies. X-ray studies of the high-energy phenomena and processes in galactic bulges provide a vital insight into our understanding of galaxy formation and evolution. Several facts make the Sombrero Galaxy (M104; NGC4594; Table 3.1) an ideal target for such a study: 1) This nearby Sa galaxy is massive (circular rotation speed of ~ 370 km s^{-1}) and bulge-dominated, and hence a potential site for probing a large amount of hot gas from intergalactic accretion (e.g., Toft et al. 2002) and/or internal stellar feedback (e.g., Sato & Tawara 1999); 2) The high inclination of the galaxy (84°) allows for a clean separation between the disk and bulge/halo components; 3) A well-determined distance (8.9 ± 0.6 Mpc) of the galaxy minimizes the uncertainty in the measurement of X-ray luminosities; 4) As indicated by its very low specific far-infrared and diffuse radio fluxes (Bajaja et al. 1988), the galaxy shows little indication for recent star formation, minimizing the possibility of heating and/or gas ejection from the galactic disk; 5) The galaxy is isolated and thus uncertainties resulting from galaxy interaction are miminal. Therefore, M104 is particularly well-suited for an X-ray study of high-energy stellar and interstellar products in a galactic bulge and their relationship to the galactic disk and to the intergalactic environment.

Existing X-ray studies of M104 have focused on its discrete X-ray sources. Di Stefano et al. (2003) reported the detection of 122 X-ray sources, based on a *Chandra*

Table 3.1.   Basic Information of M 104

Parameter	M 104
Morphology[a]	SA(s)a
Center position[a]	R.A. $12^{\rm h}39^{\rm m}59^{\rm s}\!.43$
(J2000)	Dec. $-11°37'23''\!.0$
Optical size[a]	$8'\!.7 \times 3'\!.5$
Inclination angle[b]	$84°$
B-band magnitude [a]	8.98
V-band magnitude [a]	8.00
K-band magnitude [a]	4.96
Circular speed (km s^{-1})[c]	370
Distance (Mpc)[d]	8.9
....	$(1' \stackrel{\scriptscriptstyle\wedge}{=} 2.59{\rm kpc})$
Redshift[a]	0.00342
Galactic foreground $N_{\rm HI}$ (10^{20} cm^{-2})[e]	3.7

References. —   a. NED; b. Rubin et al. (1985); c. Wagner, Dettmar & Bender (1989); d. Ford et al. (1996); e. Dickey & Lockman (1990).

ACIS-S observation of the galaxy. In particular, they classified a population of very soft X-ray sources, which tend to concentrate in the core region of the galactic bulge. Wang (2004) conducted a careful analysis of the luminosity function of the discrete X-ray sources detected from the same observation by correcting for incompleteness and Eddington bias in the source detection and by removing statistical interlopers in the field. The X-ray behavior of the central AGN has been studied by Pellegrini et al. (2003), based on an *XMM-Newton* observation as well as the *Chandra* data.

We here report a systematic analysis of the *XMM-Newton* and *Chandra* observations (Figs. 3.1 and 3.2), focusing on the study of diffuse X-ray emission in M104. The *Chandra* data, with superb spatial resolution, are well-suited for the study of the galaxy's inner region where the X-ray source density is high. However, the FOV of the *Chandra* ACIS-S, especially that of the S3 chip ($\sim 8' \times 8'$), does not provide a full coverage of the large-scale X-ray emission of the galaxy (cf. Fig. 3.3). The *XMM-Newton* EPIC observation, on the other hand, has a substantially larger FoV,

allowing us to probe the extent of the global diffuse X-ray emission. The combination of the two observations thus provides us with the most comprehensive X-ray view of the galaxy.
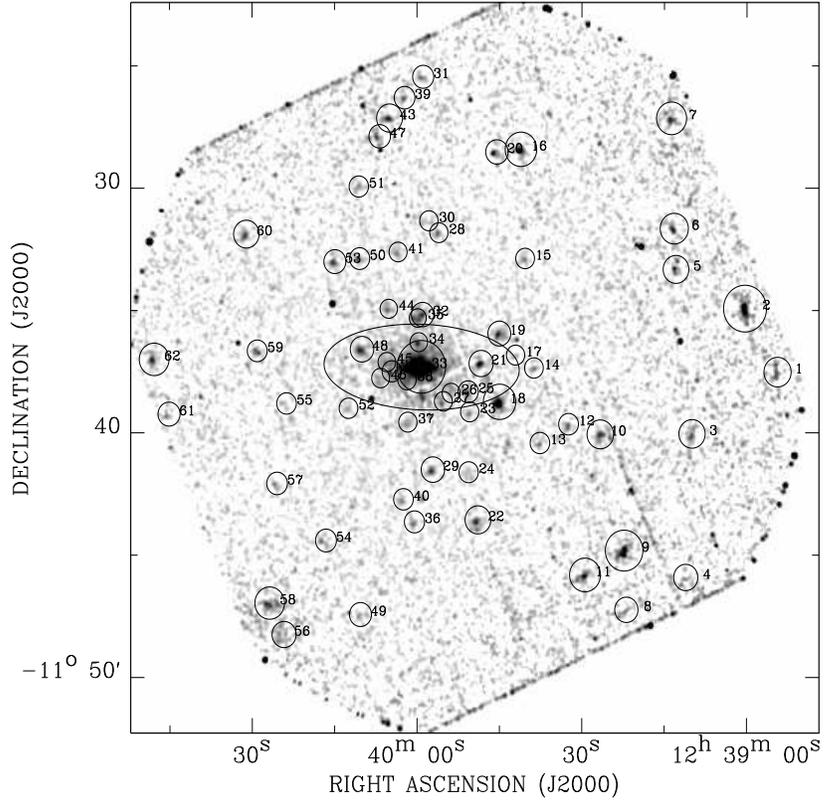
Figure 3.1 EPIC-PN intensity image of the M 104 field in the 0.5-7.5 keV band after a flat-fielding. An adaptively smoothed background has been subtracted from the image to highlight discrete sources which are outlined with circles for source-removal (see § 3.4.1). The ellipse ($8.'7 \times 3.'5$) illustrates the optical $I_B = 25$ mag arcsec^{-2} isophote of the galaxy.

3.2   Observations and Data Reduction

3.2.1   *Chandra* **observations**

The *Chandra* ACIS-S observation of M104 (Obs. ID. 1586) was taken on May 31, 2001, with an exposure of 18.8 ks. Our work uses the data primarily from the on-axis S3 chip, although part of the adjacent FI chips (S2 and S4) are also included
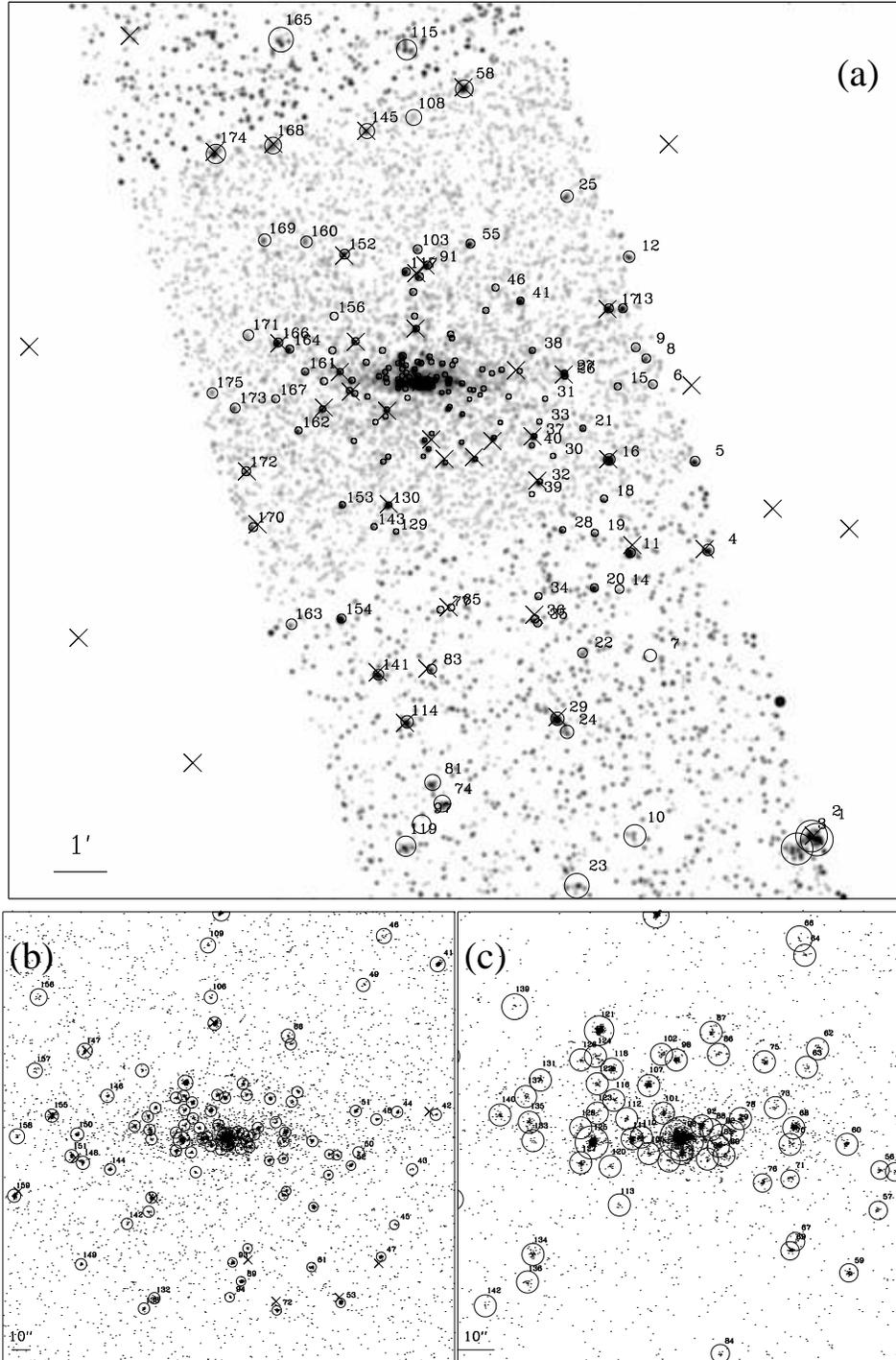
Figure 3.2 ACIS-S 0.3-7 keV band intensity images: (a) the whole source detection field, over which the image is smoothed with a Gaussian of FWHM equal to $3''.9$; (b) the inner $\sim 4' \times 4'$ region around the center of M 104; (c) the very central $\sim 2' \times 2'$ region around the galactic center. Detected X-ray sources are outlined with circles for source-removal (see § 3.4.1). Positions of sources detected by the EPIC-PN are marked with *crosses*.
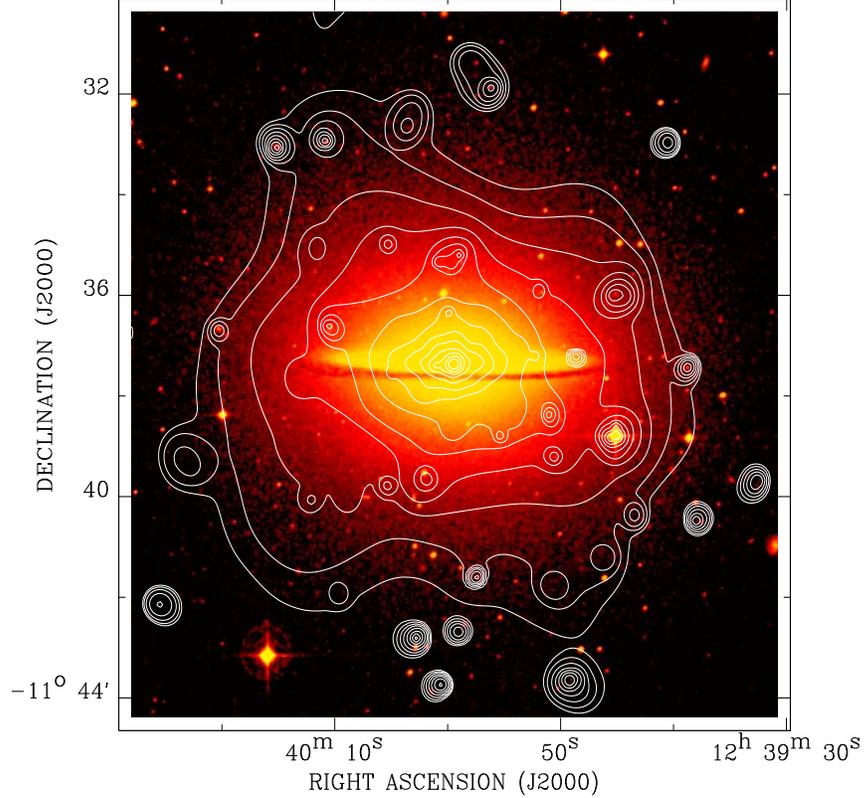
Figure 3.3 EPIC-PN 0.5-2 keV intensity contours overlaid on the digitized sky-survey blue image of M 104. The X-ray intensity is adaptively smoothed with the CIAO *csmooth* routine with a signal-to-noise ratio of ~ 3. The contours are at (1.4, 1.8, 2.6, 4.2, 7.4, 13.8, 27, 52, 103, 206, 411, 820, and 1640)$\times 10^{-3}$ cts s^{-1} arcmin^{-2} above a local background level of 2.0×10^{-3} cts s^{-1} arcmin^{-2}.

in the source detection. We reprocessed the *Chandra* data, using CIAO, version 3.2.1 and the latest calibration files. We also removed time intervals with significant background flares, i.e., those with count rates $\gtrsim 3\sigma$ and/or a factor of $\gtrsim 1.2$ off the mean background level of the observation. This cleaning resulted in an effective exposure of 16.4 ks for subsequent analysis. We created count and exposure maps in the 0.3-0.7, 0.7-1.5, 1.5-3, and 3-7 keV bands. Corresponding background maps were created from the "stowed background" data, which contain only events induced by the instrumental background. A normalization factor of ~ 1.05 was applied to the

exposure of this "stowed background" data in order to match its 10-12 keV count rate with that of Obs. 1586.

3.2.2 *XMM-Newton* observations

The *XMM-Newton* EPIC observation of M104 (Obs. ID 0084030101) was taken on December 28, 2001, with the thin filter and with a total exposure of 43 ks. We calibrated the data using SAS, version 6.1.0, together with the latest calibration files. In this work, we only use the EPIC-PN data. We found that a large fraction of the observation was strongly contaminated by cosmic-ray-induced flares. To exclude these flares, we removed time intervals with count rates greater than 11 cts s^{-1} in the 0.2-15 keV band, about a factor of 1.2 above the quiescent background level, and some additional intervals with residual flares found in sub-bands. The remaining exposure is only 10.8 ks for the PN. We then constructed count and exposure maps in the 0.5-1, 1-2, 2-4.5, and 4.5-7.5 keV bands for flat-fielding. We also created corresponding background maps from the "filter wheel closed" (FWC) data , chiefly for instrumental X-ray background subtraction. However, we found that at energies above 5 keV the spectral shape of the instrumental background of Obs. 0084030101 is apparently different from that of the FWC data, making a simple normalization inapplicable. Therefore, the FWC data are only used in producing large-scale images. Background adoption for spectral analysis will be further discussed in § 3.4.2.

3.3 Discrete X-ray sources

Fig. 3.3 shows the overall 0.5-2 keV X-ray intensity image of M104 obtained from the PN. The morphology appears more-or-less symmetric, reminiscent of the optical light distribution of the galaxy. The X-ray emission likely represents a combined contribution from discrete sources and truly diffuse hot gas. We first detect individual

sources and characterize their properties. Then we try to isolate and study the diffuse X-ray component in § 3.4.

We detect 62 *XMM-Newton* and 175 *Chandra* discrete X-ray sources. The source detection is carried out for each observation in the broad (B), soft (S), and hard (H) bands, defined differently for the ACIS-S and PN data, as noted in the tables. Following the procedure detailed in Wang (2004), we use a combination of source detection algorithms: wavelet, sliding-box, and maximum likelihood centroid fitting. The map detection and the maximum likelihood analysis are based on data within the 50% PSF energy-encircled radius (EER) for the PN and the 90% EER for the ACIS-S. The accepted sources all have a local false detection probability $P \leq 10^{-6}$.

The source locations are marked in Figs. 3.1 and 3.2. Essentially all PN sources within the field of Fig. 3.2a are also detected in the ACIS-S data. All relatively bright ACIS-S sources, except for those in the nuclear region, are detected in the PN data. These consistencies indicate no strong variability of the sources between the two observations. Source confusion is serious for the PN data, because of the limited spatial resolution. Some of the PN detections represent combinations of multiple discrete sources, This is particular the case in the nuclear region (Fig. 3.2c).

We note that the source detection limit is significantly higher in the PN data than in the ACIS-S data. The majority of detected sources are of two populations: sources associated with the galaxy and extragalactic sources mostly being background AGNs. Applying the luminosity function (LF) of the AGNs obtained by Moretti et al. (2003), we estimate the number of detected AGNs to be 15.5 (2.3) in the ACIS-S (PN) FoV.

We further obtain an accumulated ACIS-S spectrum of the sources to characterize their average spectral property. The spectrum is extracted from sources within the $I_B = 25$ mag arcsec^{-2} isophote (D_{25} ellipse; $8.'7 \times 3.'5$), except for the nuclear source and the three bright sources discussed above. The total number of included sources is $\sim$110. For each source, a circular region of twice the 90% EER is adopted for

accumulating the spectrum. A background spectrum is extracted from the rest region of the ellipse. In the PN data, only ten sources are detected within the D_{25} ellipse and four of them are located within $1.\!'5$ from the galactic center, where the emission of the nucleus largely affects. Therefore, we do not analyze an accumulated source spectrum from the PN.

We use an absorbed power-law model to fit the accumulated spectrum, with the absorption being at least that supplied by the Galactic foreground. The model offers an acceptable fit to the spectrum ($\chi^2/d.o.f. = 115.2/144$), giving a best-fit photon index of $1.51^{+0.10}_{-0.09}$ and a 0.3-7 keV intrinsic luminosity of $\sim 2.6 \times 10^{40}$ ergs s^{-1}. All quoted errors in this paper are at the 90% confidence level. The slope of the power-law is typical for composite X-ray spectra of LMXBs observed in nearby galaxies (e.g., Irwin, Athey & Bregman 2003). We note that none of the included sources contributes more than 5% of the total counts to the accummulated spectrum. Therefore, the spectrum, along with the fitting model, can be used to characterize the average spectral property of sources.

3.4 The unresolved X-ray emission

Our main interest here is in the diffuse X-ray emission from M104 A first step towards isolating the diffuse emission is to subtract the detected discrete sources from the images. To do so, we exclude regions enclosing twice the 50% (90%) EER around each PN (ACIS-S) source with a count rate $(CR) \lesssim 0.01$ cts s^{-1}. For brighter sources, a factor of $1 + \log(CR/0.01)$ is further multiplied to the source-subtraction radius. Our choice of the regions is a compromise between excluding a bulk of the source contribution and preserving a sufficient field for the study of the unresolved emission. With the above criteria about 80% (95%) of photons from individual sources are removed from the PN (ACIS-S) image.

The unresolved emission presumably consists of two components: the emission of truly diffuse gas and the collective discrete contributions from the residual emission of detected sources and the emission of undetected sources below our detection limit. In practice, the discrete component can be constrained from its distinct spatial distribution and spectral property. Below we isolate the two components and characterize the properties of the diffuse emission.

3.4.1 Spatial properties

3.4.1.1 Surface intensity profiles

We construct instrumental background-subtracted and exposure-corrected galactocentric radial surface intensity profiles for the source-subtracted emission, in the soft (0.5-1 keV for the PN; 0.3-0.7 keV for the ACIS-S), intermediate (1-2 keV for the PN; 0.7-1.5 keV for the ACIS-S) and hard (2-7.5 keV for the PN; 1.5-7.0 keV for the ACIS-S) bands (Fig. 3.4). While the ACIS-S instrumental background is determined from the "stowed background" data, the instrumental background rates in the PN bands are predicted from the spectral fit to a local PN background spectrum (see § 3.4.2). Spatial binning of annuli is adaptively adjusted to achieve a signal-to-noise ratio better than 3, with a minimum step size of $6''$ for the PN and $3''$ for the ACIS-S. For the PN profiles, the central $1.'5$ is heavily contaminated by the emission from the nucleus. Thus our analysis for the PN data is restricted to radii beyond $1.'5$. The ACIS-S data, while being capable to probe the central region, are limited by its FoV. Therefore we restrict our analysis of the ACIS-S profiles within $3.'5$, a maximal radius where complete annuli can be extracted.

It is known that M104 has a prominent dust lane (e.g., Knapen et al. 1991; cf. Fig. 3.3), which may significantly absorb soft X-rays from the galaxy and hence introduce a bias to the bin-averaged intensity. Therefore when constructing the intensity profiles we exclude a region encompassing the dust lane. We use the digitized
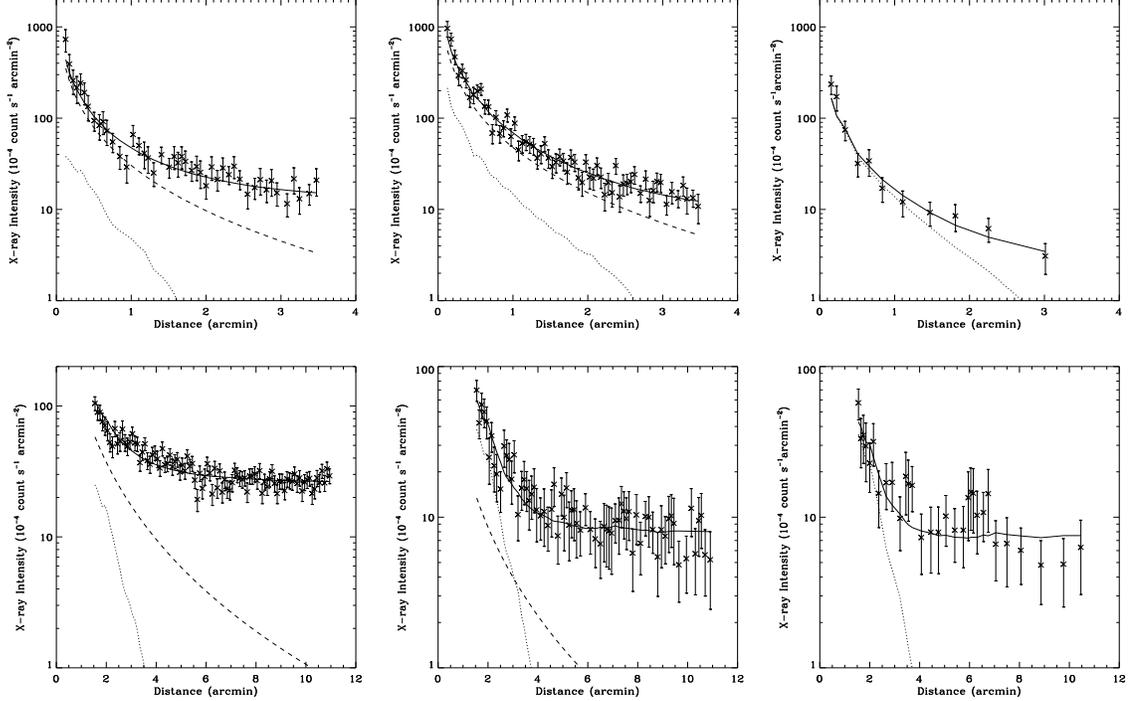
Figure 3.4 Radial surface intensity profiles of the instrumental background- and detected source-subtracted emission from M 104. *Top*: ACIS-S profiles in the 0.3-0.7 keV (*left*), 0.7-1.5 keV (*middle*) and 1.5-7 keV (*right*) bands. *Bottom*: PN profiles in the 0.5-1 keV (*left*), 1-2 keV (*middle*) and 2-7.5 (*right*) bands. The solid curves present model characterizations: a normalized K-band radial profile for emission from discrete sources (dotted curves), a de Vaucouleur's law (dashed curves) for emission from diffuse hot gas, and a local constant cosmic background. See text for details.

sky-survey blue image of the galaxy to map such a region of extinction, in which a pixel is adopted as the region bounary if it is dimmed by a factor ≥1.5 compared to the adjacent bright pixel. Visual inspection on the ACIS-S image indicates that our adopted region is coincident with a region of few registered soft X-ray photons.

To constrain the discrete component, we assume that its spatial distribution follows the near-IR light of the galaxy, which can be determined from the 2MASS K-band map (Jarrett et al. 2003). We first exclude from the map bright foreground stars and circular regions used for subtracting the discrete X-ray sources. The K-band radial intensity profile is then produced in the same manner as for the X-ray profiles. It is reasonable to assume that the discrete component dominates the X-ray emission in

Table 3.2.　Fits to the radial surface brightness profiles[a]

Parameter	PN 0.5-1 keV	PN 1-2 keV	PN 2-7.5 keV	ACIS-S 0.3-0.7 keV	ACIS-S 0.7-1.5 keV	ACIS-S 1.5-7 keV
$\chi^2/d.o.f$.................	108.0/93	46.7/69	12.5/22	32.2/43	56.1/62	6.2/9
I_g (cts s^{-1} arcmin^{-2})	$4.9^{+3.3}_{-2.6}$	$1.1^{+0.7}_{-0.5}$	-	$1.3^{+0.8}_{-0.5}$	$2.0^{+1.3}_{-0.9}$	-
r_e (arcmin)...............	$2.6^{+1.4}_{-0.9}$	same	-	same	same	-
[b]I_s......................	13.2	20.1	$18.7^{+4.7}_{-4.7}$	1.0	2.9	$2.8^{+0.5}_{-0.5}$
I_b (10^{-4} cts s^{-1} arcmin^{-2})	$25.6^{+1.0}_{-0.7}$	$7.8^{+0.9}_{-0.9}$	$7.5^{+1.5}_{-1.5}$	$11.8^{+2.3}_{-2.3}$	$6.7^{+1.9}_{-1.8}$	$2.8^{+1.3}_{-1.2}$

Note. — [a] The profiles are fitted by a normalized K-band profile plus a local constant background, $I_X(R)= I_s I_K(R) + I_b$, for the PN 2-7.5 keV and ACIS-S 1.5-7 keV bands, or with an additional de Vaucouleur's law, $I_X(R)= I_s I_K(R) + I_g\ e^{-7.67(R/r_e)^{1/4}} + I_b$, for the softer bands. [b] The normalization factors for different bands, in units of 10^{-4} cts s^{-1} arcmin^{-2}/(MJy sr^{-1}), are related via the best-fit spectral model to the accumulated source spectrum (§ 3.3).

the hard band. Thus we use the K-band profile to fit the X-ray hard band profiles, constructed from the PN and ACIS-S data. The fitting parameters are the X-ray-to-K-band intensity ratio of the underlying stellar content (I_s) and a constant intensity (I_b) to account for the local cosmic X-ray background. We find that the X-ray hard band profiles can be well characterized by the K-band profile (Fig. 3.4; Table 3.2).

We further assume that the discrete component has a collective spectral property same as that modeled for the detected sources (§ 3.3). This allows us to use the hard band intensity to constrain the discrete component in the soft and intermediate bands. The diffuse component is then determined for these two bands by subtracting the discrete component from the total intensity profile. We then fit the radial distribution of the diffuse component with a de Vaucouleur's law:

$$I(R) = I_g\ e^{-7.67(R/r_e)^{1/4}}, \tag{3.1}$$

where R is the projected galactocentric radius, r_e the half-light radius and I_g the central surface intensity. A paramter I_b is also included to account for the local cosmic X-ray background. Due to the partial coverage of the overall distribution by each profile, we require in the fit that the half-light radii be identical for all profiles.

We find that this characterization offers good fits to the profiles (Fig. 3.4; Table 3.2). The best-fit half-light radius is $2'\!.6^{+1'\!.4}_{-0'\!.9}$. In comparison, the K-band half-light radius is $\sim 1'$ (~ 2.6 kpc; Jarrett et al. 2003). This suggests that the distribution of hot gas is substantially more extented than that of the stellar content.
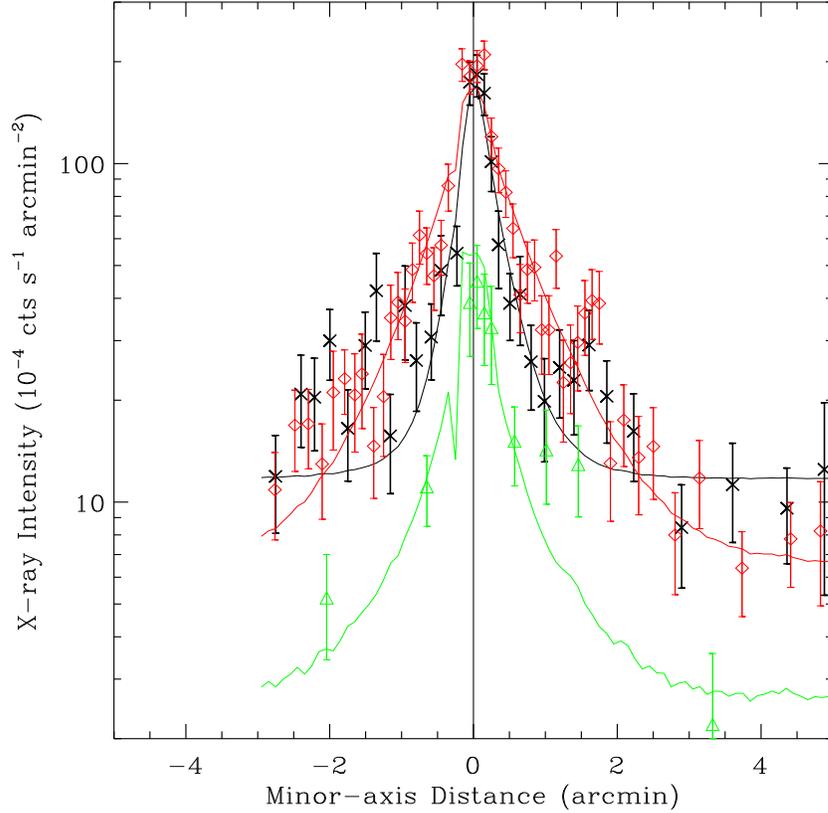
Figure 3.5 ACIS-S intensity distribution along the direction perpendicular to the disk of M 104, in the 0.3-0.7 keV (*black crosses*), 0.7-1.5 keV (*red diamonds*), and 1.5-7 keV (*green triangles*) bands. The full width along the direction parallel to the major axis used for averaging the intensity is $4'$ (~ 10 kpc). The adaptive steps along the minor axis achieve a signal-to-noise ratio greater than 3, with a minimum of stepsize of $6''$. The vertical line represents the position of the major axis of the disk, whereas the horizontal axis marks the vertical distance along the minor axis (south as negative).

We also construct vertical intensity profiles of the source-subtracted emission along the galaxy's minor axis for the ACIS-S 0.3-0.7, 0.7-1.5 and 1.5-7 keV bands (Fig.3.5). In general, the intensity decreases rapidly with the off-disk distance. We follow the above procedure to decompose the diffuse and discrete components of the vertical

Table 3.3.   Fits to the vertical surface intensity profiles[a]

Parameter	ACIS-S 0.3-0.7 keV	ACIS-S 0.7-1.5 keV	ACIS-S 1.5-7 keV
$\chi^2/d.o.f.$.............................	47.2/28	70.4/45	10.5/8
I_g (10^{-4} cts s^{-1} arcmin^{-2})...........	160^{+30}_{-30}	110^{+14}_{-14}	-
[b]z_0 (arcmin).........................	$0.22^{+0.05}_{-0.05}$, $0.31^{+0.06}_{-0.06}$	$0.64^{+0.08}_{-0.08}$, $0.72^{+0.09}_{-0.09}$	-
[c]I_s (10^{-4} cts s^{-1} arcmin^{-2}/[MJy sr^{-1}])	1.0	2.9	2.8
[c]I_b (10^{-4} cts s^{-1} arcmin^{-2})...........	11.8	6.7	2.8

Note. — [a]The 1.5-7 keV profile is fitted by a normalized K-band profile plus a local constant background: $I_X(z)= I_s I_K(z) + I_b$. For the softer bands, an additional exponential law is applied: $I_X(z)= I_s I_K(z) + I_g\, e^{-|z|/z_0} + I_b$. [b]The first and the second values are for the south and north sides, respectively. [c] Same normalization factors and local background rates are applied as for the radial profiles (Table 3.2).

profiles. An exponential law, i.e., $I(z) = I_g\, e^{-|z|/z_0}$, is used to fit to the vertical distribution of the diffuse component. The scale height z_0 is allowed to be different between the south and north sides of the midplane. The fit is marginally acceptable, with excess existing at $\sim 2'$ from the midplane on both sides. Fit results (Table 3.3) show that in each band there is no significant asymmetry in the intensity distribution with respect to the midplane. The best-fit scale height in the soft band ($\sim 1/4$ arcmin) is less than that in the intermediate band ($\sim 1/3$ arcmin), indicating that emission is softer in the central region than in the extraplanar region. When the above fit is restricted to a vertical distance $\geq 0\overset{'}{.}5$, the best-fit scale heights for the soft and intermediate bands are nearly identical ($\sim 1'$). This is evident that the temperature of hot gas around the disk plane is lower than that in the bulge.

3.4.1.2   Inner region and substructures

We use the ACIS data to probe the diffuse X-ray properties in the inner region of the galaxy. We fill the holes from the source removal with the values interpolated from surrounding bins. Fig. 3.6 shows "diffuse" X-ray intensity contours, which are substantially less smoothed than presented in Fig. 3.3. There are considerable sub-

structures in the inner region. Inner contours are extended more to the north than to the south (where strong intensity gradients are found), indicating a heavier absorption of X-ray emission to the south. This is clearly due to the prominent dust lane that lies at the $10''$ -$25''$ range to the south of the major axis (Knapen et al. 1991). The intensity contours also become strongly elongated along the galactic disk.

Fig. 3.6 also presents in grey scale a continuum-subtracted Hα image of M104, obtained with the 0.9 meter telescope at Kitt Peak National Observatory in 1999. The details of observations are presented elsewhere (Hameed & Devereux 2005). Hα emission is distributed, primarily, in an annulus, and individual HII regions can be identified on the ring. There is some Hα emission within the ring, but it is difficult to tell from the image if the emission is diffuse or if it contains HII regions. The Hα ring follows the optical dust lane but is located on its inner side. High extinction possibly obscures ionized emission from the dust lane itself.

Total Hα flux for M104, uncorrected for internal or external extinction, is calculated to be $\sim 0.8 \times 10^{-12}$ ergs s^{-1} cm^{-2}, which translates to a luminosity of $\sim 7.6 \times 10^{39}$ ergs s^{-1}. Using Kennicutt's (1998) formula, we derive a star formation rate of ~ 0.1 M$_\odot$ yr^{-1}, which is lower than the average star formation rate (0.9 M$_\odot$ yr^{-1}) for early-type spirals (Hameed & Devereux 2005).

Fig. 3.6 shows that X-ray intensity drops abruptly in the field covered by the front side of the Hα disk, corresponding to the inner region of the cold gas disk of the galaxy. This means that the Hα-emitting region does not contribute appreciable amounts to X-ray radiation. In contrast, good Hα/X-ray correlation is typically seen in late-type spirals (e.g., Strickland et al. 2004; Wang et al. 2003). In fact, the diffuse X-ray intensity in M104 is so low in the field covered by the front side of the cool gas disk that the disk must be absorbinga large fraction of X-ray emission from the region beyond.
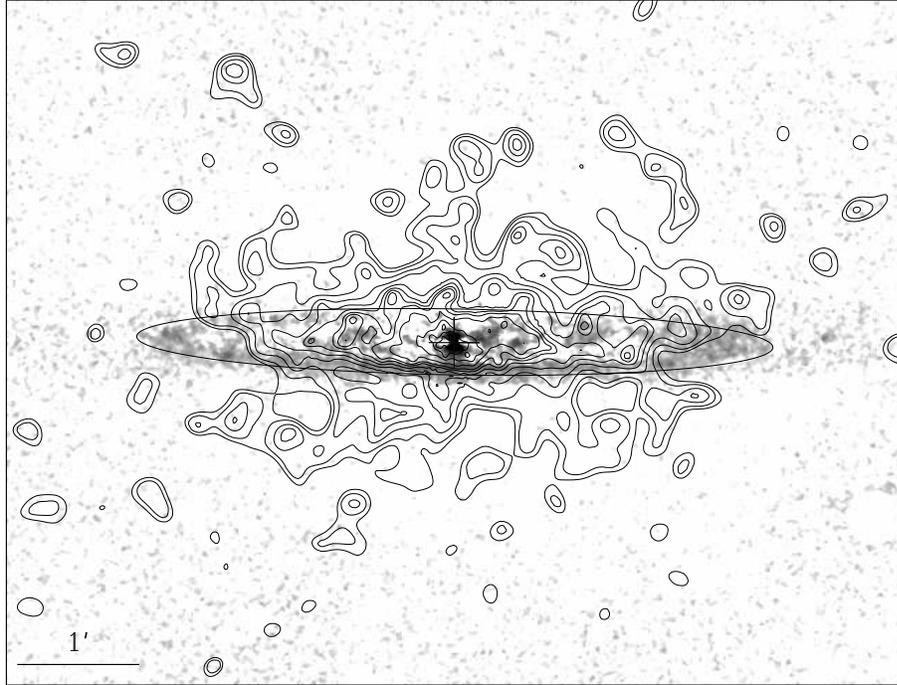
Figure 3.6 ACIS-S 0.3-1.5 keV intensity contours overlaid on the continuum-subtracted Hα image of M 104. The X-ray intensity is smoothed adaptively with a count-to-noise ratio of 4 after source-subtraction.

We probe the azimuthal variation of diffuse emission in the inner region. Fig. 3.7 shows the azimuthal ACIS-S 0.3-1.5 keV intensity distributions. The distributions deviate from axisymmetry significantly. But the deviations are largely coupled with the orientation of the bulge (0° aligns with the minor axis). When the azimuthal intensity distributions are measured within elliptical annuli with an axis ratio similar to that of the bulge (Fig. 3.7), the deviations are significantly reduced, with smaller scale fluctuations remaining in certain azimuthal ranges, especially in the inner region. For example, dips present at $\sim 200° - 250°$ and $\sim 330° - 350°$ find their counterparts in Fig. 3.6. At larger radii, only moderate deviations from axisymmetry can be seen from the azimuthal intensity distributions for the PN data. When an axis ratio of 0.8 is adopted to reflect the geomoetry of the bulge, most of the deviations vanish and no substantial fluctuations are present. This is evidence that the diffuse emission is nearly axisymmetric at large scale.
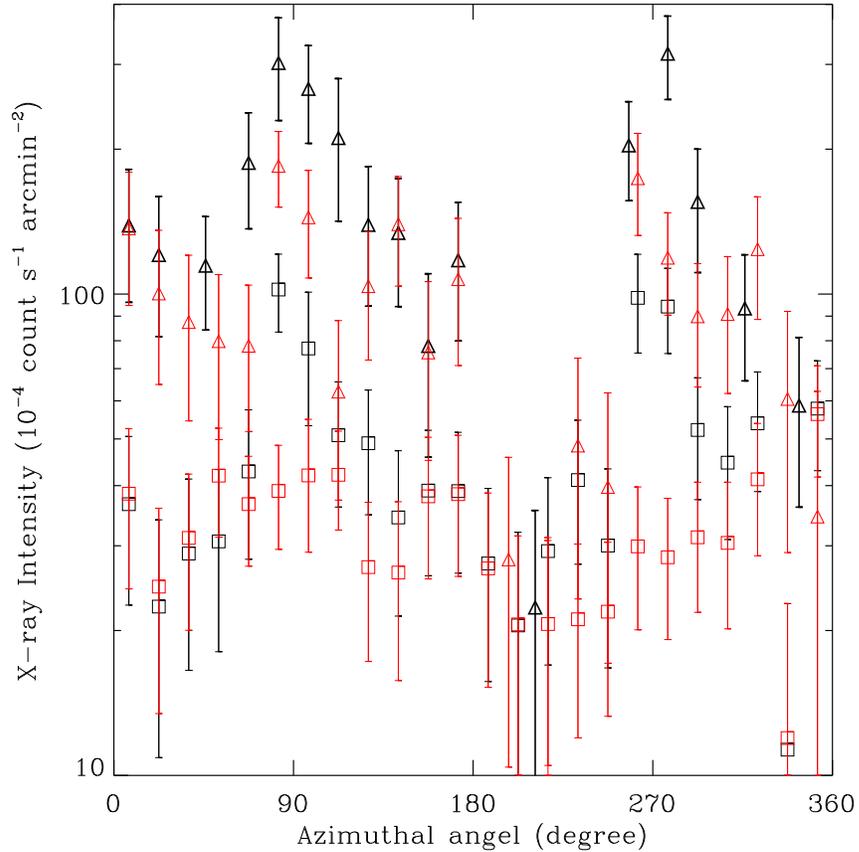
Figure 3.7 Azimuthal diffuse intensity distributions in the ACIS-S 0.3-1.5 keV band, averaged within annuli with inner-to-outer radii of 30″-1′ (black triangles) and 1′-2′ (black squares). As comparison are similar distributions (red triangles and squares) within elliptical annuli of an axis ratio of 2/3. The angle is counterclockwise from the minor axis (north). Contribution from unresolved sources is subtracted according to the underlying K-band light (§ 3.4.1; Table 3.2). Adaptive binning is taken to have a minimum step of 15° and to achieve a signal-to-noise ratio better than 3.

3.4.2 Spectral properties of the diffuse X-ray emission

With the above spatial properties in mind, we perform spectral analysis of source-subtracted emission from a series of concentric annuli around the galactic center. Specifically, spectra are extracted from two annuli with inner-to-outer radii of 30″-1′ and 1′-2′ for the ACIS-S data and two annuli of 2′-4′ and 4′-6′ for the PN data. The dust lane region (§ 3.4.1.1) is excluded from the spectral extraction.

Two factors complicate the background determination in our spectral analysis. First, the sky location of M104 is on the edge of the North Polar Spur (NPS), a Galactic soft X-ray-emitting feature (Snowden et al. 1995). The NPS introduces an enhancement to the local background, particularly at low energies. Secondly, the X-ray emission from M104 extends to at least $6'$ from the galactic center (§ 3.4.1.1). Thus a local background cannot be extracted for the ACIS-S data. While the PN FoV still allows for a local background, the vignetting effect at large off-axis angles needs to be properly corrected for in the background subtraction. Generally, this can be achieved with the "double-subtraction" procedure: a first subtraction of the non-vignetted instrumental background followed by a second subtraction of the vignetted local cosmic background. Such a procedure relies on the assumption that the template instrumental background can effectively mimic that of a particular observation.

We intend to perform the "double-subtraction" procedure to determine the background. First we extract the PN background spectrum from a source-subtracted annulus with inner-to-outer galactocentric radii of $8'$-$11'$, a region containing little emission from the galaxy (Fig. 3.4). However, at energies ≥ 5 keV, where the instrumental background is predominant, the local background spectrum is found to be significantly harder than the spectrum extracted from the FWC data. Therefore, we decide to characterize the local background spectrum of PN, both instrumental and cosmic, by a combination of plausible components. To model the instrumental background, a broken power-law plus several Gaussian lines is applied (Nevalainene, Markevitch & Lumb 2005). The modeling of the cosmic background consists of three components. Two of them are thermal (the APEC model in XSPEC), representing the emission from the Galactic halo (temperature ~ 0.1 keV) and the NPS (temperature ~ 0.25 keV; Willingale et al. 2003), respectively. The third component is a power-law with the photon index fixed at 1.4, representing the unresolved extragalactic X-ray emission (Moretti et al. 2003). Our combined model results in a good fit to

51

the local background spectrum. We note that the decomposition of the local background is not unique, especially at lower energies ($\lesssim 1$ kev). We verify our modeling by the fact that the fitted parameters of these commonly used cosmic components are in good agreement with independent measurements (e.g., Willingale et al. 2003; Moretti et al. 2003). The background spectrum in the 0.5-7 keV range, grouped to have a minimum number of 30 counts in each bin, is shown in Fig.3.8. The model, scaled according to the corresponding sky areas, is included in the following fit to the PN spectra of the unresolved emission.
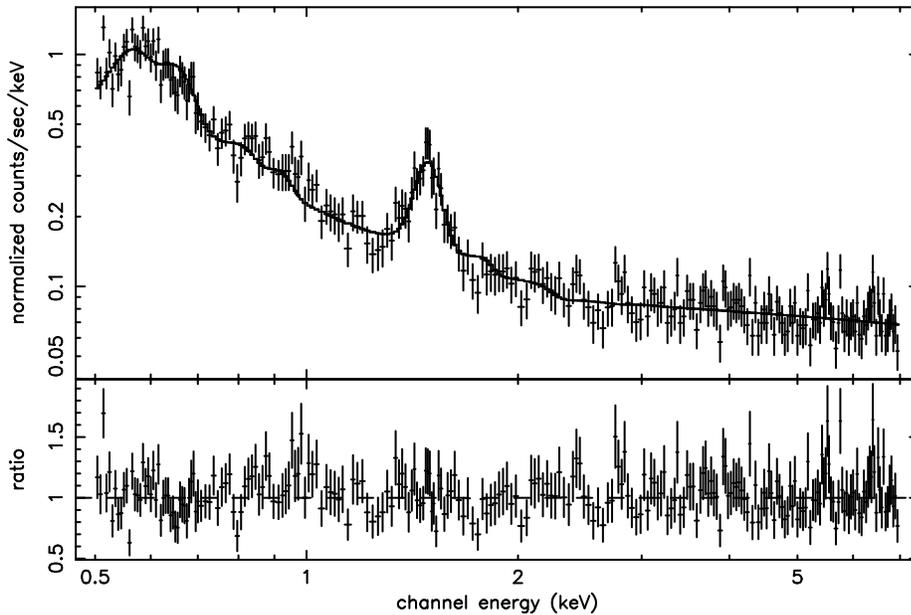
Figure 3.8 The PN background spectrum with the best-fit model. Note for a strong instrumental line at the energy of ~ 1.5 keV. See text for details.

The spectral shape of the ACIS-S instrumental background is rather stable at energies ≥ 0.5 keV[1]. Also, as the ACIS-S spectra of source-subtracted emission are extracted within the central $2'$ where the surface intensity is peaked, a small uncertainty in the instrumental background subtraction would only cause a minor effect in the analysis. Therefore, we directly subtract a "stowed backgroud" spectrum from

---

[1]http://cxc.harvard.edu/contrib/maxim/stowed/

Table 3.4.   2-D Fits to the spectra of unresolved emission[a]

Parameter	$30'' - 1'$	$1' - 2'$	$2' - 4'$	$4' - 6'$
Temperature (keV)	$0.62^{+0.09}_{-0.09}$	$0.59^{+0.07}_{-0.10}$	$0.63^{+0.07}_{-0.06}$	$0.78^{+0.13}_{-0.11}$
Abundance (solar)	$1.4\ (> 0.4)$	same	same	same
Photon index	1.51^{b}	same	same	same
Normalization (APEC; 10^{-5})	$2.3^{+0.5}_{-0.5}$	$3.6^{+0.7}_{-0.7}$	$3.8^{+0.6}_{-0.6}$	$2.7^{+0.7}_{-0.8}$
Normalization (PL; 10^{-5})	$1.1^{+0.8}_{-0.8}$	$1.2^{+1.0}_{-0.9}$	$4.0^{+0.8}_{-0.8}$	$2.1^{+1.2}_{-1.1}$
$f_{0.2-2\ \mathrm{keV}}$ (APEC; 10^{-14} ergs cm^{-2} s^{-1})	6.2	9.3	9.9	7.2
$f_{0.3-7\ \mathrm{keV}}$ (PL; 10^{-14} ergs cm^{-2} s^{-1})	7.2	8.0	26.5	14.1

Note. — The spectra extracted from four consecutive annuli are fitted by a combined model of APEC+power-law (PL) with the Galactic foreground absorption.

the ACIS-S spectra of source-subtracted emission and group them to achieve a signal-to-noise ratio better than 3. The remaining cosmic X-ray background are modeled with the same components as for the PN spectra. We note that an additional factor of 0.43, estimated from the LF obtained by Moretti et al. (2003), is multiplied to the scaling of the extragalactic component in order to account for the lower source detection limit in the ACIS-S data (Wang 2004).

The spectra show a clear line feature at $\sim$0.9 keV (Fig. 3.9), presumably due to the Fe L-shell complex contributed by the hot gas, while at energies above 1.5 keV the spectra are dominated by the residual emission of discrete sources. We account for the discrete contribution with a power-law model (PL) with a fixed photon index of 1.51 (§ 3.3), again assuming that its collective spectral shape is same as that of the detected sources. This PL, combined with a thermal plasma emission model (APEC) characterizing the emission of hot gas, is used to simultaneously fit the four spectra. Both components are subject to the Galactic foreground absorption. The temperature of the hot gas is allowed to vary, but the abundance is linked among the four spectra. We adopt the abundance standard of Grevesse and Sauval (1998) and set a physically meaningful upper limit of 10 times solar for the abundance. The

Table 3.5.   3-D Fits to the spectra of unresolved emission[a]

Parameter	$30'' - 1'$	$1' - 2'$	$2' - 4'$	$4' - 6'$
Temperature (keV)	$0.64^{+0.14}_{-0.20}$	$0.57^{+0.14}_{-0.16}$	$0.58^{+0.10}_{-0.25}$	$0.75^{+0.10}_{-0.11}$
Abundance (solar)	1.7 (> 0.4)	same	same	same
Photon index	1.51^b	same	same	same
Normalization (APEC; 10^{-5})	$2.0^{+0.7}_{-0.7}$	$2.7^{+0.8}_{-0.8}$	$4.6^{+1.1}_{-1.1}$	$4.9^{+1.5}_{-1.5}$
Normalization (PL; 10^{-5})	$1.1^{+0.8}_{-0.8}$	$1.2^{+1.0}_{-0.9}$	$4.0^{+0.8}_{-0.9}$	$2.2^{+1.2}_{-1.1}$
$f_{0.2-2 \text{ keV}}$ (APEC; 10^{-14} ergs cm^{-2} s^{-1})	6.1	9.3	10.0	7.0
$f_{0.3-7 \text{ keV}}$ (PL; 10^{-14} ergs cm^{-2} s^{-1})	7.2	8.0	26.2	14.6

Note. — The spectra extracted from four consecutive annuli are fitted by a combined model of PROJCT(APEC)+power-law (PL) with the Galactic foreground absorption, where the emission is deprojected and the parameters are measured for consecutive shells.

model gives a statistically acceptable fit to all four spectra, with the overall $\chi^2/d.o.f.$ = 481.9/511. Fit results (Table 3.4) suggest that the gas temperature vary little with radius. Interestingly, the metal abundance (> 0.4 solar) is well distinguished from very sub-solar values that were often reported in galactic X-ray studies (e.g., NGC 253, Strickland et al. 2002; NGC 4631, Wang et al. 2001). We suggest that this owes to the proper modeling of the local background, especially at energies below 0.7 keV, where the thermal continuum from the galaxy is highly entangled with the background components. An example of this kind has also been presented by Humphrey & Buote (2006), who find near-solar iron abundances for the hot gas in most of their sample early-type galaxies.

We further use the PROJCT model in XSPEC to fit the spectra for a 2-D to 3-D deprojection, i.e., the fitting parameters are measured for consecutive spherical shells. The fit is of similar significance, with a $\chi^2/d.o.f.$ = 483.2/511. Fit results are listed in Table 3.5, again indicating a quasi-isothemal hot gas with marginally super-solar abundance in the bulge of M104.

The fitted amount of the PL component in individual spectrum is verified by estimating the contribution of unresolved galactic sources. Wang (2004) obtained
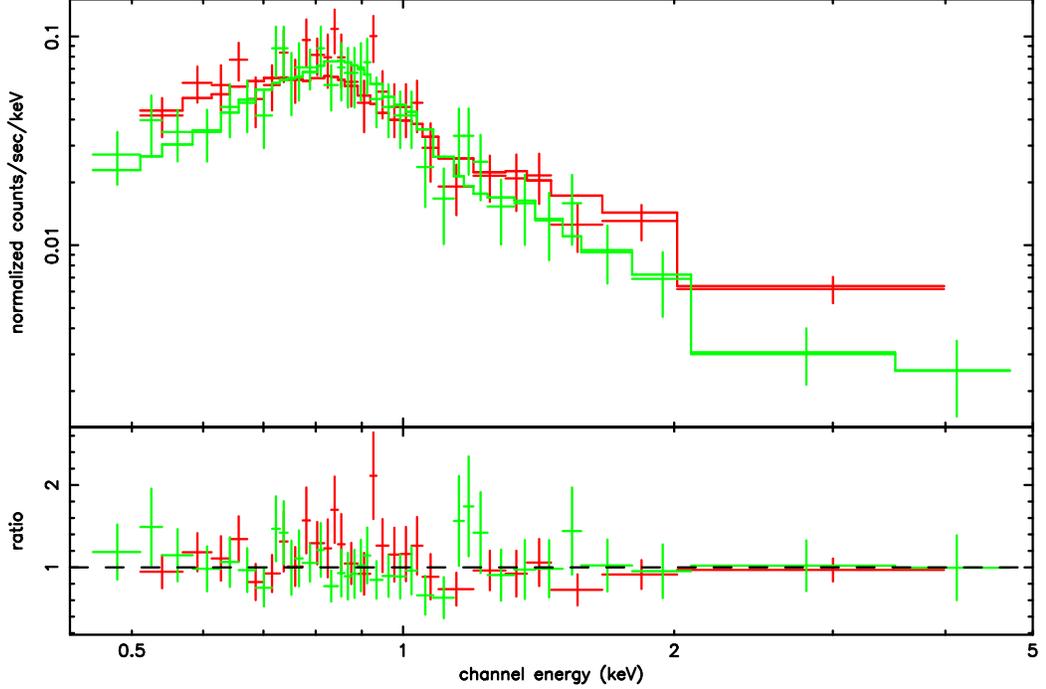
Figure 3.9 Spectra of the source-subtracted emission of M 104, extracted from concentric annuli of $30''$-$1'$ (*black*) and $1'$-$2'$ (*red*) from the ACIS-S, and $2'$-$4'$ (*green*) and $4'$-$6'$ (*Blue*) from the PN. The two ACIS-S spectra are "stowed background"-subtracted. The best-fit 3-D model (see text) is also shown.

the LF for the detected galactic sources, mostly LMXBs. Assuming that this LF is also valid for sources below the source detection limit and varies little among the regions of our spectral interest, the contribution of unresolved sources can be taken as the integrated flux from the LF, weighted by the amount of K-band light within individual annulus. We note that the integrated flux of unresolved sources in the PN is ∼4 times higher than that in the ACIS-S, due to the higher source detection limit in the PN. The fitted PL fluxes (Table 3.5) are consistent with the above estimation to within 10% (25%) for the ACIS-S (PN) spectra. The fluxes are also consistent with the X-ray-to-K-band intensity ratio obtained from the spatial analysis (Table 3.2), given a count rate to flux conversion factor predicted by the PL.

Assuming a filling factor of unity, the mean densities of hot gas are ∼6.6, 2.8, 1.2 and 0.79 $\times 10^{-3}$ cm^{-3} in the four consecutive shells with increasing radii, derived from the 3-D spectral analysis (Table 3.5). These are shown versus radius in Fig. 3.10.

Also shown is the density profile inferred from the best-fit deVaucouleur's law to the radial intensity distributions (§ 3.4.1.1; Young 1976), with the assumption that the temperature of gas is constant along with radius. This profile fairly matches the spectral measurement, indicating consistency between our spatial and spectral analyses.

As shown in § 3.4.1.2, deviations from the assumed axisymmetry are present in the diffuse emission, especially in the inner region. Nevertheless, even in the innermost annulus, the deviations would only introduce an uncertainty of 30% in the average intensity, or $\sim$15% in the measured density. Therefore, the presence of the moderate deviations does not qualitatively affect the determination of the radial structure of hot gas and its implications as we discuss below.

The total mass of hot gas contained in the shells is $\sim$4.6 $\times 10^8$ M$_\odot$ yr^{-1}, and the intrinsic 0.2-2 keV luminosity from our spectral extraction region is $\sim$ 3.1 $\times$ 10^{39} ergs s^{-1}. We note that these values can be approximated as the total mass and luminosity of hot gas in M104, given the steep density distribution (§ 3.4.1.1). For example, the luminosity within the central 6$'$ is about 75% of the total for a de Vaucouleur's distribution with a half-light radius of 2$.\!'$5.

3.5 Discussion

3.5.1 The thermal structure of hot gas

We further compare the measured density profile with that predicted from variant thermal structures that may be assumed for the hot gas. One commonly assumed case is that the gas is in hydrostatic equilibrium, i.e., the density profile is simply determined by the gravitational potential and the equation of state for the gas. A second case is that the gas is in the form of a large-scale outflow, i.e., a galactic wind (e.g., Mathews & Baker 1971; Bregman 1980; White & Chevalier 1983), in which
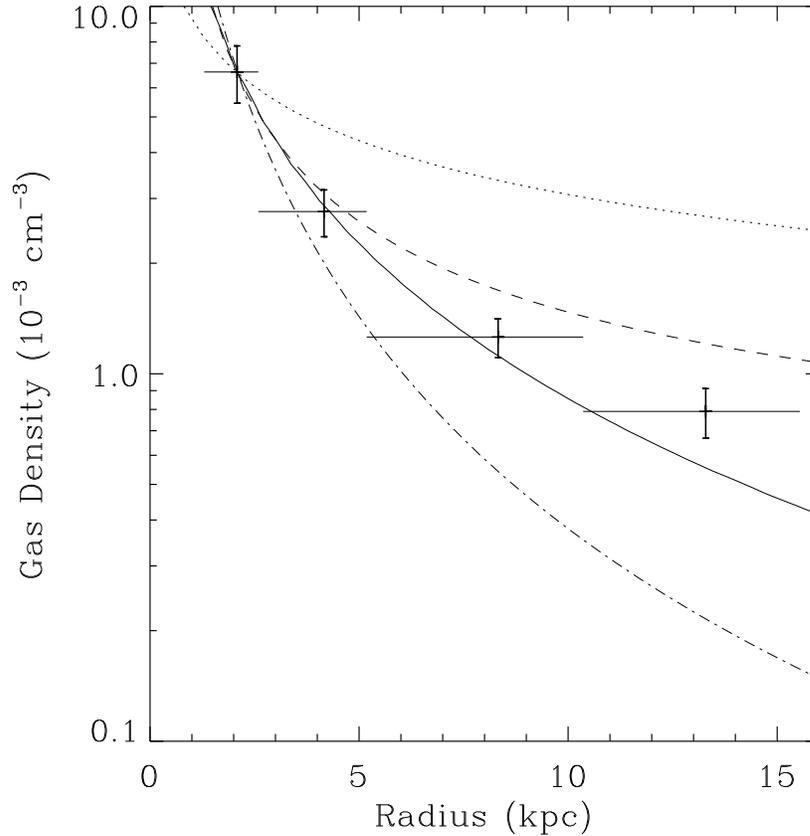
Figure 3.10 *Crosses*: the measured density of hot gas versus radius; *Curves*: the best-fit density profile to the radial surface intensity distribution (solid), the predicted density profiles of an adiabatic (dotted) or isothermal (dashed) gaseous corona in hydrostatic equilibrium and an 1-D steady galactic wind (dot-dashed). The profiles are assumed to be equal to the measurement at the first bin. See § 3.5 for details.

the physical structure of the gas is regulated by the energy and mass input from the stellar content.

We first characterize the 1-D distribution of the gravitational mass for the galactic bulge and halo. The stellar distribution in projection is assumed to follow the de Vaucouleur's law with a half-light radius of $1'$ (~ 2.6 kpc; Jarrett et al. 2003). Given the K-band magnitude of M104, the total stellar mass is estimated to be 1.6×10^{11} $M_\odot$, according to the K-band mass-to-light relation of Bell & de Jong (2001). However, Bridges et al. (1997) found a kinematic mass about three times of this value within

a projected radius of ~ 15 kpc. Therefore, a second gravitational component, i.e., dark matter, is considered. We assume that the distribution of dark matter follows the NFW profile (Navarro, Frenk & White 1996) with a scale radius of 20 kpc. This chosen scale radius is rather arbitrary but typical for a galactic dark matter halo. The mass density of the dark matter is such that the total mass (stars and dark matter) within a projected radius of 15 kpc be 5×10^{11} $M_\odot$.

For the hydrostatic equilibrium case, the density profile is calculated for two plausible states of the gas: adiabatic and an isothermal. For the galactic wind case, we have developed a simple 1-D steady dynamical model (see Appendix). Given the above distributions of stars and dark matter, the density profile of a galactic wind is determined by the rates of total energy and mass inputs to the gas which can be estimated from empirical measurements (see § 3.5.3). The measured and modeled density profiles are together shown in Fig. 3.10, in which the modeled ones are assumed to match the measurement at the first bin. We note that there is a remarkable degeneracy between the measured density and metal abundance. Since we have assumed a single abundance independent of the radius, the overall shape of the density profile is not affected by this density-abundance degeneracy.

Fig. 3.10 shows that an adiabatic gas in hydrostatic equilibrium (dotted curve) is inconsistent with the measurement, whereas neither an isothermal gas in hydrostatic equilibrium (dashed curve) nor a galactic wind (dot-dashed curve) can be completely ruled out given the relatively large uncertainties in the measurement. The isothermal case is favored by the measured temperature profile with little variation, but is subject to further considerations in which stellar feedback to the hot gas is involved (see below). A galactic wind predicts a decreasing temperature with increasing radius (e.g., Chevalier & Clegg 1985) and is apparently in contradiction with the temperature measurement. However, in the galactic wind case, gas moves rapidly outward. Beyond certain radius, the recombination timescales of some species of ions may become longer

than the local dynamical timescale. Recombinations of such ions occur at larger radii than the collisional ionization equilibrium (CIE) would predict. This process is called a "delayed reconbination" (e.g, Ji, Wang & Kwan 2006). Thermal processes from regions involving delayed reconbinations are of non-equilibrium ionization (NEI). Usually, when using a CIE plasma emission model (e.g., APEC) to fit an X-ray spectrum of hot gas, temperature is effectively determined by the position of line features that are prominent in the spectrum. Therefore, had the NEI emission from a galactic wind been observed, the measured temperature with a CIE model would be higher than the local gas temperature of the region being observed. Also, the emission measure would be higher than what the density distribution of the wind predicts. Such a possibility in M104 deserves further investigation.

3.5.2 Accretion from the intergalactic medium?

We now turn to discuss the origin of the hot gas in specific scenarios. Given the high circular rotation speed of M104 (~ 370 km s^{-1}), it is a good candidate to look for X-ray signals from an accreted gaseous halo around it. Toft et al. (2002, therein Fig. 3) predict a 0.2-2 keV X-ray luminosity of $\sim 10^{41}$ ergs s^{-1} for galaxies with circular rotation speeds similar to that of M104, about 95% of which coming from within 20 kpc of the disk. However, the observed 0.2-2 keV diffuse X-ray luminosity from M104 is only $\sim 3 \times 10^{39}$ ergs s^{-1} within the central ~ 15 kpc. Therefore, there is a remarkable discrepancy between the amount of observed extraplanar hot gas and that predicted by numerical simulations, similar to the case of NGC 2613 (§ 2). We emphasize that such a discrepancy might be due to an inadequate treatment of the stellar/AGN feedback in the simulations.

3.5.3 Stellar feedback from M104

Empirically, stars in a galactic bulge continuously deposit energy and mass to the interstellar medium (ISM) at rates of $\sim 1.1 \times 10^{40}[L_K/(10^{10}L_{\odot,K})]$ ergs s^{-1} and

$\sim 0.02[L_K/(10^{10}L_{\odot,K})]$ M$_\odot$ yr^{-1} (e.g., Mannucci et al. 2005, Knapp, Gunn & Wynn-Williams 1992), respetively, where L_B is the blue luminosity of the bulge. Both the stellar mass loss and the Type Ia SN rates are believed to be substantially greater at high redshifts when the bulges are young (e.g., Ciotti et al. 1991). Meanwhile, if the metals contained in the stellar ejecta are uniformly mixed with the ISM, the mean iron abundance of the ISM is expected to be $Z_{Fe} = Z_{*,Fe} + 9.7(M_{Fe}/0.7\mathrm{M}_\odot)$, where M_{Fe} is the iron mass yield per Type Ia SN (e.g., Nomoto, Thielemann & Yokoi 1984) and a solar iron-to-hydrogen ratio in number of 3.16×10^{-5} is adopted (Grevesse and Sauval 1998).

Had most of the stellar feeback been retained by the ISM in the galaxy since the onset of Type Ia SNe, it is expected that the observed X-ray luminosity and mass of hot gas be the amount inferred from the above energy and mass input rates. In the case of M104, $L_K = 18 \times 10^{10}L_{\odot,K}$, corresponding to an energy input rate of $\sim 2.0\times10^{41}$ ergs s^{-1} and a mass input rate of ~ 0.4 M$_\odot$ yr^{-1}, or a total mass input of 4×10^9 M$_\odot$ over a period of 10 Gyr. However, our measurement (§ 3.5.1) shows that the rate of energy released from and the mass contained in the hot gas of M104 are nearly two orders of magnitude lower than the empirical expectations. Given the prominent Fe L-shell features in the spectra, the fitted metal abundance should be largely weighted by the abundance of iron. Hence the fitted value is also lower than the empirical expectation, if the iron ejected by the SNe is uniformly distributed into the ISM. It is worth noting that metal abundance can easily be under-estimated in the spectral analysis of X-ray CCD data, especially with over-simplified models (e.g., in the case of NGC 1316 as demonstrated by Kim & Fabbiano 2003). Nevertheless, the lack of metals in M104 is evident and mostly tied to the small amount of X-ray emitting gas. Overall, there is a "missing stellar feedback" problem in M104.

In fact, this "missing stellar feedback" problem is often met in the so-called low L_X/L_B early-type galaxies (typically Sa spirals, S0, and low mass ellipticals), where

the X-ray luminosity, mass and metal content of the hot gas inferred from observations represent only a small fraction of what is expected from the stellar feedback (Irwin, Sarazin & Bregman 2002; O'Sullivan, Ponman & Collins 2003). These discrepancies are a clear indication for Type Ia SN-driven galactic winds (e.g., Irwin et al. 2002; Wang 2005). Globally, winds can continuously transport the bulk of stellar depositions into the IGM, leaving only a small fraction to be revealed within the optical extent of the host galaxy. Locally, our analysis (§ 3.5.1) for M104 indeed shows that the thermal structure of a wind is reasonably consistent with the observation, although more detailed considerations involving NEI processes in the gas are likely needed.

3.5.4 Feedback from the central AGN

Feedback from AGNs is a potential and sometimes favorable mechanism to affect the accretion of the IGM and the structure of hot gas. This is suggested to be the case in M104 (Pellegrini et al. 2003), even though its AGN has only a very sub-Eddington luminosity. AGN feedback, if present, would disturb the gas distribution in the circumnuclear region. For example, dips seen in the X-ray intensity distributions at certain azimuthal ranges (Figs. 3.6 and 3.7) might be the result of hot gas removal by the collimated ejecta from the AGN. However, no strong evidence of such collimated ejecta is seen in the radio continumm map of M104 (Bajaja et al. 1988). Furthermore, the inclusion of the AGN feedback would only increase the energy discrepancy discussed above. Therefore, although the possibility of AGN feedback can not be ruled out, we suggest that it plays little role in regulating the large-scale structure of hot gas in M104.

3.6 Summary

We have conducted a systematic analysis of the *XMM-Newton* and *Chandra* X-ray observations of the nearby massive Sa galaxy M104. The main results of our analysis are as follows:

- We have detected large-scale diffuse X-ray emission around M104 to an extent of ~ 20 kpc from the galactic center, which is substantially more extended than the stellar content;

- While at large scale the distribution of the diffuse X-ray emission tends to be smooth, intensity fluctuations are present in the inner region;

- Our spectral analysis of the diffuse emission reveals a gas temperature of $\sim$ 0.6-0.7 keV, with little spatial variation, while the measured gas density drops with increasing radius, in a way apparently different from the expected density distribution of either an isothermal gas in hydrostatic equilibrium or a galactic wind, assuming CIE emission;

- We have compared our measurements with the predictions of numerical simulations of galaxy formation and find that the observed 0.2-2 keV luminosity ($\sim 3.3 \times 10^{39}$ erg s^{-1}) is substantially lower than the predicted value;

- We have further compared the mass, energy, and metal contents of the hot gas with the expected inputs from the stellar feedback in M104. Much of the feedback is found to be missing, as is the case in some other X-ray faint early-type galaxies. A logical solution for this missing stellar feedback problem is the presence of a galactic wind, driven primarily by Type Ia SNe.

CHAPTER 4

CHANDRA DETECTION OF DIFFUSE HOT GAS IN AND AROUND THE M31 BULGE

4.1 Introduction

The bulge of a galaxy, though consisting of mainly old stars, is a mecca of high-energy activities. LMXBs, in the luminosity range of $\sim 10^{35} - 10^{38}$ ergs s^{-1}, are among the brightest X-ray sources observed in a galaxy like our own. At lower luminosities, typically $\sim 10^{30} - 10^{33}$ ergs s^{-1}, are numorous cataclysmic variables (CVs) and coronally active binaries (ABs) that can be individually detected normally only in the Solar neighborhood. Such stars are most likely responsible for the bulk of the unresolved 2-10 keV emission observed in the Galactic bulge/ridge (Revnivtsev et al. 2006), whereas lower energy X-rays from the same regions are subject to heavy interstellar absorption and hence difficult to detect. One thus needs external perspectives of nearby galaxies. Indeed, Revnivtsev et al. (2007) have shown that the unresolved emission from the low-mass bulge-dominated galaxy M32 over the entire 0.5-7 keV range is primarily stellar in origin.

The ISM in a galactic bulge is also expected to be extremely energetic, chiefly due to a concentration of Type Ia supernovae (SNe). The bulk of the mechanical energy release from such SNe is expected to be in shock-heated gas which can be naturally traced by its X-ray emission. However, the observed luminosity of the unresolved (source-removed) X-ray emission from a galactic bulge typically accounts for only a small fraction (a few %) of the expected SNe energy release. How the remaining energy is dissipated remains unknown. It may be propagated into the large-scale

63

halo of the host galaxy in a mechanical outflow or sound waves, for example. In any case, determining the fate of this "missing" stellar feedback energy is fundamentally important in our understanding of its role in galaxy evolution (e.g., Wang 2007). Here we present the first step of such a study.

We detect the truly diffuse soft X-ray emission from the bulge of M31 — the nearest spiral galaxy ($d \sim 780$ kpc; $1' \widehat{=} 0.23$ kpc) that is similar to our own Galaxy. The galaxy contains no AGN, so the non-nuclear X-ray emission can be studied even in the very central region. The M31 bulge has little cool gas and star formation, so the X-ray contribution from young stellar populations is minimal. The moderate inclination ($\sim 78°$) of the M31 disk and the relatively low Galactic foreground absorption ($N_H \sim 6.7 \times 10^{20}$ cm^{-2}) also allow us to detect extraplanar X-ray emission in the 0.5-2 keV range. Indeed, detections of diffuse soft X-ray emission have been claimed, based on spectral decompositions (Shirey et al. 2001; Takahashi et al. 2004). However, such a decomposition depends sensitively on rather arbitrary choices of spectral models for various components contributing to the spectrum, both diffuse and discrete. Our approach here is to spatially map out the diffuse X-ray emission (in addition to its energy dependence) and to study its relationship to other stellar and interstellar components of the M31 bulge.

4.2   Data preparation

Our X-ray study was based on 31 *Chandra* ACIS archival observations of M31 taken by 2005. The majority (21 out of 31) of these observations were taken with the ACIS-I array and aimed toward the M31 bulge with the aim-points located within $1'$ from the galactic center. To maximize the coverage and uniformity of the combined field, we utilized data only from the front-illuminated CCDs (the ACIS-I array and the S2 chips) of the 21 observations. For same reason, we also included I-chip data from four ACIS-S observations. These data together cover a field of $r \sim 18'$ around

the center of M31. Furthermore, for local sky background determination, we used six additional ACIS-I observations which were aimed toward an "off-field" $\sim 20'$ southwest to the center.

We reprocessed the data using CIAO (version 3.3), following the *Chandra* ACIS data analysis guide. We generated count and exposure maps for each observation in the 0.5-1, 1-2, 2-4 and 4-8 keV bands. Corresponding instrumental background maps were generated from the "stowed" data, after calibrating the 10-12 keV count rate with individual observations. The total effective exposure is ~ 95 ks in the central region and gradually drops to $\lesssim 20$ ks at radii $r \gtrsim 10'$.

Following a procedure detailed in Wang (2004), we performed source detection in the soft (0.5-2 keV), hard (2-8 keV) and broad (0.5-8 keV) bands. With a local false detection probability $P \leq 10^{-6}$, a total of 305 sources are detected in the field. To study the unresolved X-ray emission, we excluded each of the sources from maps of individual observations with circular regions enclosing $\sim 97\%$ of the source counts. The residual of this source removal contributes about 10% of the remaining unresolved X-ray emission in the field. The source-removed maps were then reprojected to generate combined images in the four bands. We further statistically corrected for the variation of the detection incompleteness across the field, to a common detection limit of 8×10^{34} ergs s^{-1} (0.5-8 keV). Because of the relatively flat luminosity function of the sources (mostly LMXBs; Voss & Gilfanov 2007), the correction (normalized according to the 2MASS K-band intensity; Fig. 4.1a; Jarrett et al. 2003) typically amounts to less than 6% of the unresolved emission. For the same reason, the residual contribution from LMXBs at lower luminosities is found to be negligible.

4.3   Analysis and results

Fig. 4.1a shows the 0.5-2 keV unresolved X-ray emission from a $30'$ by $30'$ region around the center of M31, compared with the near-IR K-band image. In the inner

bulge and along the major-axis of the disk, the X-ray emission shows morphological similarities with the K-band light, whereas at large radii the X-ray morphology appears substantially rounder and is elongated approximately along the minor-axis, in particular at the southeast side, indicating the presence of diffuse hot gas.

4.3.1 The collective stellar emission

To quantify the diffuse hot gas, we need to isolate the collective stellar contribution, which presumably spatially follows the K-band light distribution. Optimal for this purpose is to inspect regions along the major-axis, where the soft X-ray emission morphologically mimics the K-band light better than in regions further away from the major-axis (Fig. 4.1a). Fig. 4.2a shows the unresolved X-ray intensity profiles along the major-axis, together with the corresponding K-band intensity profile. Indeed, the K-band profile as a "model" fits the hard band profile (triangles in Fig. 4.2a) well with a normalization factor $N_K = 4.3 \pm 0.2 \times 10^{-5}$ cts s^{-1} arcmin^{-2}/(MJy sr^{-1}). Therefore, the hard band X-ray emission is fully consistent with an origin in the old stellar population.

The collective stellar emission should also contribute at lower energies. However, while the soft X-ray profile (diamonds in Fig. 4.2a) can match that of the K-band light reasonably well at major-axis radii $\gtrsim 8'$, there is a clear excess above the collective stellar contribution in the inner region. This soft excess in the bulge is another indication for the presence of hot gas, although its exact spatial distribution is yet to be determined. We include an exponential law to approximately account for the excess. The resultant fit is satisfactory (solid curve in Fig. 4.2a), with a fitted $N_K = (25.0 \pm 2.4) \times 10^{-5}$ cts s^{-1} arcmin^{-2}/(MJy sr^{-1}). The fit predicts that the stellar component contributes about 60% to the soft emission within a major-axis raidus of $\sim 8'$ and becomes dominant further beyond. The fit also reveals an interesting drop of the X-ray to K-band intensity ratio within the central $0.'5$ (more clearly indicated

in a radial intensity profile which is not shown here), with values still comparable to or greater than that at the large major-axis radii. The nature of this ratio drop is currrently being investigated, and we note that it has little effect on the result of the above procedure.
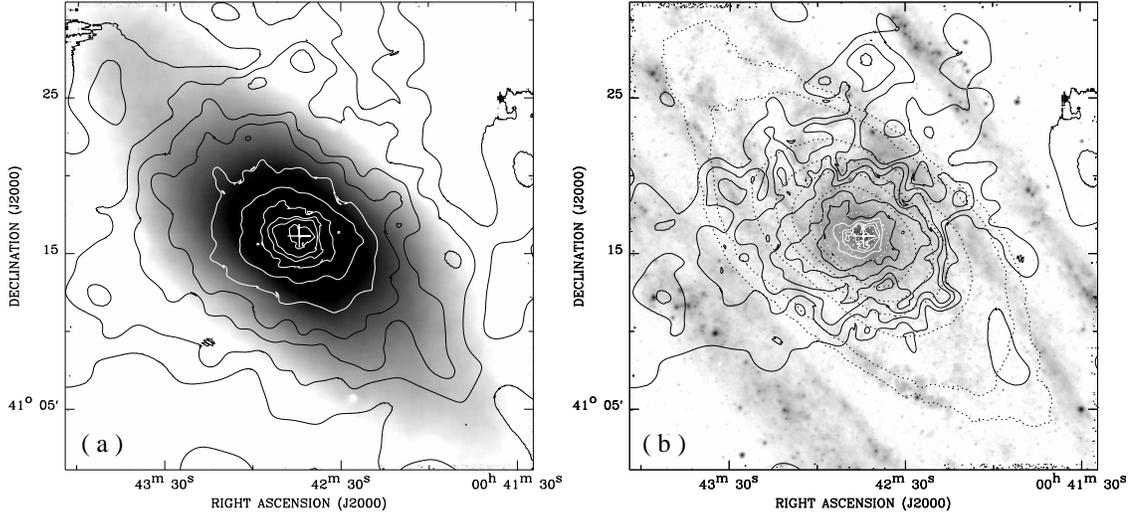
Figure 4.1 (a) Background-subtracted, exposure-corrected and smoothed intensity contours of the *Chandra* ACIS-I 0.5-2 keV unresolved emission overlaid on the 2MASS K-band image of M31. The contours are at 3, 6, 10, 16, 32, 64, 128, 196, 256 and 512 $\times 10^{-4}$ cts s^{-1} arcmin^{-2}. The galactic center is marked by a plus sign. (b) Contours of the diffuse (stellar contribution-subtracted) X-ray intensity (solid) and K-band light (dotted) overlaid on the *Spitzer* MIPS 24 μm image.

4.3.2 The diffuse X-ray emission

Fig. 4.1b shows an image of the truly diffuse emission after subtraction of the collective stellar contribution from the total unresolved X-ray emission of M31. The emission along the major-axis is confined within a projected distance of $\sim 8'$ (~ 1.8 kpc) from the galactic center to the southwest and is slightly more extended to the northeast. The overall morphology is elongated approximately along the minor-axis, with an extent of more than $15'$ (~ 3.5 kpc) on both sides with respect to the center; but the emission appears considerably fainter on the northwest side and somewhat interrupted by the presence of spiral arms. This asymmetry is further illustrated

in Fig. 4.2b, where diffuse X-ray intensity profiles along the minor-axis are shown separately in the 0.5-1 keV and 1-2 keV bands. The asymmetry can be naturally explained by the soft X-ray absorption of the galactic disk, as its near side is to the northwest. In particular, a major spiral arm and the star-forming ring, as traced by the peaks of the *Spitzer* MIPS 24 μm emission (Gordan et al. 2006), apparently cast deep X-ray shadows on the northwestern side. Estimated from the relative depth of these shadows, the equivalent X-ray-absorbing column densities are $\sim1.2\times10^{21}$ cm^{-2} and $\sim3.6\times10^{21}$ cm^{-2}, consistent with the hydrogen column densities of the spiral arm and the star-forming ring (Nieten et al. 2006). No similar shadow is apparent on the southeastern side, indicating that the emission on this side is mostly from the bulge region in front of the disk. Therefore, the diffuse emission seems to have an intrinsic (absorption-corrected) overall coherent morphology reminiscent of a bi-polar outflow from the bulge. The soft X-ray absorption by the disk suggests that the vertical extent of the X-ray-emitting gas from the galactic plane is at least 2.5 kpc.

We characterize the profiles (Fig. 4.2b) at distances of $-7' < z < 0'$ off the major-axis with an exponential law: $I(z) = I_g e^{-|z|/z_0}$, where I_g is the central intensity and z_0 is the projected scale-height. The best-fit z_0, being $2\!.\!5\pm0\!.\!1$ (~0.6 kpc), shows no statistically significant difference between the two bands, indicating that the hot gas in the bulge has little temperature variation. The hardness ratio, $I_{g,1-2keV}/I_{g,0.5-1keV}\sim0.25$, is consistent with a spectrum from an isothermal gas with a temperature of ~0.4 keV, subject to the Galactic foreground absorption. For comparison, the hardness ratio of the stellar emission is ~0.72; the scale-heigh of the K-band light is $\sim2\!.\!1$, if characterized by an exponential law as well. Therefore, the diffuse X-ray emission is both softer and more extended than the stellar contribution. At $|z| \gtrsim 7'$, however, the soft X-ray intensity distribution levels off (Fig. 4.2b). Part of this leveling may be related to emission associated with the galactic disk, partially compensating its X-ray absorption. The exact intensity level at such large distances,
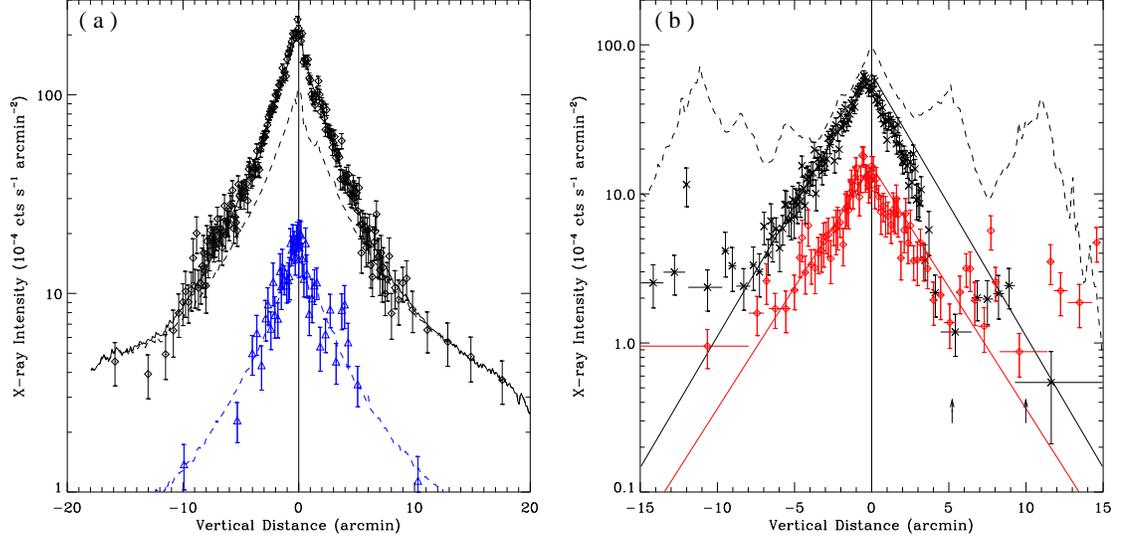
Figure 4.2 (a) 0.5-2 (*diamonds*) and 2-8 keV (*triangles*) keV intensity profiles of the unresolved X-ray emission along the major-axis. A position angle of 45° is adopted. The positive side is toward the southwest. The full width for averaging the intensity is 8′. Spatial binning is adaptively ajusted to achieve a signal-to-noise ratio better than 4, with a minimum step of 6″. The X-ray profiles are characterized by a normalized K-band intensity profile (dashed curves), and an additional exponential law for the soft band (solid curve). (b) 0.5-1 (*crosses*) and 1-2 keV (*diamonds*) intensity profiles of the diffuse emission along the minor-axis; the stellar contribution has been subtracted. The positive side is toward the northwest. The full width for averaging the intensity is 16′. The adaptive steps achieve a signal-to-noise ratio better than 3. The solid curves represent a fit with an exponential law. The corresponding 24 μm intensity profile is shown by the dashed curve. The arrows mark the positions of the shadows casted by a spiral arm and the star-forming ring.

however, depends on an accurate subtraction of the local sky background which has been estimated in the off-field and may be biased (§ 2). The sky coverage of the present ACIS observations is still too limited to accurately determine both the background and the large-scale distribution of the diffuse emission associated with the bulge. Assuming the above exponential fit and temperature estimate as well as an intrinsic symmetry with respect to the galactic plane, we infer a 0.5-2 keV luminosity of the diffuse emission as $\sim 2.2 \times 10^{38}$ ergs s^{-1}. The flat tail parts of the profiles give an additional $\sim 3 \times 10^{37}$ ergs s^{-1}.

4.4 Discussion

In § 3.4.1 we have estimated the stellar contribution to the total unresolved X-ray emission, which is a key step in isolating the truly diffuse emission. It is thus instructive to compare our result with independent measurements. Sazonov et al. (2006) measured the collective X-ray emissivity (per unit stellar mass) of the old stellar populations in the Solar neighborhood to be $9\pm3 \times 10^{27}$ ergs s^{-1} M$_\odot^{-1}$ in the 0.5-2 keV band and $3.1\pm0.8 \times 10^{27}$ ergs s^{-1} M$_\odot^{-1}$ in the 2-10 keV band. Revnivtsev et al. (2006) showed that the Galactic ridge X-ray emission closely follows the near-IR light that traces the Galactic stellar mass distribution, and that the X-ray to near-IR intensity ratio is consistent with the collective X-ray emissivity of old stellar populations inferred from the Solar neighborhood. Revnivtsev et al. (2007) further found that the 0.5-7 keV unresolved X-ray emission and K-band stellar light in M32 have consistent spatial distributions, but they did not explicitly give fitted parameters of the spectral model, which would allow for an immediate comparison with the M31 values.

We have thus re-extracted the unresolved X-ray spectrum of M32 from two *Chandra* ACIS-S observations (Obs.ID. 2017 and 5690) with a total exposure of 160 ks. The spectrum can be adequately fitted by a model consisting of a power-law component (with a photon index of $1.86^{+0.26}_{-0.21}$) and a thermal plasma component (temperature of $0.45^{+0.15}_{-0.10}$ keV), with the Galactic foreground absorption. The collective emissivity is $5.8\pm1.1(5.6\pm1.0) \times 10^{27}$ ergs s^{-1} M$_\odot^{-1}$ in the 0.5-2 (2-10) keV band, consistent with the values reported by Revnivtsev et al. (2007). The spectral model-predicted ACIS-I count rate is $\sim$17.1 (3.9) $\times10^{-5}$ cts s^{-1} arcmin^{-2}/(MJy sr^{-1}) in the 0.5-2 (2-8) keV band. The hard band value agrees well with the measurement for M31 ($4.3\pm0.2\times10^{-5}$), accounting for the residual photons spilling outside the source-removal regions ($\sim$ 10%; § 4.2). The soft band stellar emissivity of M31 (residual LMXB contribution excluded) is a factor of 1.4 ± 0.3 higher than the M32 value, but is consistent with that inferred from the Solar neighborhood. This discrepancy is not

totally unexpected, considering various statistical errors and hiden systematic uncertainties (e.g., in the mass-to-light ratio and in the spatial and spectral modeling). We note that adopting the M32 stellar emissivity to remove the stellar contribution in M31 would enhance the hot gas contribution in and around the M31 bulge, but would not qualitatively alter the picture of the diffuse emission presented in § 4.3.2 and below.

The characterization of the diffuse hot gas sheds important insights into the energy balance in the M31 bulge. The estimated luminosity of the hot gas $(2.5 \times 10^{38}$ ergs s$^{-1})$ is only about 0.6% of the expected SNe mechanical energy input, $\sim 4 \times 10^{40}$ ergs s^{-1}. As mentioned in § 4.1, this indicates that the input energy may be removed primarily in an outflow. Dynamically, such an outflow tends to find its way along steeper pressure gradient against the gravity of the galaxy, consistent with the observed bipolar morphology of the diffuse X-ray emission. If the gas were quasi-static, one would expect its distribution to follow that of the gravitational potential, i.e., more extended along the major-axis. However, the gas may not be hot enough to ultimately escape from the deep gravitational potential of M31; it is also not clear how the outflow interacts with the large-scale halo of M31 and how the mechanical energy is dissipated. Similar considerations also challenge the studies of X-ray-faint elliptical galaxies (e.g., David et al. 2006). Ongoing numerical simulations would help to understand the nature of the hot gas and its role in the evolution of these systems.

Our unambiguous detection of the diffuse hot gas in and around the M31 bulge also helps to understand the soft X-ray enhancement observed toward the inner region of our Galaxy. The temperature of the hot gas associated with the M31 bulge, 0.4 keV, is similar to that with the Galactic bulge, as estimated from the ROSAT all-sky survey (Snowden et al. 1997). Based on a hydrostatic model of the Galactic bulge X-ray emission developed by Wang (1997), Almy et al. (2000) further inferred a total 0.5-2 keV luminosity of $\sim 8 \times 10^{38}$ ergs s^{-1}, about four times greater

than our estimated M31 bulge luminosity. The relatively high luminosity of the Galactic bulge manifests in the large extent of the soft X-ray enhancement from the Galactic bulge. At Galactic latitudes $b \sim -15°$ ($\sim$2 kpc from the plane), for example, where both the confusion with the foreground emission features and the interstellar absorption are relatively small, the intensity has an averaged value of $\sim$6(4)$\times 10^{-4}$ ROSAT PSPC cts s^{-1} arcmin^{-2} in the 0.75 (1.5) keV band (Snowden et al. 1997). Had this emission been detected from M31 by the *Chandra* ACIS-I, it would be measured with an intensity of $\sim$10(3)$\times 10^{-4}$ cts s^{-1} arcmin^{-2} in the 0.5-1 (1-2) keV band, about 2-4 times higher than the observed M31 values represented by the tails (Fig. 4.2b). The intensity drops slowly and even shows local enhancements at high latitudes ($b \gtrsim -30°$; Snowden et al. 1997). Within $|b| \lesssim 10°$, the interstellar absorption is severe, little can be inferred reliably about the properties of the hot gas. It is in this corresponding region in the M31 bulge ($|z| \lesssim 6'$) that the diffuse soft X-ray intensity shows the steepest increase (by about one order of magnitude) toward the galactic center. Such a mid-plane concentration of diffuse soft X-ray emission may also be present instrinsically in our Galactic bulge. Clearly, a more careful comparison and modeling of the X-ray data sets are needed in order to understand the similarity and difference in the hot gas characteristics and their relationship to other galactic properties (e.g., the effect of recent active star formation in the Galactic center).

CHAPTER 5

M31* AND ITS CIRCUMNUCLEAR ENVIRONMENT

5.1 Introduction

Galactic circumnuclear environments, in which stars and interstellar medium (ISM) are present in a dense state, are of vast astrophysical interest. The circumnuclear ISM, generally thought to be composed of externally acquired material and local stellar ejecta, is the neccesary fuel for the SMBH to become an active galactic nucleus (AGN). Theoretically, how the fuel is transported to the SMBH is not fully understood (e.g., a recent review by Wada 2004). Observationally, direct links between nuclear activities and the ISM properties remain to be uncovered. Timescales of both dynamical and thermal processes are relatively short in the circumnuclear regions; thus a passive accumulation of the multi-phase (e.g., neutral and ionized) ISM there would inevitably lead to an interaction among its various components, and possibly to enhanced nuclear and/or star-forming activities (e.g., Ho, Filippenko & Sargent 1997; Sarzi et al. 2007). That different phases of the ISM often co-exist in galactic circumnuclear regions, some showing organized morphologies (e.g., van Dokkum & Franx 1995; Macchetto et al. 1996; Knapen et al. 2005), is an indication of certain mechanisms regulating the dynamics and energetics of the ISM, which remains to be understood. Furthermore, the global ISM evolution, one of the fundamental issues in galaxy evolution, can not be fully assessed without understanding its role in the circumnuclear regions.

Owing to its proximity ($d \sim$780 kpc; $1'\hat{=}0.23$ kpc), the Andromeda Galaxy (M31) provides an ideal testbed for studing a galactic circumnuclear environment. Indeed,

the inner few hundred parsecs of M31 have received vast observational attention, from radio to X-ray, tracing all phases of the ISM and various types of stars in the region. As we will further discuss in the later sections, it is clear that the SMBH of M31 (i.e., M31*) is currently inactive and thus brings minimal disturbance to its environment, in which there is also little indication for recent star formation. Without the confusion from such activities, this environment offers a unique "quiescent" close-up of possible relationships among the various interstellar and stellar components as well as the nucleus. In this work we aim to probe and to understand such relationships.

Studing the ISM against a high stellar radiation background is by no means straightforward at any wavelength. In particular, it is practically difficult to isolate the X-ray emission of truly diffuse hot gas from the collective emission of individually unresolved stars. In a recent study of the M31 bulge with *Chandra* observations (Li & Wang 2007; hereafter LW07), we have successfully accounted for the collective X-ray emissivity of faint, unresolved stars (see also Revnivtsev et al. 2007; Bogdán & Gilfanov 2008) according to the near-infrared (NIR) K-band light distribution, and thus revealed the presence of diffuse hot gas on kpc-scales (LW07; Fig. 5.1a). This procedure in turn allows us to advance the high-resolution study of hot gas in the circumnuclear regions.

The rich observational knowledge in the literature on M31* and its surrounding matter (except for the hot gas yet to be studied) deserves a selected summary in § 5.2, which in turn serves as a necessary guide for subsequent analyses. The preparation of multiwavelength data used in this work is brifely described in § 5.3. We present our analyses in § 5.4 and discuss the results in § 5.5. Important implications of the study are summarized in § 5.6.

5.2 Observational knowledge on M31* and its environment

- **Nucleus**

At optical wavelenths M31 hosts the well known double nuclei (so-called P1 and P2; Lauer et al. 1993) peaking at an angular separation of about half-arcsec from each other, which are interpreted to be an eccentric disk of typically K-type stars with a total mass of $\sim 2 \times 10^7$ M$_\odot$ (Tremaine 1995). P2 is fainter than P1 in V- and B-bands but brighter in U-band and in UV, consistent with an addition of a 200 Myr old starburst embedded in P2 (called a third nucleus, P3; Bender et al. 2005). The SMBH is embedded in P2/P3, with an inferred dynamical mass of $\sim 1.4 \times 10^8$ M$_\odot$ (Bender et al. 2005).

Crane, Dickel & Cowan (1992) reported detection of M31* from VLA 3.6 cm observations, giving a flux density of 28 μJy. Basing on a 50 ks *Chandra*/HRC observation, Garcia et al. (2005; hereafter G05) claimed a 2.5 σ detection of M31* with a 0.3-7 keV intrinsic luminosity of $\sim 9 \times 10^{35}$ ergs s^{-1}.

- **Stars**

  The photometry in NIR (Beaton et al. 2007) and optical (Walterbos & Kennicutt 1998) bands shows little color gradient in the inner bulge. The colors are typical of an old, metal-rich stellar population, equivalent to type G5 III or K0 V. The Mg$_2$ index of 0.324 measured from the central $\sim 30''$ (Burstein et al. 1988) indicates a metallicity of [Fe/H]$\sim$0.3 (Buzzoni, Gariboldi & Mantegazza 1992). For reference, the K-band luminosity within the central $1'$ ($2'$) is 4.7 (11)$\times 10^9$ L$_{\odot, K}$, which, according to the color-dependent (here a $B - V$ color of 0.95 is adopted) mass-to-light ratio of Bell & de Jong (2001), corresponds to a stellar mass of 4.0 (9.3)$\times 10^9$ M$_\odot$.

  Using N-body simulations, Athanassoula & Beaton (2006) showed that a classical bulge plus a bar-like structure is able to reproduce the observed NIR light distribution. This strongly argues the presence of a stellar bar in M31, which is otherwise difficult to be recognized due to its high inclination.

There is little evidence for any recent massive star formation in the circumnuclear regions. No massive (i.e., O and B-types) stars have been detected (King et al. 1992; Brown et al. 1998); the far- to near-ultraviolet ($FUV - NUV$) color in the inner bulge suggests a stellar age over 300 Myr (Thilker et al. 2005); while a small amount of ionized gas is indeed present, it shows optical line intensity ratios atypical of conventional HII regions (Rubin & Ford; del Burgo, Mediavilla & Arribas 2000; see below).

- **Atomic gas**

  So far there is no reported detection of atomic hydrogen in the central 500 pc; an upper lmit of HI mass is set to be 10^6 M$_\odot$ (Brinks 1984).

- **Warm ionized gas**

  The existence of ionized gas has long been known through detection of [O II], [O III], Hα, [N II] and [S II] emission lines in the spectra of the inner bulge (Munch 1960; Rubin & Ford 1971). Later narrow-band imaging observations (Jacoby, Ford & Ciardullo 1985; Ciardullo et al. 1988; Devereux et al. 1994) further revealed that the gas is apparently located in a thin plane, showing filamental and spiral-like patterns, across the central few arcmins (so-called a *nuclear spiral*; Fig. 5.1b). The electron density of the ionized gas, inferred from the intensity ratio of [S II] lines, is $\sim$10^2-10^4 cm^{-3} within the central arcmin, generally decreasing outward from the center (Ciardullo et al. 1988). The gas is estimated to have a mass of $\sim$10^3 M$_\odot$, an Hα+[N II] luminosity of a few 10^{39} ergs s^{-1}, and a very low volume filling factor consistent with its filamental morphology (Jacoby et al. 1985). The relatively high intensity ratio of [N II]/Hα, ranging from $\sim$1.3-3 in different regions (Rubin & Ford 1971; Ciardullo et al. 1988), is typical of values found in the bulge/halo of early-type galaxies (e.g., Macchetto et al. 1996) rather than in conventional HII regions

(with typically [N II]/Hα $\sim$0.5). Kinematics of the gas is rather complex. A major component of the velocity field apparently comes from circular rotation, whereas the residuals indicate both radial and vertical motions (Rubin & Ford 1971).

That the stellar disk of M31 is probably barred offers a natural formation mechanism for the nuclear spiral: an inflow of gas from the outer disk driven by bar-induced gravitational purterbations to form organized patterns (e.g., Englmaier & Shlosman 2000; Maciejewski 2004). Indeed, by modelling the gas dynamics in a bar-induced potential Stark & Binney (1994) obtained a satisfactory fit to the observed position-velocity diagram of the ionized and neutral gas in the central $\sim$2$'$. Another possible driver of gas is a recent head-on collision between M31 and its companion galaxy, favorably M32 (Block et al. 2006). Although details remain to be studied, it seems certain that an asymmetric gravitational potential is responsible for the formation and maintenance of the nuclear spiral in M31 and similar gaseous structures found in the inner regions of disk galaxies (e.g., Regan & Mulchaey 1999). The ionizing source responsible for the observed optical lines, however, is rather uncertain, especially in view of the lack of massive stars in the region. We discuss possible ionizing sources in § 5.5.

- **Molecular gas and dust**

Detection of CO closest to the galactic center ($\sim$1$\rlap{.}'$3 away) points to a prominent dust complex, D395A/393/384, with an estimated molecular gas mass of 1.5×10^4 M$_\odot$ (Melchior et al. 2000). This $\sim$100 pc-wide feature is also seen in mid- and far-infrared (MIR/FIR) emission (see § 5.4.3).

Spitzer observations now provide the highest-resolution MIR/FIR view toward the circumnuclear regions. We show below (§ 5.4.3) that these observations

reveal the presence of interstellar dust and its remarkable association with the nuclear spiral.

- **Magnetic field and high energy particles**

  Under $10''$-$30''$ resolution the radio continuum emission shows filamental patterns apparently associated with the Hα emission, i.e., the nuclear spiral (Walterbos & Grave 1985; Hoernes, Beck & Berkhuijsen 1998). The average power-law spectral index ($S_\nu \propto \nu^\alpha$) of $\sim$-0.75 throughout the 2.8-73.5 cm range indicates that the bulk emission is non-thermal (Walterbos & Grave 1985). Hoernes et al. (1998) reported that the polarized emission is concentrated on the filaments, and that the regular magnetic field appears to be oriented along the filaments. Assuming energy equipartition and a volume filling factor $f \sim 1$, Hjellming & Smarr (1982) estimated an energy density of $\sim$0.5 eV cm^{-3} for the energetic particles within the central $30''$. In regard to the likelihood that a substantial fraction of the radio emission arises from the nuclear spiral, however, the assumption of $f \sim 1$ is questionable, let alone that for the energy equipartition.

5.3   Data preparation

This work involves a variety of high-resolution data from IR to X-ray. Procedures of combining the archival *Chandra*/ACIS-I observations and spatially isolating the diffuse X-ray emission in the M31 bulge have been described in LW07. The same X-ray data set is used in this work to study the circumnuclear regions, for which a total effective exposure of $\sim$90 ks is achieved. In order to maximize the counting statistics to constrain the X-ray emission of M31*, we added to the data set a 38 ks ACIS-S observation (Obs.ID 1575; PI: S. Murray). This observation unfortunately appears to be contaminated by a low-level, long-duration flare of cosmic-rays, hence we do not include it for the analysis of the diffuse emission, which requires a more stringent

filtering of flares. In spectral analysis (§ 5.4.2), spectra extracted from individual observations were combined into a single spectrum. The considered energy range is restricted to 0.5-4 keV to miminize contamination by residual flares. A "stowed background" was subtracted to remove the quiescent instrumental signals. Although we do not have a precise knowledge of the sky background (LW07), it has a negligible contribution in the analyzed spectra.

It is known that a bright X-ray source is located at $\sim$0″.5 from the position of M31* (G05; see § 5.4.1). Thus it is a challenge for the ACIS image, with its 0″.49 pixel size and typical PSF FWHM of 0″.6-0″.7 near the optical axis, to isolate the emission from M31*. Therefore we have followed the "sub-pixel event repositioning" technique (Tsunemi et al. 2001; Li et al. 2003) to take advantage of sub-pixel information from the dithering of the ACIS observations. The resultant "super-resolution" ACIS image has a PSF FWHM of $\sim$0″.5.

To trace the warm ionized gas we rely on the Hα+[N II] image of Devereux et al. (1994) with a $\sim$2″ resolution. For simplicity, in the following we refer to this image as the Hα emission unless otherwise the [N II] component is specified. We also obtained the *Spitzer*/IRAC (Program ID 99; PI: M. Rich), *Spitzer*/MIPS (Program ID 3400; PI: G. Rieke), 2MASS K-band (Jarrett et al. 2003), HST/ACS F330W (Propos.ID 10571; PI: T. Lauer) and GALEX NUV/FUV (Gil de Paz et al. 2007) images of M31 from public archives, in order to provide a multiwavelength, co-spatial view of the various stellar and interstellar components. In particular, the *Spitzer* MIR/FIR images offer unprecedented information on how the interstellar dust, and thus the cold neutral gas to some extent, is distributed across the circumnuclear regions. We note that, while the bulk of the FIR emission presumably arises from interstellar dust, a substantial fraction of the MIR emission from the inner bulge comes from stellar objects, i.e., emission of the circumstellar envelopes around asymptotic giant branch (AGB) stars (e.g., Bressan, Granato & Silva 1998), the spatial distribution of which

79

closely follows the bulge starlight (e.g., Barmby et al. 2006; Gordon et al. 2006). Therefore we have subtracted a normalized K-band image from the IRAC 8 μm and MIPS 24 μm images respectively to remove the stellar contribution. To do so, we first constructed the radial ($8 \ \mu m - K$) and ($24 \ \mu m - K$) color profiles from consecutive annuli. Within each annulus the intensity of each band was chosen to be the median (instead of azimuthally-averaged) value to minimize fluctuation introduced by the interstellar component. Both profiles show little ($\lesssim 10\%$) radial variation within the central $\sim 3'$ and thus represent the ($8 \ \mu m - K$) and ($24 \ \mu m - K$) flux ratios of the stellar component, which were then adopted as normalization factors for the K-band image. The $\lesssim 10\%$ uncertainty indroduced by the subtraction is expected to have little effect on the interpretation of subsequent analysis. Hereafter the 8 and 24 μm emission refer to the interstellar component only.

To further extend our multiwavelength view and to probe the conceiveable presence of gas with temperatures of 10^5-10^6 K, we utilized FUSE spectroscopic observations toward the center of M31, which is part of a program (Program ID C128; PI T. Brown) aimed at understanding the stellar populations in the cores of elliptical galaxies. Four exposures were taken covering the central $30''$ by $30''$ and a total useful exposure time of 49 ks. The reduction and calibration of the FUSE spectra were described in detail by Wakker et al. (2003) and Wakker (2006).

5.4 Analysis and results

Our mining of the multiwavelength data is presented in this section. First we attempt to constrain the amount of X-ray emission from M31*, with a much improved counting statistics compared to that achieved by G05. Next we study the physical properties of the diffuse hot gas, as we shall show below, filling the bulk of the circumnuclear volume. This volume-filling gas may naturally play a crucial role in
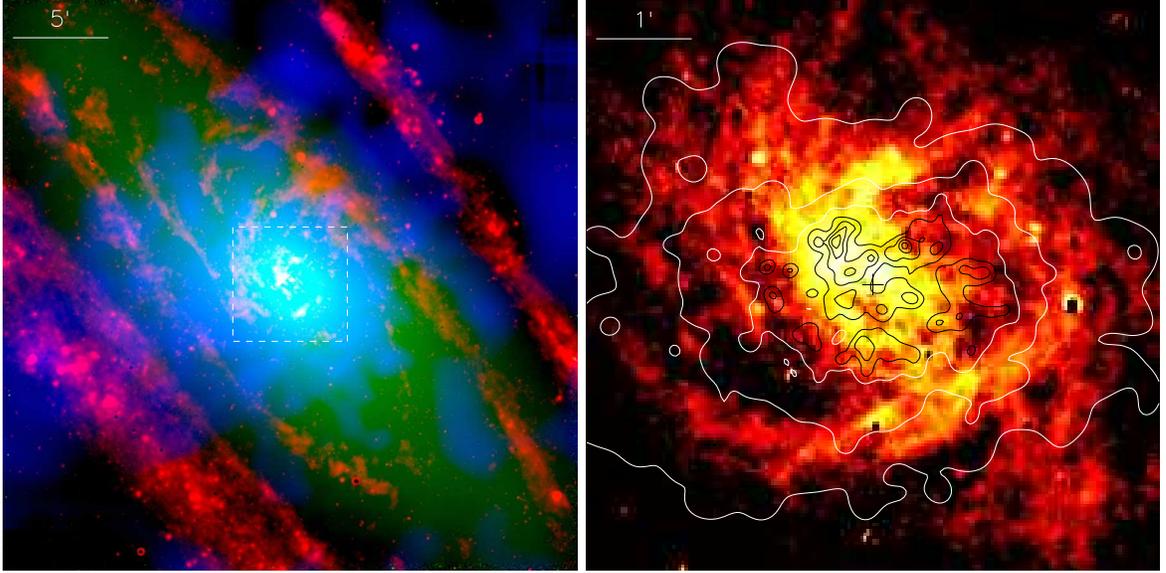
Figure 5.1 (a) Tri-color image of the central 30′ by 30′ (6.8 kpc by 6.8 kpc) of M31. *Red*: *Spitzer*/MIPS 24 μm emission; *Green*: 2MASS K-band emission; *Blue*: *Chandra*/ACIS 0.5-2 keV emission of diffuse hot gas (LW07). The dashed box outlines the central 6′ by 6′, a region further shown in (b) and Fig 5.5. (b) Smoothed intensity contours of the 0.5-2 keV diffuse emission overlaid on the Hα emission. The contours are at 5, 10, 19, 27, 35, 45, and 55 $\times 10^{-3}$ cts s^{-1} arcmin^{-2}. The plus sign marks the M31 center.

regulating the mass and energy flows in the region. From the multiwavelength view we then seek clues about physical relations among the various ISM components.

5.4.1 X-rays from M31*

Fig. 5.2 shows the distribution of 0.5-8 keV ACIS counts detected from the central $3'' \times 3''$ region, along with an HST/ACS F330W image showing the double nuclei P1 and P2. Dominating the X-ray emission are the two known bright sources with luminosities of $\sim 10^{37}$ ergs s^{-1}: a super-soft source (SSS; partly shown in Fig. 5.2) is located at $\sim 2''$ south to the nuclei; the other source (named N1 by G05) is positionally coincident with P1, the presence of which severely hampers the isolation of X-ray emission from M31*.

We assume that the X-ray source N1 is indeed embedded in P1. By fixing the angular displacement between N1 and the yet unresolved M31* as that between the

two optical nuclei, i.e., $0\!\!''\!5$ (Lauer et al. 1998, Fig. 8 therein), we perform a 2-d fit to the ACIS image by adopting a model consisting of three delta functions convolved with the local PSF, respectively respresenting SSS, N1 and M31*, and a constant representing the background "diffuse" emission. The local PSF is mimiced by stacking seven bright sources detected within $30''$. The centroids of SSS and N1, the normalization of all three sources and the background constant are determined by the fit, while the relative location of N1 and M31* is fixed as assumed. The best-fit is achieved with a normalization of 210 ± 50 (1 σ) cts for M31*. Corrected for the difference of effective area between ACIS-S3 and ACIS-I, the best-fit infers a 0.5-8 keV ACIS-I count rate of 1.4×10^{-3} cts s^{-1}, corresponding to a 0.3-7 keV intrinsic luminosity of 1.2×10^{36} ergs s^{-1} (assuming an absorbed power-law spectrum with $N_{\rm H}\sim7\times10^{20}$ cm^{-2}, the Galactic foreground absorption column, and a photon-index of 1.7), which is consistent with the 2.5 σ detection of 9×10^{35} ergs s^{-1} for M31* reported by G05 (based on $\sim$10 *Chandra*/HRC counts). We have also tried to probe flux variation by examing the detected count rate of the $0\!\!''\!25$ by $0\!\!''\!25$ square enclosing M31* from individual observations of typically 5 ks long. We find no statistically significant variation over a factor of 2 from observation to observation as well as from within the 38 ks ACIS-S observation.

Our constraint for the X-ray emission of M31* relys on the assumption that the bright X-ray source N1 is embedded in P1 instead of being an interloper. In galactic bulges the most likely interlopers are low-mass X-ray binaries (LMXBs). Gilfanov (2004) derived an empirical relation between the number of LMXBs with luminosites over 10^{37} ergs s^{-1} and the stellar mass of the host galaxies, being $N_{\rm LMXB}\approx$ 14 sources per 10^{10} M$_\odot$. Along the line of sight through the central arcsec, the observed K-band light infers a stellar mass of few 10^{7} M$_\odot$. Accordingly, the expected number of LMXBs along this line is $\lesssim$0.05. Hence the chance that we have detected N1 as an interloper is small. Moreover, stellar mass BH and neutron stars (NS)
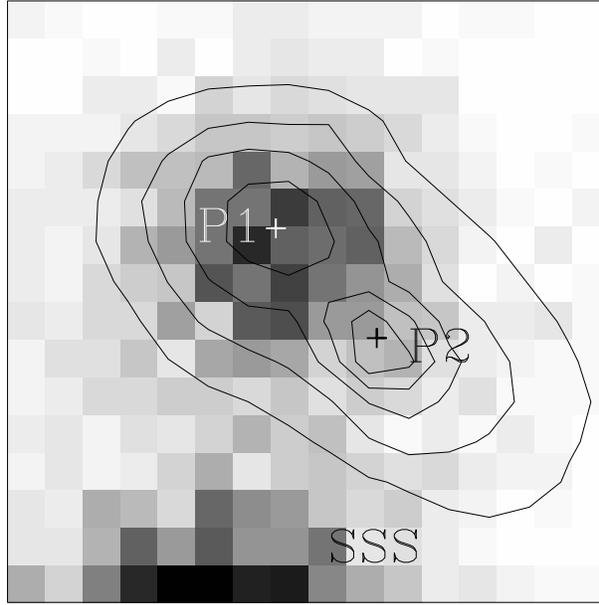
Figure 5.2 A super-resolution 0.5-8 keV ACIS counts image (§ 5.3) of 0″125 pixels, with the HST/ACS F330W intensity contours showing the double nuclei P1 and P2. The greyscale linearly ranges from 0 to 40 cts/pixel. The '+' signs mark the fitted centroids of P1 and P2. The displacement between P1 and P2 in X-ray is assumed to be same as in optical. Part of the SSS is also shown at the bottom of the field.

formed in the central cusp of the bulge are predicted to sink into the close vicinity (few parsecs) of the SMBH, due to dynamical friction on less massive background stars (Morris 1993). Such migrators thus have the chance to compete with the SMBH on the consumption of surrounding gas to become bright X-ray sources. Nayakshin & Sunyaev (2007) modeled such a process and found that the collective X-ray luminosity of the migrated compact objects can be higher than that of the SMBH up to two orders of magnitude, dependent on the mass of the common accretion disk. This scenario lends further support to the above procedure of pinning N1 on the position of P1, in a sense that N1 is the appearance of one or more accreting stellar mass BHs, being about ten times brighter than M31*. In regard of the common origin of P1 and P2 (i.e., an eccentric stellar disk), it is possible that the X-ray signals detected from the position of P2, which we have considered as originated from M31*, also arise from

stellar mass BHs. The marginal flux variation detected does not offer much help in distinguishing between a stellar mass BH origin and a SMBH origin. It is worth to note that, at the position of P1, which is the apocenter of the eccentric orbits, BHs (and stars) have small velocities and hence a greater chance to capture the surrounding gas at large accretion rates. The situation is likely opposite at the position of P2. In conclusion, the assumed source positions are physically plausible.

5.4.2 Diffuse hot gas

Fig. 5.1a shows the large-scale 0.5-2 keV diffuse X-ray emission in the M31 bulge. The emission, showing an elongated morphology along the minor-axis and shadows cast by the outermost spiral arm and the prominent star-forming ring (e.g., Gordon et al. 2006) on the the near (northwestern) side of the tilted disk, has led LW07 to suggest that the hot gas is in a form of bi-polar outflow. Fig. 5.1b shows this emission in the circumnuclear regions, along with the Hα emission tracing the nuclear spiral. As is the case on large-scales, the X-ray emission appears i) elongated approximately along the minor-axis, and ii) fainter at the northwestern side beyond the central arcmin, presumably due to absorption by some cold ISM located in the foreground. These suggest that the bi-polar outflow of hot gas is launched in the very inner bulge.

A more quantitative view of the diffuse X-ray emission is shown in Fig. 5.3 for the 0.5-2 keV intensity profiles along the minor (NW) and major (SW) axes and the radius. The intensity i) has a slightly steeper drop along the major-axis than along the minor-axis, and ii) is lower at the northwestern side along the minor-axis; these are fully consistent with the morphology shown in Fig. 5.1b. The major-axis profile has a "cap" shape in the centeral arcmin, where the intensity is more than two times higher than that of the regions immediately beyond. In accordance, the radial profile exhibits a flattening towards the center (Fig. 5.3c). These apparently result from the clumpy X-ray emission positionally coincident with the nuclear spiral in the central
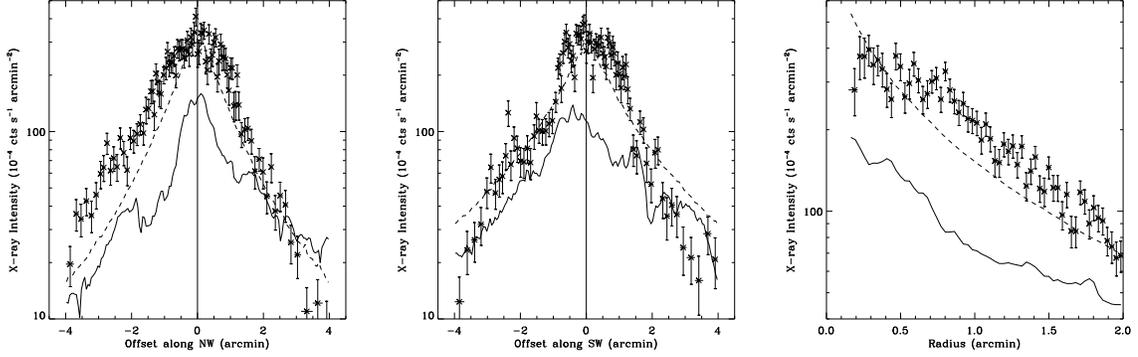
Figure 5.3 0.5-2 keV diffuse X-ray intensity profiles along the minor-axis (a), the major-axis (b) and the radius (c). The vertical profiles are averaged within slices of 2′ in width. A position angle of 40° is adopted. In each pannel, the dash curve shows the corresponding K-band intensity profile with a normalization representing the *already subtracted* contribution of unresolved X-ray sources, whereas the solid curve is the corresponding Hα intensity profile with an arbitrary normalization.

arcmin (Fig. 5.1b), indicating a relation between the two ISM components, albeit overall the X-ray intensity profile shows no clear correlation with the Hα intensity profile (solid curve in Fig. 5.3b). Compared to the steep decline of the K-band light (dashed curve in Fig. 5.3b), the "cap" also indicates a source of hot gas in addition to the stellar ejecta. A more detailed comparison of the multiwavelength emission will be given in § 5.4.3.

To quantify the hot gas properties, we extract a representative spectrum of the total unresolved X-ray emission (i.e., from both the gas and unresolved stellar objects) from the central 1′ (Fig. 5.4). The unresolved stellar objects, with individual luminosities below 10^{35} ergs s^{-1}, are predominantly cataclysmic variables and coronally active binaries (CVs and ABs; Sazonov et al. 2006), the average spectrum of which unfortunately can not be determined in the M31 bulge due to the presence of hot gas. Instead, we rely on such a spectral information as derived from the drawf elliptical galaxy, M32, which essentially lacks diffuse gas (Revnivtsev et al. 2007). We find that, in agreement with Revnivtsev et al. (2007), the spectrum of the unresolved X-ray emission from M32 can be characterized by a combination of two thermal plasma
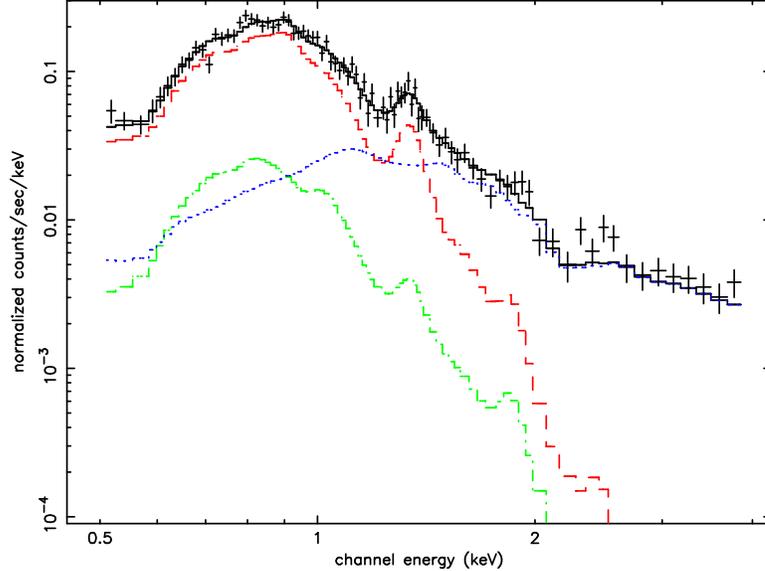
Figure 5.4 Spectrum of the central 1′, fitted by a three-component model: VMEKAL (gas; *red curve*) + MEKAL (ABs; *green curve*) + MEKAL (CVs; *blue curve*). See text for details.

emission components (MEKAL in XSPEC), with temperatures of ∼0.4 and ∼4.6 keV and a solar abundance. The low- and high-temperature components are dominated by the emission of ABs and CVs, respectively. We adopt these two components to account for the stellar contribution in the M31 spectrum, fixing the temperatures and abundance and having the normalizations scaled according to the underlying K-band light. As shown in Fig. 5.4, the adopted model well accounts for the observed spectrum at energies above ∼1.5 keV. At lower energies, there is indication that the stellar emissivity inferred for the M31 bulge is ∼1.5 times higher than that for M32 (LW07). We note that neglecting this difference has little effect on the subsequent fit results as the gas component dominates the 0.5-1.5 keV emission.

We then introduce a third thermal component (VMEKAL in XSPEC) to charac-terize the emission of hot gas, allowing the abundance, if other than solar as required by the fit, to be different among heavy elements. This component is subject to pos-sible absorption by the cold ISM in the circumnuclear regions (see § 5.4.3). The fit is initiated with the abundance of all elements fixed at solar, giving a fitted temper-

ature of ~0.3 keV. The fit is poor, however, in particular not able to account for a prominent line feature present at ~1.33 keV, most likely due to Mg XI Kα, given a gas temperature of ~0.3 keV. Therefore, we let the abundance of Mg to be determined in a fit. The abundance of Fe is also allowed to be free in the fit to account for the Fe L-shell lines dominating energies of ~0.8-1 keV. The resulant fit, with $Z_{\mathrm{Mg}} \sim 2$ and $Z_{\mathrm{Fe}} \sim 1$, still shows considerable discrepancies at energies below 0.7 keV, where lines of O VII and O VIII dominate. Finally an acceptable fit is achieved with a fitted $Z_{\mathrm{O}} \sim 0.4$. The various fit results are summerized in Table 5.1. We infer from the best-fit an electron density of 0.08 cm^{-3} and a 0.5-8 keV unabsorbed flux of 1.0×10^{-12} ergs cm^{-2} s^{-1} for the hot gas.

The clumpiness of the circumnuclear X-ray emission (Fig. 5.1b) implies that the hot gas is inhomogeneous, in particular, the gas could have more than one temperature. In this regard, we fit the spectrum with the CEVMAL model in XSPEC. The model assumes a continuous distribution of emission measure (EM) such that $S_\nu = \int_{T_{\min}}^{T_{\max}} N\Lambda_\nu(T, Z)(T/T_{\max})^\alpha dT/T$ (Singh, White & Drake 1996), where S_ν is the intrinsic spectrum, Λ_ν the volume emissivity provided by the MEKAL model, and N the normalization. The maximum temperature $T_{\max}$ is fixed at 3.6 keV, the reason of which would become clear below (see § 5.5.2). Due to the degeneracy between $T_{\max}$ and α, the exact choice of $T_{\max}$ is not crucial for the fit and its implications. The minimum temperature $T_{\min}$ is effectively 0.08 keV in the implement of MEKAL. While the fit is not as satisfatory as the single-temperature fit, the resultant value of α, being negative (~-2.7), implies that high-temperature gas, if existed, has only a minor contribution to the total emission. If we further assume that the density and fractional volume of gas are power-law functions of temperature: $n \propto T^{\alpha_n}$, $dV/dT \propto T^{\alpha_V}$, from $S_\nu \equiv \int \Lambda_\nu(T, Z)n^2 dV$ we have $\alpha = 2\alpha_n + \alpha_V + 1$. In the case of thermal pressure balance, $\alpha_n = -1$ and $\alpha_V = -1.7$, it can be shown that the volume-weighted temperature is ~0.4 keV. This value is close to the single temperature of 0.3 keV de-

Table 5.1. Fits to the spectrum of diffuse X-ray emission from the central arcmin

Model	$N_H{}^a$ 10^{20} cm^{-2}	T keV	α	$Z_O{}^b$	$Z_{Fe}{}^b$	$Z_{Mg}{}^b$	EM cm^{-6} pc	χ^2/d.o.f.
VMEKAL	21^{+5}_{-8}	$0.28^{+0.03}_{-0.03}$	-	1	1	1	$2.0^{+0.9}_{-0.8}$	112.5/85
VMEKAL	19^{+8}_{-9}	$0.28^{+0.04}_{-0.04}$	-	1	$1.1^{+0.3}_{-0.2}$	$1.7^{+0.5}_{-0.5}$	$1.8^{+1.2}_{-0.7}$	107.1/83
VMEKAL	14^{+23}_{-14}	$0.25^{+0.06}_{-0.07}$	-	$0.4^{+0.1}_{-0.2}$	$0.9^{+1.0}_{-0.4}$	$2.0^{+0.6}_{-0.5}$	$2.8^{+3.0}_{-1.7}$	89.1/82
CEVMAL	15	3.3^c	$-2.7^{+0.2}_{-0.2}$	$0.2^{+0.2}_{-0.1}$	$1.7^{+0.4}_{-0.3}$	$2.2^{+0.7}_{-0.6}$	40^{+39}_{-23}	106.0/83

Note. — The quoted errors are at the 90% confidence level. Values without errors are fixed in the fits. See text for details. ^{a}In addition to the Galactic foreground absorption. ^{b}Abundance standard of Grevesse & Sauval (1998) is applied. ^{c}For T_{max}.

rived from the spectral fit, i.e., emission weighted, suggesting that the diffuse X-ray emission arises from such a gas filling the bulk of the circumnuclear volume.

5.4.3 The circumnuclear regions in multiwavelength

Fig. 5.1a illustrates that structures of dusty gas are developed in the inner disk regions. The distributions of circumnuclear MIR and FIR emission are further shown in Fig. 5.5, along with the Hα emission. A morphological similarity among the MIR, FIR and Hα emission is evident, indicating that the interstellar dust is associated with the ionized gas, i.e., they are both concentrated in the nuclear spiral. Apart from this overall similarity, region-to-region intensity contrasts among the MIR, FIR and Hα emission are also apparent. This is not unexpected, as both the strength of ionizing/heating sources and the density of the dusty gas could vary significantly across the circumnuclear regions.

We examine the multi-band intensity contrasts for several representative regions (Fig. 5.5c), named as follows according to their positions and appearances. The "Outer Arm" is vertically present at $\sim2'.5$ east of the M31 center. Outward, it spirals a winding angle of about $\pi/2$ and is rooted at the outermost spiral arm at northwest (Fig. 5.1a); inward, it turns northwestward and peaks in all the bands where it ap-
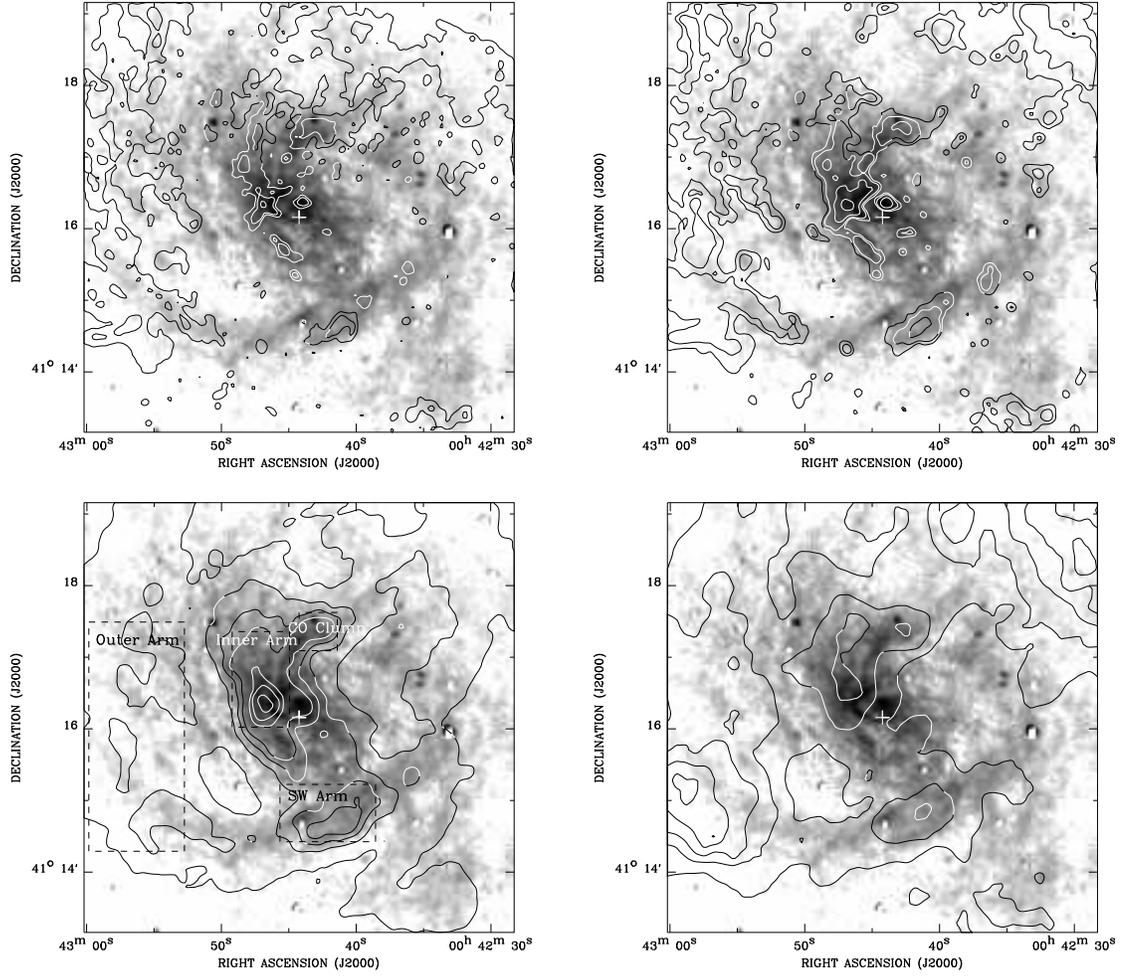
Figure 5.5 Contours of (a) 8 μm, (b) 24 μm, (c) 70 μm and (d) 160 μm emission overlaid on the Hα image of the central 6' by 6' region, in arbitrary units. The dashed rectangles marked in (c) outline the selected regions for examination of multiwavelength correlations. See text for details.

proximately intersects the major-axis at southwest, and we refer to this region as the "SW Arm". The clump showing CO emission (§ 5.2) is prominent in all the bands and is called the "CO Clump". Finally, an arcmin-long filament appears coherent at northwest to the center and is referred to as the "Inner Arm". The multi-band intensities, defined as νI_ν, of the four regions are measured from the images and summarized in Table 5.2. We further show in Fig. 5.6a for the individual regions various intensity ratios versus the FIR intensity, $(\nu I_\nu)_{\rm FIR} \equiv (\nu I_\nu)_{70} + (\nu I_\nu)_{160}$. Although limited in number, the selected regions well sample the FIR intensity at values above

Table 5.2. Multiwavelength properties of the nuclear spiral in selected regions

Region (1)	Position (2)	Size (3)	$(\nu I_\nu)_8$ (4)	$(\nu I_\nu)_{24}$ (5)	$(\nu I_\nu)_{70}$ (6)	$(\nu I_\nu)_{160}$ (7)	$(\nu I_\nu)_{H_\alpha}$ (8)	T_h (9)	M_d (10)
Outer Arm	$(-136'', -16'')$	$80'' \times 192''$	5.0 ± 0.6	0.9 ± 0.1	12 ± 1.2	9.8 ± 1.0	11 ± 2.3	50	28
SW Arm	$(24'', 80'')$	$80'' \times 48''$	3.6 ± 0.8	0.6 ± 0.2	18 ± 1.8	8.3 ± 0.8	25 ± 5.0	45	3.9
CO Clump	$(16'', 72'')$	$32'' \times 32''$	7.2 ± 1.0	1.2 ± 0.2	21 ± 2.1	9.3 ± 0.9	35 ± 6.9	48	1.3
Inner Arm	$(-32'', 32'')$	$48'' \times 80''$	4.7 ± 1.4	1.4 ± 0.4	26 ± 2.6	9.2 ± 0.9	46 ± 9.2	48	3.7

Note. — (1)-(3): Rectangular regions as defined in § 5.4.3, their centroid positions with respect to the M31 center, and sizes; (4)-(8): Multiwavelength intensities in units of 10^{-4} ergs cm^{-2} s^{-1} sr^{-1}. The quoted errors account for a 10% calibration uncertainty for the MIR/FIR intensities and a 20% for the Hα intensity. A 5-10% uncertainty due to the removal of stellar contribution in the 8 and 24 μm emission is also propagated into the quoted errors; (9) Temperature of the warm dust component, in units of K; (10) Dust mass, in units of 10^3 M$_\odot$.

2.0×10^{-3} ergs cm^{-2} s^{-1} sr^{-1}. The ratio of $(\nu I_\nu)_{70}/(\nu I_\nu)_{160}$ increases with $(\nu I_\nu)_{\text{FIR}}$, implying that the stronger FIR emission is more weighted by warmer dust. Furthermore, both $(\nu I_\nu)_{70}/(\nu I_\nu)_{160}$ and $(\nu I_\nu)_{\text{FIR}}$ show the lowest (highest) value at the Outer (Inner) Arm, i.e., generally increase with decreasing distances from the center. Such a trend is consistent with the bulge stellar radiation field, which is presumably responsible to heating the dust, being stronger at smaller galactocentric radii.

The ratio of $(\nu I_\nu)_{24}/(\nu I_\nu)_{\text{FIR}}$, on the other hand, varies little among the different regions. It can be shown that in each region the MIPS intensity ratios are inconsistent with a single dust temperature. A full accounting of the broadband IR spectral energy distribution (SED) requires a physical model of interstellar dust (e.g., Li & Draine 2001), which is beyond the scope of the present study. Instead, we simply assume that the observed MIR/FIR emission can be reproduced by two distinct dust components, each characterized by the color temperature of a diluted blackbody, i.e., a λ^{-1} emissivity law. Therefore in each region, the MIPS intensities can be expressed by (e.g., Goudfrooij & de Jong 1995):

$$I_\nu = K_l \lambda_\mu^{-4} [e^{1.44\times10^4/(\lambda_\mu T_l)} - 1]^{-1} + K_h \lambda_\mu^{-4} [e^{1.44\times10^4/(\lambda_\mu T_h)} - 1]^{-1}, \qquad (5.1)$$
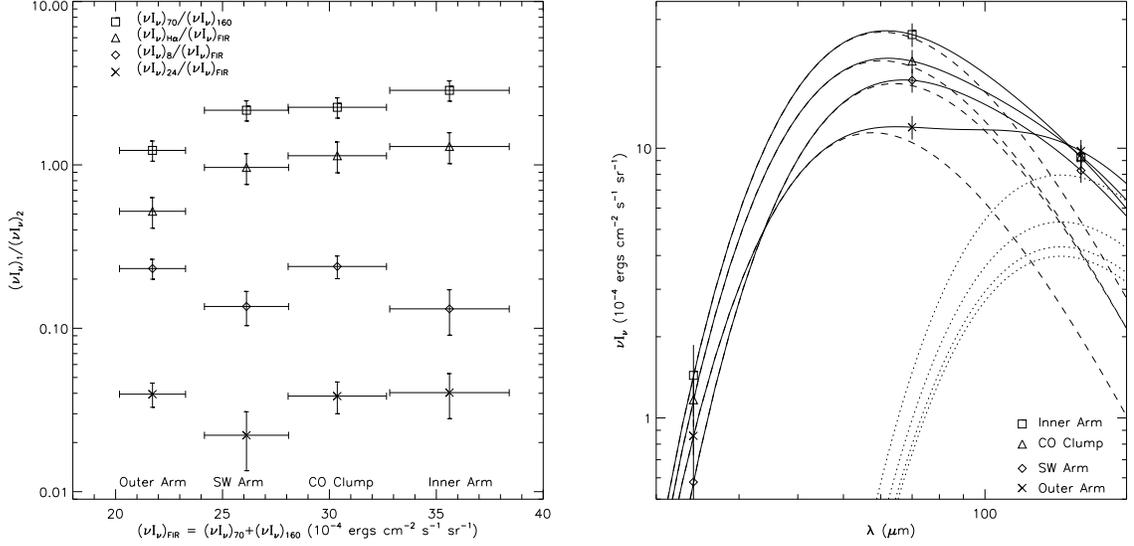
Figure 5.6 (a) Intensity ratios as a function of the FIR intensity for selected circum-nuclear regions. (b) The MIPS 24, 70 and 160 μm intensities characterized by a two-component dust emission model (solid curves). The low- and high- temperature components are represented by the dotted and dash curves, respectively. See text for details.

where λ_μ (= 24, 70, 160) and I_ν are in units of μm and MJy sr^{-1}, respectively. The 8 μm emission, presumably arising from line emission of PAH particles, is not considered here. Since the four unknowns in Eq. 5.1 can not be completely determined with the three MIPS bands, we further assume $T_l = 20$ K for the cold dust component. Presence of cooler dust is possible, but the emission of which would be largely beyond the wavelength coverage of the MIPS. The remaining unknowns can then be solved for individual regions. The results (Table 5.2) indicate that the temperature of the warm dust component, T_h, ranges between 45-50 K, and that the relative contribution of this component to the 70 μm emission increases from 88% at the Outer Arm to 97% at the Inner Arm (Fig. 5.5b). We further estimate the dust mass according to $M_d = 5.1 \times 10^{-2} d^2 (K_l + K_h)$ M$_\odot$ (Goudfrooij & de Jong 1995), where $d = 0.78$ is the distance of M31 in Mpc. In particular, a dust mass of 1.3×10^3 M$_\odot$, or a gas mass of 1.3×10^5 M$_\odot$ (assuming a dust-to-gas mass ratio of 0.01), is inferred for the CO Clump. Corrected for the considered area, this value is about four times higher than

that derived from optical extinction (Melchior et al. 2000). Such a discrepancy, often encountered in the determination of dust mass in elliptical galaxies (e.g., Goudfrooij & de Jong 1995), does not necessarily cast serious doubt to our results, in view of the disadvantage of extinction study to probe a diffusely distributed component of dust. On the other hand, it is worth to note that the estimated mass is much weighted by the low-temperature component and thus dependent on the less certain value of T_l. An adoption of $T_l = 25$ K, for instance, would result in typically 50% less mass. The equivalent hydrogen column density is inferred to be $(1\text{-}2)\times10^{21}$ cm^{-2} for the four regions, consistent with the value inferred from the X-ray spectral fit (Table 5.1).

A zoom-in view of cross-correlations among the 24 μm, Hα, UV and X-ray emission in the central 3$'$ by 3$'$ region is presented in Fig. 5.7. The FIR emission, limited in spatial resolution in this region, is expected to be represented by the 24 μm emission. Within the central $\sim$1$'$, both the Hα and 24 μm emission appear filamentary at the resolution of few arcseconds (Fig. 5.7a). It is now clear that the CO Clump is part of an arm-like filament. Inward, this filament joins the Inner Arm at $\sim$30$''$ east to the center, where the 24 μm emission peaks, and further extends southwestward across the minor-axis. The association between the Hα and 24 μm emission along these features is evident. There is no further trace of coherent feature of 24 μm emission, however, on the southwestern side to the center, where the nuclear spiral is still prominent in Hα emission. Except for its presence at a bright knot located $\sim$15$''$ north to the center, the 24 μm emission is also largely absent towards the very central regions, where the Hα and diffuse X-ray emission also show a sign of flattening (Fig. 5.3c). Interestingly, the Hα emission, wherever it is seen associated with the 24 μm emission, appears limb-brightened at the side facing the galactic center.

Immediately close to the nuclear spiral, the diffuse X-ray emission appears clumpy and enhanced with respect to the overall elongated morphology along the minor-axis (Fig. 5.7b). As shown in Fig. 5.7c, there is no clear correlation between the X-ray in-
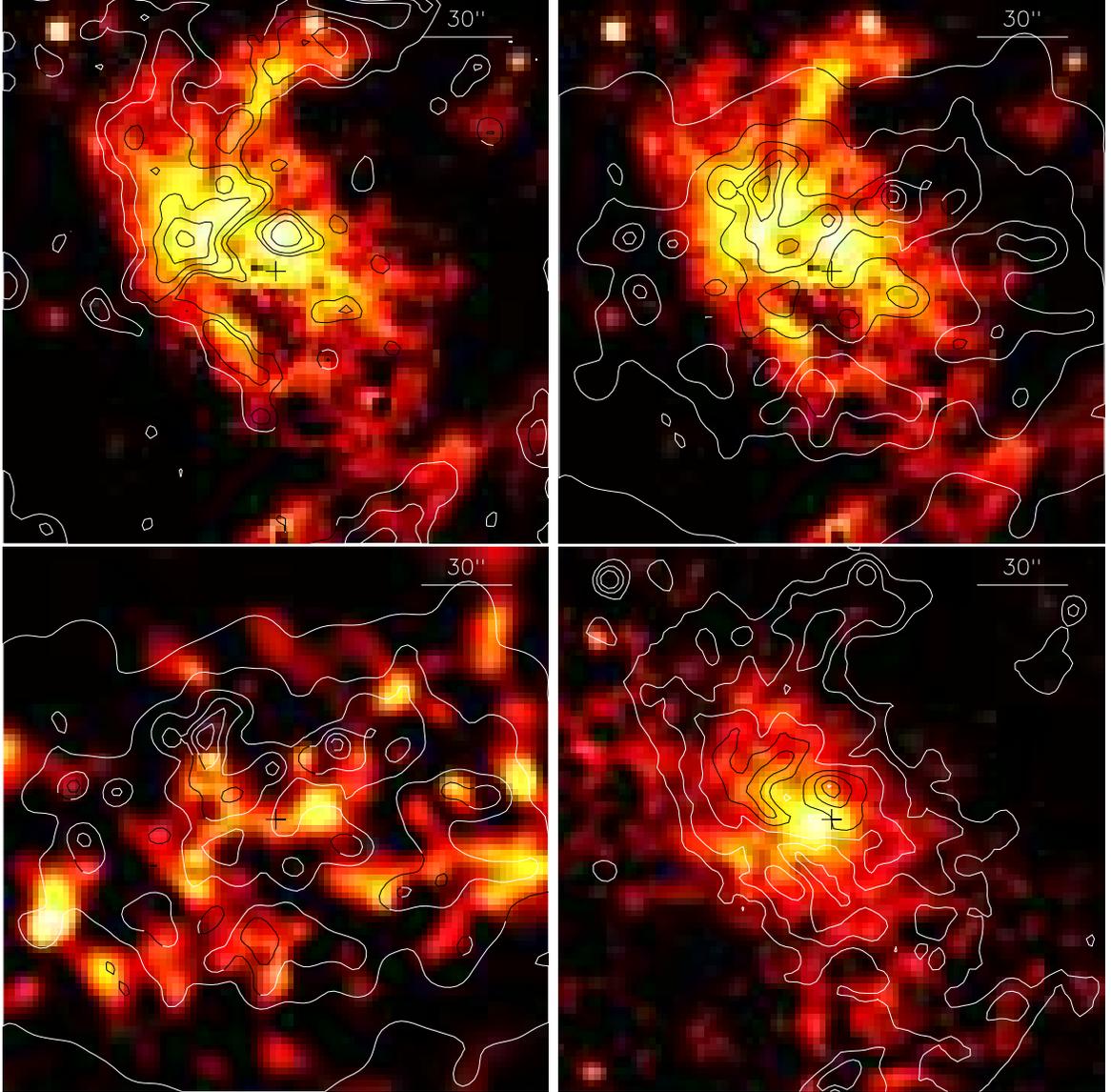
Figure 5.7 A multiwavelength view of the central $3'$ by $3'$ region. (a) Contours of 24 μm emission overlaid on the Hα image. (b) Contours of 0.5-2 keV diffuse X-ray emission overlaid on the Hα image. (c) Contours of 0.5-2 keV diffuse X-ray emission overlaid on the X-ray hardness ratio map. (d) Contours of Hα emission overlaid on the $(NUV - FUV)$ color map.

tensity and the hardness ratio, defined as $(I_{1-2 \text{ keV}} - I_{0.5-1 \text{ keV}})/(I_{1-2 \text{ keV}} + I_{0.5-1 \text{ keV}})$, indicating that the X-ray clumpiness is not merely a result of spatially varying obscuration. Rather, the observed X-ray enhancement close to the nuclear spiral, albeit a picture complicated by the projection effect, suggests a physical relation between the hot and cooler gas. We shall further address this issue in § 5.5.

Like the MIR emission, the NUV and FUV emission in the central few arcmins show a bulge-like morphology and hence most likely arise from evolved stars (King et al. 1992). It is evident from the radial intensity distributions that the FUV emission enhances more steeply toward the center than the NUV emission does (Thilker et al. 2005), suggesting a gradual change of the stellar UV SED. Such a trend is illustrated in Fig. 5.7d, where the 2-D distribution of $(m_{\mathrm{NUV}} - m_{\mathrm{FUV}})$ is shown along with the Hα emission. For reference, the color, $m_{\mathrm{NUV}} - m_{\mathrm{FUV}}$, has a mean value of ~ -0.95 within the central $30''$, about 0.2 higher than that in the regions immediately beyond. Most surprisingly, the overall morphology of the $(NUV - FUV)$ color is similar to that of the nuclear spiral rather than that of the bulge, indicating that the apparent rising of the FUV emission relative to the NUV emission is not simply due to a radial change of the stellar SED. In principle, the excess could be the result of differential extinction introduced by the cold ISM residing in the nuclear spiral. Quantitatively, adopting $A_{\mathrm{FUV}}/E(B - V) = 8.376$, $A_{\mathrm{NUV}}/E(B - V) = 8.741$ (Wyder et al. 2005; based on the extinction law of Cardelli, Clayton & Mathis 1989), $N_{\mathrm{H}}/E(B - V) = 6 \times 10^{21}$ atom cm^{-2} mag^{-1} and an equivalent hydrogen column of 10^{21} cm^{-2}, the differential extinction is estimated to be $A_{\mathrm{NUV}} - A_{\mathrm{FUV}} \approx 0.06$ and not able to fully account for the observed color excess. That there is no color excess seen at the position of the CO Clump also indicates that differential extinction has a minor effect.

Alternatively, the color excess could be due to intrinsic FUV emission associated with the nuclear spiral. We seek evidence for such a possibility from the FUSE spectrum of the central $30''$. At a glance the spectrum, in particular the prominent Lyβ absorption feature, seems to be typical of hot subdwarf stars (Brown et al. 1996) that are generally thought to be responsible for the unresolved FUV emission in the inner bulge (Brown et al. 1998; see below). On the other hand, OVI absorption lines, not characteristic of the SED of hot subdwarfs, are clearly present (the S/N near the

94

O VI-1031 line is 9.3), implying for an interstellar origin. We determine the continuum across the O VI doublet by fitting a second-order polynomial through absorption-line-free regions between 1028 and 1047 Å. We also measure the H_2 column density, using the method described by Wakker (2006). H_2 is detected both in the Milky Way and in M31. For the Milky Way we find $\log N(H_2)$=18.78, centered at a velocity of 1 km s^{-1}, while for M31 we find $\log N(H_2)$=15.19, centered at -300 km s^{-1}. Fig. 5.8 shows the resulting data (histogram) and continuum fit (continuous line). The Galactic O VIλ1031.926 absorption is relatively weak, being $\log N(OVI)$=13.76±0.17±0.04), as is the case for other sightlines in this part of the sky (Wakker et al. 2003). Here the first error is the statistical error associated with the noise in the data and the uncertainty in the placement of the continuum, while the second error is the systematic error associated with fixed-pattern noise and a 10 km s^{-1} uncertainty in the choice of the velocity limits of the integration (see Wakker et al. 2003 for details).

The O VIλ1031.926 associated with M31, centered at -265 km s^{-1}, is contaminated by Galactic H_2 LP(3) 6-0 λ1031.191, while the O VIλ1037.617 line is contaminated by H_2 LR(1) 5-0 λ1037.149 and LR(0) 5-0 λ1036.545. After correcting for the H_2 line, we find an equivalent width for the M31 O VIλ1031.926 line of 392±26±10 mÅ. The absorption profile can be converted into an apparent optical depth profile: $N_a(v) = 2.76 \times 10^{12}$ log(cont/flux). By comparing the apparent optical depth profiles of the two O VI lines it is possible to assess whether the line is saturated. We show the apparent optical depth profiles of the two lines in the right two panels of Fig. 5.8, with the caveat that the O VI-1037 line can be trusted only in a narrow range in velocities between -280 and -220 km s^{-1}. In this velocity range, the apparent column densities of the two O VI lines match, showing that the O VIλ1031.926 line is not saturated. Then, integrating from -370 to -140 km s^{-1}, we find an O VI column density of $\log N(O\ VI)$=14.75±0.06±0.03.

−400 −200 0   −400 −200 0

EW=392±26±10 mÅ   log N(OVI) = 14.75±0.06±0.03   9E+12

2.4

6E+12

1.6

3E+12

0.8

R4
0.0 R3   0

2.4   9E+12

6E+12

1.6

3E+12

0.8 CII*
CII   CII*   R2
R1   P1
0.0   R1
−400 −200 0   −400 −200 0

velocity [km s⁻¹]   velocity [km s⁻¹]

Flux [erg cm⁻² s⁻¹ Å⁻¹]

$N_a(v)$ [cm⁻² (km s⁻¹)⁻¹]
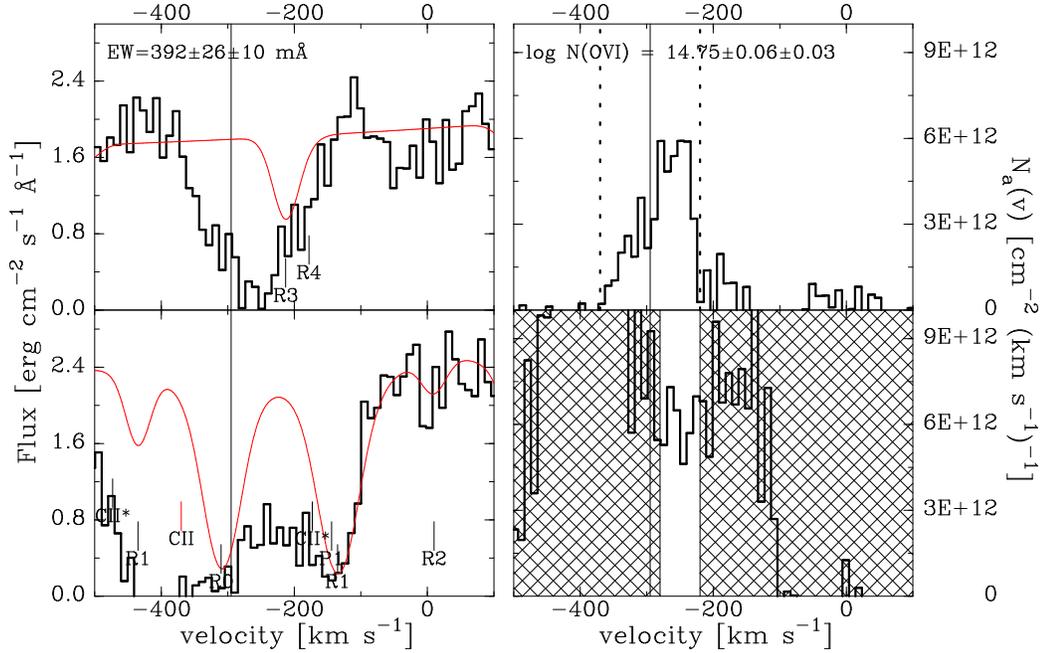
Figure 5.8 FUSE spectrum of the central 30″ of M31 (*histogram*) and a fit to the continuum (*continuous line*).

It is not *a priori* clear that all of this O VI absorption is associated with the M31 core. In almost all sightlines in the region of sky within about 40° from M31 there are two high-negative velocity O VI absorption components, centered at about −300 and −150 km s⁻¹. Sembach et al. (2003) associated the former with a possible extension of the Magellanic Stream, while the latter may represent gas distributed through Local Group, although this is a tentative interpretation. Braun & Thilker (2004) later discovered that there is faint HI emission in this part of the sky, with velocities that are continuous with those of the Magellanic Stream. The O VI column density in the −300 km s⁻¹ component is log N(O VI)=14.22±0.05 in a sightline about 1°9 from the M31 center (toward the QSO RX J0048.3+3941), which is at the high end of O VI column densities found for this component. Therefore, it is likely that some fraction of the O VI column density seen toward the M31 core originates in the Magellanic Stream and between the Milky Way and M31. However, even if these contribute as much as log N(O VI)=14.20 (1.6×10^{14} cm⁻²), the remainder (4×10^{14} cm⁻²) is likely

to originate in the M31 core, implying for the presence of gas with temperatures of 10^5-10^6 K. We further discuss this possibility below.

5.5   Discussion

Based on the above multiwavelength analyses, we now explore the physical nature of various phenomena and processes in the M31 circumnuclear regions. In the central few hundred parsecs, the ISM consists of two dynamically distinct components. One is the nuclear spiral with a low volume filling factor, consisting of cold dusty gas, traced by the MIR and FIR emission, and warm ionized gas, traced by optical recombination lines. The nuclear spiral is thought to be formed by bar-induced gravitational perturbations with a possibly continuous supply of gas from the outer disk regions. Connections between the nuclear spiral and the major spiral arms in the outer disk are evident in Fig. 5.1a (see also Gordon et al. 2006). The other component is a corona of volume-filling hot gas, traced by the diffuse X-ray emission. This hot corona has a bi-polar extent of at least several kpc away from the midplane (LW07). While young massive stars are essentially absent, embedded in the hot corona there is a $\sim10^{10}$ M$_\odot$ population of old stars, which is primarily responsible for the gravitational potential and is likely so for the energetics of the ISM. Finally, there is the inactive SMBH manifesting itself only in radio and X-ray to date. Both the circular speed ($v_c \sim 270$ km s^{-1} at $r \approx 230$ pc) and the sound speed of the hot gas ($c_s \sim 280$ km s^{-1} with a temperature of 0.3 keV) imply a relatively short dynamical timescale at the order of 10^6 yr. Unless our multiwavelength view is a highly transient one, which is unlikely, there ought to be certain physical processes regulating the behavior of the multi-phase ISM as well as that of the SMBH. In the following discussion we aim primarily to propose a self-consistent scenario for this regulation.

For ease of quantification, we adopt fiducial values of the hot and warm ionized gas in the central 1′ ($\sim$230 pc) as: $n_h = 0.1$ cm^{-3}, $T_h = 4 \times 10^6$ K, $n_w = 200$ cm^{-3},

$T_w = 10^4$ K, respectively. n_h and T_h are inferred from the X-ray spectral fit (§ 5.4.2), while n_w is roughly the intensity-weighted average value inferred from [S II] line ratios (Ciardullo et al. 1988), given the canonical value of T_w for ionized gas. For both phases the notation of density is for hydrogen and, as assumed for simplicity, equally for electron. The density and temperature of the cold gas are less certain, for which we adopt $n_c = 10^4$ cm^{-3} and $T_c = 100$ K so that $n_c T_c \sim 2 n_h T_h$, the case of pressure balance. The apparently higher pressure of the warm gas can be understood if this phase represents an interface between the hot and cold phases (see § 5.5.2). Because of the high pressure environment, the bulk of hydrogen in the cold phase is likely in a molecular form (Wolfire et al. 1995), which is also suggested by the estimated mass ($\sim 5 \times 10^6$ M$_\odot$) of cold gas in the central 500 pc much exceeding the upper limit of atomic hydrogen mass ($\sim 10^6$ M$_\odot$) set by 21 cm observations (Brinks 1984). Now the mass of hot gas, $M_h \approx 1.2 \times 10^5$ M$_\odot$, is a straightforward measurement based on n_h and the considered volume $V \approx 1.5 \times 10^{63}$ cm^3. The mass of warm gas, $M_w \approx 3.2 \times 10^3$ M$_\odot$, is estimated from the Hα emission by assuming a standard case B emissivity and a [N II]/Hα intensity ratio of 2. The mass of cold gas, $M_c \approx 10^6$ M$_\odot$, is inferred from the MIR/FIR emission using the procedure described in § 5.4.3.

5.5.1 Accretion and feedback of the nucleus

M31*, with a 0.3-7 keV luminosity of 1.2×10^{36} ergs s^{-1}, ranks as the second faintest galactic nucleus detected in X-ray, after Sgr A*, but comparable to M32* (Ho, Terashima & Ulvestad 2003, who found a 2-10 keV luminosity of 10^{36} ergs s^{-1}). Assuming that the X-ray emission typically accounts for $\sim 10\%$ of the bolometric luminosity, we have $L_{\rm bol} \sim 10^{37}$ ergs s^{-1}, in comparison to the Eddington luminosity of $L_{\rm Edd} \approx 10^{46} (M_{\rm BH}/10^8$ M$_\odot)$ ergs s^{-1}, where $M_{\rm BH}$ is the mass of the SMBH. Either the hot gas or the cold gas in the circumnuclear environment is sufficiently massive to feed M31* for a time up to 10 Gyr at its present accretion rate. For instance, assuming

that M31* is powered by the Bondi accretion (1952) of the soft X-ray-emitting hot gas, the accretion rate can be estimated as:

$$\dot{M}_{\rm Bondi} \approx 4\pi\lambda m_{\rm H} n_h (GM_{\rm BH})^2 c_s^{-3} \tag{5.2}$$

$$\approx 5.5 \times 10^{-5} \left(\frac{n_h}{0.1~{\rm cm}^{-3}}\right)\left(\frac{M_{\rm BH}}{10^8~{\rm M}_\odot}\right)^2\left(\frac{c_s}{300~{\rm km~s}^{-1}}\right)^{-3}~{\rm M}_\odot~{\rm yr}^{-1},$$

where λ is a numerical factor taken to be 0.25 and the rest symbols are of conventional meanings if not yet defined above. The corresponding *Bondi luminosity* is $L_{\rm Bondi} \equiv \eta \dot{M}_{\rm Bondi} c^2 \approx 3.1 \times 10^{41}(\eta/0.1)$ ergs s^{-1}, where η is the radiation efficiency. It follows that $L_{\rm bol}/L_{\rm Bondi} \sim 10^{-5}$, indicating that the radiation of M31* is highly inefficient, i.e., $\eta \ll 0.1$. The estimated Bondi accretion rate could be somewhat biased, as we do not have a precise knowledge on the physical properties of the accretion flow on pc-scales. Regardless, the radiation efficiency of M31* is likely low, as predicted by models of advection-dominated accretion flow with typically low accretion rates ($\dot{M}_{\rm acc}/\dot{M}_{\rm Edd} \ll 1$; Narayan & Yi 1995).

On the other hand, it is not fully understood what mechanisms act to remove the angular momentum of gas originating from the $r \sim 100$ pc regions and then to transport the gas to the sub-pc vicinity of the SMBH (Wada 2004). In any case, this theoretical difficulty does not seem to pertain to M31. We recall that there is no clear evidence of gas gathering into the central few parsecs of M31 (§ 5.4.3); any coherent entity of cold gas is apparently located at a distance $\gtrsim 50$ pc. This is contradicted with the presence of gas inflow, favorably induced by the bar potential and forming the nuclear spiral. It is sometimes suggested by numerical models (e.g., Maciejewski 2004) that the inflowing gas ultimately settles in quasi-circular orbits, where the orbital energy is minimum for a given angular momentum, forming a so-called *nuclear ring*. Accumulation of gas on such orbits are expected to be subject to gravitational instability that leads to star formation, by which the ring manifests itself in observations (e.g., Sarzi et al. 2007), or to a further infall to the galactic

center, activating the nucleus. *Neither* situation is observed in M31, whereas there is no reason to argue that the global gas inflow has been stopped. In this regard, the right question to ask for M31 seems to be: what mechanism prevents gas from gathering into the $r \lesssim 50$ pc region? We shall further address this issue below.

Alternatively, M31* can obtain fuel from its immediate surroundings, i.e., the eccentric stellar disk consisting of a $\sim 2 \times 10^7$ M$_\odot$ population of old stars (Tremaine 1995). It is expected that these stars lose mass via stellar winds at a rate of $\sim 10^{-4}$ M$_\odot$ yr^{-1} (e.g., Ciotti et al. 1991), a value comparable to the above estimated Bondi accretion rate. Chang et al. (2007) argued that the stellar winds are trapped by the stellar disk and eventually collapse to form a thin gaseous disk orbiting around the SMBH on pc-scales, and that star formation can be triggered from the gaseous disk every 0.1-1 Gyr, consistent with the 200 Myr starburst proposed for P3 (§ 5.2). These authors noticed that, given the estimated mass of a few 10^3 M$_\odot$ for P3, the star formation efficiency is $\sim 10\%$-20%. The remaining gas could then be accreted by the SMBH, although details of such a process remain unclear.

It is not trivial to quantify feedback from galactic nuclei, even for the inactive ones such as M31*. Much of the feedback is expected to be carried out by jets of relativistic particles, especially for "faint" nuclei showing a low radiation efficiency. Allen et al. (2006) found an empirical relation between accretion rate and jet power in X-ray-bright elliptical galaxies, quantitatively as: $\log(L_{\mathrm{Bondi}}/10^{43}$ ergs s$^{-1}) = 0.65 + 0.77\log(L_{\mathrm{jet}}/10^{43}$ ergs s$^{-1})$. The Bondi accretion rate of their sample nuclei ranges from 3.5×10^{-4} M$_\odot$ yr^{-1} to 4.6×10^{-2} M$_\odot$ yr^{-1}. It is not known *a priori* how the relation behaves at lower accretion rates. If it holds for M31*, the jet power would then be $\sim 1.6 \times 10^{40}$ ergs s^{-1}, or about 5% of the Bondi luminosity. In principle, this powerful nuclear feedback can result in an X-ray cavity, as hinted by the central flattening of the X-ray intensity (Fig. 5.3c and Fig. 5.7b). Another possible signature of the feedback is the energetic particles inferred to be present along the nuclear

100

spiral (§ 5.2), although it is also possible that they are originated from SN events. High-resolution, high-sensitivity radio observations will help to clarify this issue.

5.5.2 The origin, role, and fate of the hot gas

The study of the circumnuclear diffuse X-ray emission (§ 5.4.2) reveals the unambiguous presence of hot gas in the core of M31. The next question to address is what supplies the hot gas. Diffuse hot gas is commonly found in the cores of early-type galaxies. Proposed origins of hot gas include accretion of the intergalactic medium (IGM), typically prevalent in massive, high-L_X elliptical galaxies, and the collective ejecta of local evolved stars, likely predominant in low-L_X early-type galaxies. In the latter case, the most important heating source of the stellar ejecta is thought to be Type Ia SNe (e.g., Ciotti et al. 1991; David et al. 2006). This should be the case in the M31 bulge, where the SMBH is quiescent and there is no recent massive star formation. In the present-day universe, a stellar spheroid empirically deposits energy and mass at rates of $\sim 1.1 \times 10^{40}[L_K/(10^{10}L_{\odot,K})]$ ergs s^{-1} (Mannucci et al. 2005) and $\sim 2 \times 10^{-2}[L_K/(10^{10}L_{\odot,K})]$ M$_\odot$ yr^{-1} (Knapp, Gunn & Wynn-Williams 1992), respectively, given an energy release of 10^{51} ergs per SN Ia. Assuming an SN heating efficiency $\epsilon \sim 1$ and that the stellar mass loss is wholly involved, an average energy input of ~ 3.6 keV per gas particle is inferred. The gravitational potential of a normal galaxy is unlikely to confine the gas with such a high temperature. Therefore the gas is expected to escape, at least from inner regions of the host galaxy. Indeed, for many early-type galaxies the observed X-ray luminosity of hot gas, L_X, is typically no more than a few percent of the expected energy input rate from SNe Ia (e.g., David et al. 2006; Li, Wang & Hameed 2007; LW07); the inferred gas mass is also much less than expected if the stellar ejecta has been accumulated for a substantial fraction of the host galaxy's lifetime. Such discrepancies can be naturally explained

with the presence of an outflow of hot gas, in which the "missing" energy and mass are transported outside the regions covered by the observations.

It can be shown that the stellar feedback is also largely missing in the core of M31. For the central arcmin we have $L_X \approx 7 \times 10^{37}$ ergs s^{-1} and $M_h \approx 10^5$ M$_\odot$, whereas the SN heating rate is $\sim 5 \times 10^{39}$ ergs s^{-1} and the mass input rate is ~ 0.01 M$_\odot$ yr^{-1} (taking only $\sim 10^7$ yr to accumulate the observed amount of hot gas). Clearly, these suggest an outflow launched in the circumnuclear regions, as already hinted by the X-ray morphology (§ 5.4.2). On the other hand, the fitted gas temperature in the M31 core, ~ 0.3 keV (§ 5.4.2), is much lower than the maximum allowed temperature of ~ 3.6 keV ($\epsilon \sim 1$),

That $\epsilon \sim 1$ is often implicitly assumed in the context of early-type galaxies, in which individual SNe occur in volume-filling hot gas. The SN blast wave does not dissipate easily and can effectively convert mechanical energy into thermal energy (i.e., $\epsilon \sim 1$; Tang & Wang 2005). In the case of M31, dissipation of the blast wave could become important when it encounters the cold, dense gas of the nuclear spiral. The amount of energy loss in such a process, via mechanical and radiational dissipations, depends on the geometry of the encounter and the local gas density (e.g., McKee & Cowie 1975), but is unlikely large enough to result in $\epsilon < 0.5$, as the solid angle covered by the nuclear spiral with respect to the wave front must be less than 2π.

Alternatively, a reduced gas temperature is expected given mass input additional to the stellar deposition. In particular, this is conceivable via thermal conduction between the hot gas and the nuclear spiral. Evaporation of the cold gas at an appropriate rate would result in a "mass-loading" to the hot gas, a process we shall now consider. We assume that the nuclear spiral is composed by discrete cloudlets. The geometry of the cloudlets, which determines the evaporation rate, is rather uncertain. Here as a first order approximation we consider spherical cloudlets having a characteristic radius $R_s = R_{\rm pc}$ pc. Only those cloudlets that are smaller than a crit-

ical radius, $R_{\rm crit} \approx 4.8 \times 10^5 T_h^2 n_h^{-1}$ cm ≈ 25 pc, would be evaporating; condensation would be more likely to take place for larger ones upon radiative cooling (McKee & Cowie 1977). While the large CO Clump may be in this latter case, most cloudlets in the region, essentially unresolved under the few-arcsec resolution, appear to be small enough to undergo evaporation. In regions where the Hα and MIR emission are associated, the cold neutral gas most likely resides in the cores of the cloudlets with evaporating, ionized outer layers; in regions where only the Hα emission is prominent, the cloudlets are likely in the late stages of evaporation and fully ionized. The number of cold cloudlets, N_c, satisfies $(4\pi/3)R_s^3 N_c n_c m_H = M_c$, or $N_c R_{\rm pc}^3 \approx 960(M_c/10^6 \ {\rm M_\odot})$. Similarly, for the warm cloudlets we have $(4\pi/3)R_s^3 N_w n_w m_{\rm H} = M_w$, or $N_w R_{\rm pc}^3 \approx 160$. If $N_c \sim N_w$, the size of the warm cloudlets is about half that of the cold cloudlets, consistent with a reduced size due to early evaporation. The classical thermal conductivity (Spitzer 1962) holds when the mean free path of conducting electrons, $\lambda \approx 10^4 T_h^2 n_h^{-1}$ cm ≈ 0.5 pc, is shorter than the scale-length of temperature variation, roughly being the cloudlet radius. Adopting $R_{\rm pc} = 0.5$ and assuming that classical evaporation applies, the total evaporation rate of the cold cloudlets is $\dot{M}_{\rm evap} \approx 2.75 \times 10^4 T_h^{5/2} R_{\rm pc} N_c$ g s$^{-1} \approx 0.05 \ {\rm M_\odot}$ yr^{-1} (Cowie & McKee 1977), implying a corresponding mass input rate about five times that of the stellar ejecta to the $r \lesssim 230$ pc region. An additional evaporation of $\sim 0.01 \ {\rm M_\odot}$ yr^{-1} may arise from the fully ionized cloudlets. For cloudlets of smaller initial sizes, the conduction becomes saturated and the evaporation rate from individual cloudlets drops significantly (Cowie & McKee 1977), but the correspondingly number of cloudlets must increase to conserve the total gas mass and hence could result in a comparable $\dot{M}_{\rm evap}$.

Several self-consistency checks are needed before concluding the likelihood of the above scenario. First, the evaporation timescale is $t_{\rm evap} \sim 2 \times 10^7$ yr, not much longer than the time needed for the cold gas to spiral an angle of 2π, $t_{\rm evap} \approx 2\pi r/v_c \sim 5 \times 10^6$ yr. Thus the gas is likely to be evaporated before spiraling into the very

central regions. This naturally explains the observed X-ray enhancement coincident with the Inner Arm as well as the lack of cold gas observed in the $r \lesssim 50$ pc regions (§ 5.4.3; Fig. 5.7). Second, although difficult to measure, a gas inflow rate of ~ 0.05 $M_\odot$ yr^{-1} from the outer disk regions of M31 is entirely possible. Typical gas inflow rates of 0.1-1 $M_\odot$ yr^{-1} are suggested for barred spirals (e.g., Quillen et al. 1995; Sakamoto et al. 1999), which often lead to an observed concentration of 10^8-10^9 $M_\odot$ neutral gas in the central kpc. In contrast, the gas mass in the central kpc of M31 is merely $\sim 10^7$ $M_\odot$. Without consumption of gas by star formation, this lack of gas concentration is most likely due to the evaporation process discussed above. In this regard, the maximum evaporation rate afforded by a hot corona in barred spirals is likely ~ 0.1 $M_\odot$ yr^{-1}. Third, the implied mass-loading rate to the corona results in a reduced heating per gas particle that is about right for the measured temperature of the hot gas. The mass-loading also predicts a dilution of metallicity for the hot gas. In particular, the iron abundance is expected to be $Z_{\rm Fe} \approx 9.7(M_{\rm Fe}/0.7 M_\odot)$ due to SN Ia enrichment (Nomoto, Thielemann & Yokoi 1984) of the collective stellar ejecta alone. The measured $Z_{\rm Fe}$, $\sim$ 1-2 solar (Table 5.1), is consistent with the predicted dilution. It is not immediately clear, however, how a supersolar abundance of Mg and a subsolar abundance of O are simultaneously derived from the mass-loading. One possibility is that the Mg abundance reflects the primary Type II SNe enrichment at the outer disk regions before gas inflowing to the nuclear spiral. The O abundance, on the other hand, might have been underestimated, in a sense that the resonance scattering of the O VII and O VIII Kα line emission, being optically thick if the velocity dispersion of the hot gas is not far from its thermal broadening, is not properly accounted for in the spectral fit.

5.5.3 Ionizing and heating sources of the nuclear spiral

With the above information, we shall now revisit the ionizing source of the nuclear spiral in M31, a long-standing puzzle (Devereux et al. 1994). Assuming a [N II]/Hα intensity ratio of 2 and that every recombination produces 0.45 Hα photon, the observed Hα+[N II] flux of 1.1×10^{-11} ergs s^{-1} cm^{-2} within the central arcmin implies a recombination rate $R \approx 2 \times 10^{50}$ s^{-1}. In the absence of massive young stars, possible sources for the ionizing photons include: i) UV radiation of old stellar populations; ii) X-ray photons from the hot gas as well as stellar objects; iii) UV photons induced by thermal conduction; iv) UV photons induced by shocks; and v) cosmic-rays produced by the nucleus or SN events. Below we access the relative importance of these sources.

Extended recombination line emission, particularly Hα emission, is often observed in elliptical galaxies. Binette et al. (1994) demonstrated that the ionizing photons from post-AGB stars with effective temperatures of $\sim 10^5$ K are typically sufficient to account for the observed Hα emission. The Hα intensity is found to be correlated with the optical luminosity within regions of the line emission (Macchetto et al. 1996), further suggesting a stellar origin of the ionizing photons in elliptical galaxies. According to Binette et al. (1994), post-AGB stars provide ionizing photons (i.e., shortward of 912 Å) at a rate of 7.3×10^{40} s^{-1} M$_\odot^{-1}$. In the central arcmin of M31, this gives a recombination rate of $R \approx 2.9g \times 10^{50}$ s^{-1}, where $g \lesssim 0.5$ is a geometric factor that determines the fraction of ionizing photons received by the nuclear spiral.

It is also possible that the ionizing photons are related to the so-called *UV-upturn*, a rise in the SED shortward of ~ 2500 Å observed in elliptical galaxies as well as the M31 core (Burstein et al. 1988). In view of the lack of young stars, the UV-upturn is generally attributed to the emission of hot horizontal branch (HB) stars (e.g., Brown et al. 1998), with an effective temperature of a few 10^4 K. Such stars could be simultaneously responsible for the UV-upturn and the recombination line emission observed in M31. According to the lastest model for the UV-upturn (Han et al. 2007;

Han 2008, private communications), HB stars produce ionizing photons at a rate of 1.4×10^{40} s^{-1} M$_\odot^{-1}$, responsible to a recombination rate of $R \approx 5.6g \times 10^{49}$ s^{-1} in the central arcmin of M31.

Ionization by X-rays could also be significant due to secondary ionization by photoelectrons. Assuming that on average each incident X-ray photon from the hot gas produces a 0.3 keV primary photoelectron, the number of secondary ionizations is ~ 10 (Shull 1979). The recombination rate induced by X-ray photons is then $R \approx 1.2g \times 10^{48}$ s^{-1}, according to the photon luminosity of $\sim 1.2 \times 10^{47}$ s^{-1} within the central arcmin. While stellar objects dominate the overall X-ray luminosity of M31, there are only 33 sources detected within the central arcmin (Voss & Gilfanov 2007), the corresponding covering factor g of which must be small compared to that of the volume-filling hot gas. Hence the X-ray ionization by stellar objects is ignored.

The above proposed thermal conduction is accompanied by ionizations. Ionizing photons are generated at a rate of $R \approx 2 \times 10^{-8} n_h^2 T_h^{-0.6} R_s S$ s^{-1} (McKee & Cowie 1977), where $S = 4\pi R_s^2 N_c$ is the effective area of the conduction front and the rest notations are defined above. With $N_c R_{pc}^3 = 960$, $R \approx 8 \times 10^{45}$ s^{-1}.

Shocks are likely present in the nuclear spiral either due to orbital dissipation (e.g., Englmaier & Shlosman 2000) or propagation of SN blast wave into the cold gas. Such shocks produce ionizing photons at a rate of $R = \kappa n_c v_s S$ (Shull & McKee 1979), where v_s is the shock velocity, κ a tabulated numerical factor and S the rather uncentain effective area of the shock front. Adopting $v_s = 40$ km s^{-1} and $S = (100 \text{ pc})^2$, we have $R \approx 3 \times 10^{48}$ s^{-1}.

Finally, ionizations can be induced by cosmic-rays. The ionization rate per hydrogen atom is adopted to be $5.4f^{-4/7} \times 10^{-15}$ s^{-1} (e.g., Goldsmith, Habing & Field 1969), according to 2 MeV protons with an energy density of $0.5f^{-4/7}$ eV cm^{-3} inferred from the central regions of M31 (§ 5.2; the dependancy on the volume filling

factor f is considered). With a hydrogen mass of 10^6 $M_\odot$, the recombination rate is inferred to be $R \approx 6.5 f^{-4/7} \times 10^{48}$ s^{-1}.
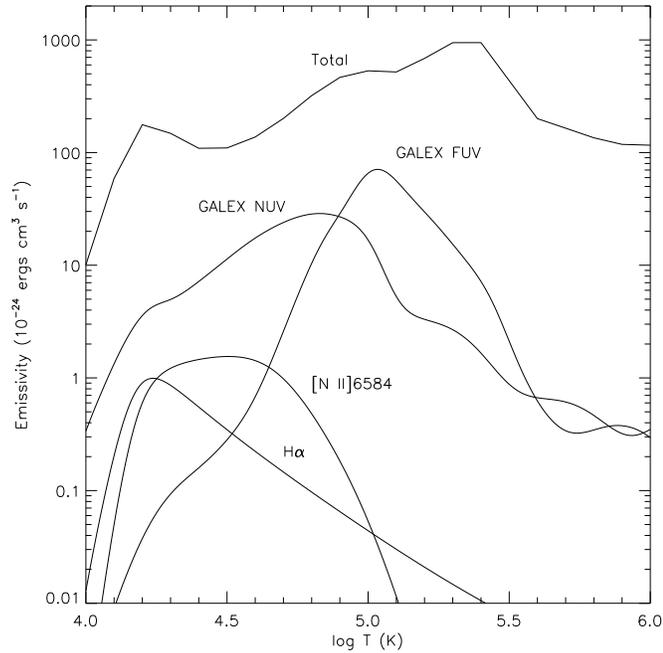
Figure 5.9 Temperature-dependent volume emissivities of selected lines and bands, for a gas of solar abundance in CIE.

From the above estimates, it is evident that the most likely ionizing source for the nuclear spiral is the stellar UV radiation predominantly contributed by the post-AGB stars, with an additional contribution from HB stars. This is consistent with the observed limb-brightened Hα emission of the filaments on the sides facing the M31 center (§ 5.4.3), where the ionizing radiation intensity peaks. However, models for the photoionization due to post-AGB stars predict an [N II]/Hα intensity ratio of $\sim$1.2 for gas with an abundance up to 3 solar (Binette et al. 1994), which is inconsistent with the high ratios (generally $\gtrsim$1.3, as large as $\sim$2.7) observed in M31 (Ciardullo et al. 1988). The relatively high intensities of low-ionization metal lines imply heating in addition to the photoionization. This is illustrated in Fig. 5.9, in which volume emissivities of Hα and [N II] lines are shown versus gas temperature in the case collisional ionization equilibrium (CIE), a reasonable approximation given the high

gas density. For instance, a temperature of $\sim 10^{4.35}$ is needed to produce a [N II]/Hα ratios of 2.

The existence of gas with temperatures between $10^4 - 10^6$ K is naturally expected at conductive interfaces between the nuclear spiral and the hot corona, which may be enhanced by turbulent mixing (Slavin, Shull, & Begelman 1993) induced by the SNe Ia shock waves. In particular, the observed FUV enhancement associated with the nuclear spiral (§ 5.4.3) likely provides one such evidence, in a sense that gas with temperatures $\gtrsim 10^5$ K exhibits its peak FUV emissivity and an FUV to NUV intensity ratio of ~ 5 (Fig. 5.9). We note, however, that a reliable quantification of the FUV emission intrinsic to the nuclear spiral is currently infeasible, due to the large uncertainties in the stellar SED and differential extinction. Nevertheless, the presence of $\gtrsim 10^5$ K gas in the M31 core is probable in view of the detected O VI absorption lines (§ 5.4.3). Assuming that the absorption arises from the conductive interfaces, for each classically evaporating cloudlet the absorption column is $N_{\rm OVI} = \int 2.5(T/T_h)^{1/2} n_h X_{\rm OVI} R_s d(T/T_h) = 2.6 \times 10^{18} n_h X_{\rm OVI} R_{\rm pc} \sim 10^{13}$ cm^{-2} (McKee & Cowie 1977), given our fiducial values (§ 5.5.2) and an abundance of 4×10^{-5} O VI ions per hydrogen atom. Within the FUSE aperture ($30'' \times 30''$) there could be a number of $N_c/4\pi$ cloudlets, therefore the predicted total absorption column is $\sim 8 \times 10^{13}$ cm^{-2}, not too far away from the observed (4×10^{13} cm^{-2}).

If a substantial fraction of the observed [N II] line (and FUV) emission is indeed arising from gas heated to $\gtrsim 10^{4.5}$ K, the total [N II] luminosity of $\sim 5 \times 10^{38}$ ergs s^{-1} then implies a heating rate at the order of 10^{40} ergs s^{-1}, as the [N II] lines typically account for only few percent of the total radiative cooling (Fig. 5.9). The energy input from SNe Ia, while responsible for the heating of the hot gas, alone may not be sufficient to account for this radiative loss. In this regard, energetic particles ejected by the nucleus are likely an additional heating source, given the above estimated jet power of 2×10^{40} ergs s^{-1}.

5.6   Summary and concluding remarks

Based on the multiwavelength data presented above we have studied M31* and its circumnuclear environment.

- We have derived a tight constraint on the X-ray luminosity of M31*, $L_{0.3-7\ \text{keV}} \lesssim 1.2 \times 10^{36}$ ergs s^{-1}. The estimated jet power from M31*, 1.6×10^{40} ergs s^{-1}, might contribute to balancing the significant radiative cooling of the nuclear spiral. Future high-sensitivity, long-duration and simulteneous X-ray/radio observations may lead to the detection of timing variabilities intrinsic to M31* and help to establish its appearance in X-ray as suggested by the present study. Such observations are also crucial for assessing the relative importance of feedback from inactive nuclei.

- We have determined a temperature of 0.3 keV and a mass of $\sim 10^5$ M$_\odot$ for the circumnuclear X-ray-emitting hot gas. We have also revealed the interaction between the hot gas and the nuclear spiral, which we suggest to be due to thermal evaporation.

- We have detected O VI absorption against the stellar UV radiation, a substantial part of which is likely associated with the bulge.

- We have proposed a self-consistent scenario in understanding much of the multiwavelength phenomena, in which thermal conduction between the hot corona and the nuclear spiral plays a crucial role. Further tests of the scenario include high-resolution imaging-spectroscopic observations of optical and UV emission lines arising from the conductive interfaces. The scenario, albeit crude in details at the moment, should have important applications on similar circumnuclear environments of spiral galaxies, in particular our Galaxy. It is also reasonable to invite its application on elliptical galaxies (e.g., Sparks, Macchetto & Golombek 1989), in which hot and cold gas are often observed to co-exist and sometimes

show morphological correlations (e.g., Trinchieri, Noris & di Serego Alighieri 1997). In the absence of a large-scale disk, elliptical galaxies may obtain a substantial supply of cold gas from galaxy mergers. In any case, thermal conduction is expected to be prevalent in the core of early-type galaxies containing typically dense, multi-phase ISM, a process previously overlooked. Numerical modeling of such a scenario will help to derive characteristics of the dynamical and thermal properties of both the hot and cold gas.

- Understanding the ISM evolution in the circumnuclear regions also allows for a better understanding of its evolution on large scales. In this regard, a detailed modeling of the hot gas as well as the O VI-absorbing gas in the M31 bulge will be our first goal.

CHAPTER 6

SUMMARY AND OUTLOOK

In the above chapters I have presented several observational studies of the hot ISM in nearby galaxies, which were carried over the past few years. In this concluding chapter I would like to comment on recent progress as well as prospects that are closely related to these studies.

In § 2 and § 3 we have seen that the observed amount of X-ray-emitting gas in the halos of NGC2613 and M104, two massive disk galaxies, is at least ten times lower than that predicted by the numerical simulations carried out in Toft et al. (2002). Shortly after our results were presented, these authors (Pedersen et al. 2006; Rasmussen 2007) claimed the finding of an extended halo of hot gas around NGC5746, another massive disk galaxy, the amount of which is consistent with the prediction of their newly performed numerical simulations. Noticeably, for a given galaxy mass, the X-ray luminosity calculated from these new simulations appear to be about ten times lower than that given by Toft et al. (2002), which is presumably due to the much enhanced spatial resolution. I note that the observed X-ray luminosity of NGC2613 is also consistent with the new calculations, while that of the more massive galaxy M104 is still several times lower than the prediction. Finding an expected amount of hot gas in the halo, however, does not guarantee the origin of the gas being external. In NGC2613, for example, the hot gas is most likely related to star formation or the active nucleus, as we have argued in § 2. It is worth noting that the hot gas in the halos ofmassive disk galaxies show relatively high temperatures (e.g., ∼0.6-0.8 keV in NGC2613, NGC5746 and M104), as compared to lower values found in less massive

ones (e.g., $\sim$0.3 keV in M31), implying that gravity does play some role in regulating the global properties of the gas.

Given its rich potentials in galactic studies, we have recently obtained deep *Chandra* ACIS-I observations of M104 (PI: C. Jones; 180 ks), which would particularly allow us to trace the X-ray-emitting gas to large radii and to probe substructures with necessary signals.

Chandra repeatedly observes the M31 bulge every year, accumulating more than 300 ks exposures to date, the first half of which has been utilized in our studies. It is valuable to maximize the use of archival data, which would particularly allow for a deep view to the circumnuclear regions. It is also important to extend the field of view along the minor-axis, in order to trace the outflow of hot gas outside the M31 bulge. This could be achieved by future *Chandra* observations as well as existed *XMM-Newton* observations.

APPENDIX

A GALACTIC WIND MODEL

Theoretical models for galactic-scale gas flows have long been developed (e.g., White & Chevalier 1983, 1984; Loewenstein & Mathews 1987; Ciotti et al. 1991), most of which are in the scope of elliptical galaxies for which spherical symmetry is reasonable approximation. White & Chevalier (1983) studied the steady state galactic wind, in which they have assumed constant supernova energy input and stellar mass loss, the rates of which are estimated at the current epoch. Stimulated by the fact that both the supernova rate and the stellar mass loss rate could be much higher at early epochs, Ciotti et al. (1991) modeled the time-dependent evolution of galactic gas flows. They proposed that the gas flow would evolve through up to three consecutive stages: the wind, subsonic outflow and inflow phases, which can in principle account for the large scatter in the observed X-ray luminosities of galaxies with similar optical luminosities (e.g., Ellis & O'Sullivan 2006). While some of these models succeeded in predicting the X-ray properties of gas in several aspects, such as the total X-ray luminosity, direct comparison with observations has been so far restricted in the scope of integrated properties of the gas. More suggestive comparison is to be carried out, in terms of confronting the model-predicted spectral and spatial properties of gas with current X-ray observations on sub-galactic scales. To do so, we construct a simple one-dimention steady-state galactic wind model, as follows.

A.1   Physical assumptions and formulation

Many of the exsited models (e.g., Loewenstein & Mathews 1987, Ciotti et al. 1991) involve detailed characterizations of various properties of an ideal galaxy, e.g., how the stars and dark matter spatially distribute, how mass and energy are loaded into the gas flow (i.e., stellar feedback). Such properties, essentially determining the gas dynamics, are practically difficult to constrain from direct observations. Our approach is to construct a model with simple but essential physical considerations, aiming to constrain the stellar feedback by confronting the model with current X-ray observations.

Our first assumption is that the gas flow is in steady state and spherical symmetry. The dynamical timescale of a wind is much shorter than the timescale of galaxy evolution, hence it is reasonable to assume that the mass and energy input from evloved stars, which together supply the gas flow, remain at a constant level. Spherical symmetry is not only a practical assumption as used in most theoretical models but also is hinted in the typical large-scale X-ray morphologies of elliptical galaxies. All physical parameters considered hereafter, e.g., gas density and temperature, are functions of galactocentric radius. Secondly, we assume that the mass and energy input spatially follow the distribution of stars. The mass input is essentially contributed by ejecta of evolved stars; the energy input is primarily provided by mechanical energy from Type Ia SNe, with an addition of orbital energy carried by the stellar ejecta.

In galaxies where outflows of gas are expected to exist, the X-ray luminosity is typically as low as to account for only a few percent of the energy input. Thus we neglect the effect of radiative cooling on the gas dynamics. We note that this assumption is not valid in the case of X-ray bright elliptical galaxies, where gas inflow is believed to be prevailing. In that case, the cooling timescale is comparable to or even significantly shorter than the dynamic timescale, making the effect of cooling

on the dynamics crucial. Other assmptions that have been made include neglecting thermal conductivity, viscosity, and self-gravity of gas.

Now the physical properties of the gas can be described by the *Euler* equations:

$$\frac{1}{r^2}\frac{d}{dr}(\rho u r^2) = \dot{m}(r), \tag{A.1}$$

$$\rho u \frac{du}{dr} = -\frac{dP}{dr} - \rho\frac{d\phi}{dr} - \dot{m}(r)u, \tag{A.2}$$

$$\frac{1}{r^2}\frac{d}{dr}[\rho u r^2(\frac{1}{2}u^2 + \frac{\gamma}{\gamma-1}\frac{P}{\rho})] = -\rho u\frac{d\phi}{dr} + \dot{E}(r), \tag{A.3}$$

where u, ρ, and P are the velocity, density and pressure of gas, respectively. γ is the ratio of specific heats taken to be 5/3. $\phi(r)$ is the gravitational potential given by

$$\frac{d\phi}{dr} = \frac{G[M_s(r) + M_d(r)]}{r^2}, \tag{A.4}$$

$$M_s(r) = \int_0^r 4\pi\rho_s(r)r^2 dr, \tag{A.5}$$

$$M_d(r) = \int_0^r 4\pi\rho_d(r)r^2 dr, \tag{A.6}$$

where $\rho_s(r)$ and $\rho_d(r)$ are the density distributions of stellar mass and dark matter, respectively. $\dot{m}(r)$ and $\dot{E}(r)$ are the mass and energy input rates per unit volume, which are assumed to be proportional to the density of stellar mass $\rho_s(r)$.

A.2 Galaxy modelling

A valid solution of the above *Euler* equations depends on the specific realization of the host galaxy, i.e., spatial distributions of the stars and dark matter, mass and energy input rates.

While many early models have applied the isothermal r^{-2} density distribution for the dark matter halo, we use the NFW profile (Navarro, Frenk and White 1996), in which density decreases following r^{-3} at large radii,

$$\rho_d(r) = \frac{\rho_{d0}}{\frac{r}{r_d}(1 + \frac{r}{r_d})^2}. \tag{A.7}$$

The boundary of galaxy is defined to be the virial radius R_v. We adpot $R_v = 250$ kpc, $q_d \equiv R_v/r_d = 15$, and the mass of dark matter M_d within R_v to be 90% of the total mass, i.e., $M_d + M_s$. ρ_{d0} can be replaced by an algebric combination of M_d and r_d. The mass and concentration of such a dark matter halo is consistent with results of numerical simulations (e.g., van den Bosch 2001). We note that the gas dynamics in the inner galactic regions, i.e., those monitored by typical X-ray observations, is not sensitive to the distribution of dark matter, since gravity in these regions is dominated by the stars.

For the stellar distribution, we adopt the Hernquist profile (Hernquist 1990)

$$\rho_s(r) = \frac{M_s}{2\pi} \frac{r_s}{r(r + r_s)^3}, \tag{A.8}$$

where r_s is the scale radius and M_s is the total stellar mass. The Hernquist profile, when projected, closely approximates the de Vaucouleurs's law, which is empirically used to describe the stellar surface brightness profile of elliptical galaxies and bulges (Hernquist 1990). We note that this profile predicts a cusp at the galactic center. Since the mass input follows the stellar distribution, the resultant central gas density is infinite. In reality, the existence of discrete X-ray sources almost always prevent us from directly probing the diffuse emission of gas near the very center of the host galaxy, therefore for simplicity we save our effort in relaxing a central cusp in the stellar distribution. In principle, by assuming a constant stellar mass-to-light ratio,

116

r_s can be related to R_e, the effective radius, within which half of the total stellar light lies, by the defining relation for R_e

$$\int_0^{R_e} 2\pi R \int_R^{R_v} 2\frac{\rho_s(r)r}{\sqrt{r^2 - R^2}} dr dR = \frac{1}{2}\int_0^{R_v} 2\pi R \int_R^{R_v} 2\frac{\rho_s(r)r}{\sqrt{r^2 - R^2}} dr dR. \qquad \text{(A.9)}$$

R_e is an observable, thus we can derive r_s by knowing R_e. In practice, we fit the 2MASS K-band radial intensity profile of the target galaxy with the projected Hernquist profile and derive r_s from the best-fit. Finally, M_s is determined from the color-dependent mass-to-light ratio of Bell & de Jong (2001) based on the K-band luminosity.

To complete the modelling, we also need to specify the colletive stellar mass loss rate $\dot{m}_0$ and the collective energy input rate $\dot{E}_0$ within the virial radius, so as to determine $\dot{m}(r)$ and $\dot{E}(r)$ (both assumed to be propotional to ρ_s) via relations

$$\int_0^{R_v} 4\pi r^2 \dot{m}(r) dr = \dot{m}_0, \qquad \text{(A.10)}$$

$$\int_0^{R_v} 4\pi r^2 \dot{E}(r) dr = \dot{E}_0. \qquad \text{(A.11)}$$

$\dot{m}_0$ and $\dot{E}_0$ are the two key parameters in our model.

For a given galaxy, there are also empirical methods to estimate $\dot{m}_0$ and $\dot{E}_0$. Knapp, Gunn and Wynn-Williams (1992) suggested the following relation as a direct measurement of the current mass loss rate from evolved stars in elliptical galaxies, using the 2.2 μm flux density

$$\dot{m} = 8 \times 10^{-4}(\frac{D}{\text{Mpc}})^2(\frac{S_{2.2}}{\text{Jy}}) \text{ M}_\odot \text{ yr}^{-1} = 2 \times 10^{-2}(\frac{L_K}{10^{10}L_{\odot,K}}) \text{ M}_\odot \text{ yr}^{-1}. \qquad \text{(A.12)}$$

The energy input consists of that from Type Ia SNe and that from stars, i.e., $\dot{E}_0 = \dot{E}_{0,\text{SN}} + \dot{E}_{0,\text{star}}$. By assuming a typical released energy of 10^{51} ergs for single SN

explosion,

$$\dot{E}_{0,\mathrm{SN}} = 1.1{\times}10^{40}(\frac{R_{\mathrm{SN}}}{0.035\mathrm{SNuK}})(\frac{L_K}{10^{10}L_{\odot,K}}) \text{ ergs s}^{-1}, \qquad (\mathrm{A}.13)$$

where R_{SN} is the observed Type Ia SNe rate in units of SNuK (one per $10^{10}L_{\odot,K}$ per 100 yr) for early-type galaxies at low redshifts (Mannucci 2005).

The stellar ejecta also carry mechanical energy obtained from the orbital motion of the progenitor star,

$$\dot{E}_{0,\mathrm{star}} = \frac{1}{2}\dot{m}_0\sigma^2 \approx 0.3{\times}10^{40}(\frac{\dot{m}_0}{0.1\ \mathrm{M}_\odot\ \mathrm{yr}^{-1}})(\frac{\sigma}{300\ \mathrm{km\ s}^{-1}})^2 \text{ ergs s}^{-1}, \qquad (\mathrm{A}.14)$$

where σ is the stellar velocity dispersion. Clearly, $\dot{E}_{0,\mathrm{SN}}$ is the dominant form of energy input.

Closely relevant is the metal-enrichment of gas predominantly by the SNe. Take the iron enrichment as an example. Nomoto, Thielemann and Yokoi (1984) calculated the Fe yield per Type Ia SN to be $0.7M_\odot$, about half of the total released mass. Assuming a complete mixture of the iron atoms with the gas, the iron abundance can be estimated as

$$Z_{\mathrm{Fe}} = Z_{\mathrm{Fe,star}} + 9.7(\frac{3.16{\times}10^{-5}}{[n_{\mathrm{Fe}}/n_{\mathrm{H}}]_\odot})(\frac{R_{\mathrm{SN}}}{0.035\mathrm{SNuK}}), \qquad (\mathrm{A}.15)$$

which is independent to the total stellar content. According to Grevesse & Sauval (1998), $[n_{\mathrm{Fe}}/n_{\mathrm{H}}]_\odot = 3.16{\times}10^{-5}$, thus by assuming that $Z_{\mathrm{Fe,star}}$ equals solar, Eq.(A.15) gives $Z_{\mathrm{Fe,gas}} = 10.7$.

The above estimates of $\dot{m}_0$ and $\dot{E}_0$, however, are averaged values obtained from a large sample of galaxies. The actual values for individial galaxies, while cannot be easily probed from direction observations, may deviate from the average significantly. Our aim of confronting the model with X-ray observations provides an alternative way to constrain the values of $\dot{m}_0$ and $\dot{E}_0$, such that the resultant model best fits the observed gas properties (see below).

A.3 Solution

To solve Eqs.(A.1) - (A.3), three boundary conditions, or three equivalent constrains on the variables, are generally needed. Given a natural assumption that the gas velocity is zero at the center, we have the first boundary condition,

$$u|_{r=0} = 0. \tag{A.16}$$

With a further assumption that the derivatives of velocity and temperature are finite at the center, Eq.(A.3) and (A.16) require that

$$kT_0 \equiv kT|_{r=0} = \mu_g m_{\rm H} \frac{P}{\rho}\Big|_{r=0} = \mu_g m_{\rm H} \frac{\gamma - 1}{\gamma} \frac{\dot{E}_0}{\dot{m}_0}, \tag{A.17}$$

where μ_g is the mean molecular weight of gas taken to be 0.6, $m_{\rm H}$ and k are of their conventioanl usages.

Now it is convenient to introduce a dimensionless variable, the Mach number $M \equiv u/c_s$, where $c_s \equiv (\gamma P/\rho)^{1/2}$ is the sound speed of gas. With Eq.(A.16) and (A.17), one can show that the *Euler* equations reduce to a first order differential equation of the Mach number

$$\frac{dM^2}{dr} = \frac{M^2}{M^2 - 1}(1 + \frac{\gamma - 1}{2}M^2)g(r, M), \tag{A.18}$$

$$g(r, M^2) = \frac{4}{r} - \frac{\gamma + 1}{\gamma - 1}\frac{\frac{dW}{dr}}{L - W} - (1 + \gamma M^2)[\frac{\frac{dF}{dr}}{F} + \frac{\frac{dL}{dr}}{L - W}],$$

where

$$F(r) = \int_0^r 4\pi \dot{m}(r)r^2 dr, \tag{A.19}$$

$$L(r) = \int_0^r 4\pi \dot{E}(r)r^2 dr, \tag{A.20}$$

$$W(r) = \int_0^r F(r)\frac{d\phi}{dr}dr. \tag{A.21}$$

In general the right-hand side of Eq.(A.18) is singular when $M = 1$. Correspondingly, the radius $r = r_c$ at which $M = 1$ is called *sonic radius* or *critical radius*. A

119

wind solution requires that the gas flow smoothly passes through the sonic radius. This provides a third boundary condition to the solution,

$$g(r, M)|_{r_c} = 0, \qquad\qquad (A.22)$$

so that the right-hand side of Eq.(A.18) remains regular when $M = 1$.

To derive the wind solution, the location of the sonic radius is first found by solving Eq.(A.22), which is simply an algebric equation of r. Then *L'Hospita*'s rule is applied to obtain the derivative of M at r_c. Finally, a wind solution is found by integrating Eq.(A.18) starting from r_c inward to the center and from outard to the virial radius. An adaptively stepping fifth order Runge-Kutta method is used when porforming the numerical solution. Fig. A.1 shows a representative solution of the wind model for M104.
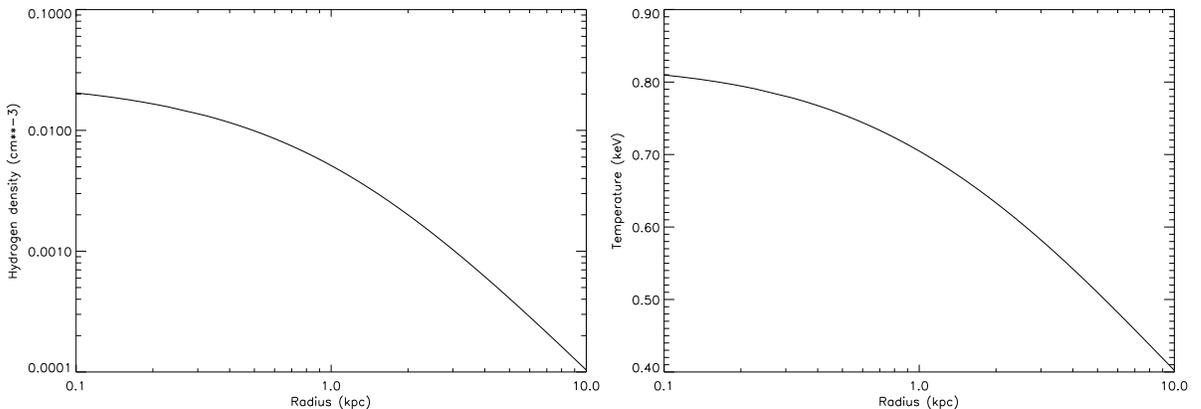
Figure A.1 Representative radial distributions of gas density and temperature within 10 kpc from the center of M104, calculated from the galactic wind model.

A.4   Application to X-ray observations

In principle, giving the spatial distributions of gas density and temperature would completely determine the thermal emission of the gas, provided that the emission mechanism is known, e.g., emission from thermal plasma in collisional ionization

equilibrium (CIE). Correspondingly, in case that our model is a good approximation of the actual gas dynamics, we expect that the observed X-ray emission be well fitted by the model predictions.

A practical methodology of studying the X-ray emission is to perform spatially-resolved spectral analysis. Below we develop procedures to generate X-ray spectra based on the spatial distributions of gas density and temperatur given by a certain solution of the model.

According to spherical symmetry, the spectrum of the gas from within a projected annular region with inner to outer galactocentric radii $R_1 - R_2$ is given by

$$S_\nu(R_1, R_2) = \frac{1}{4\pi D^2} \int_{R_1}^{R_2} 2\pi R \int_R^{R_v} 2\frac{n_e(r)n_H(r)\Lambda_\nu[T(r), Z(r)]r}{\sqrt{r^2 - R^2}} dr dR, \qquad (A.23)$$

where $\Lambda_\nu(T, Z)$ is the CIE emissivity of optically thin plasma with temperature T and abundance Z. We shall neglect the possible dependency of Z on the radius.

Since the model spectra are to be used to fit the observed spectra, it is convenient to make use of the XSPEC software to generate model spectra. There are two ways to generate an XSPEC implementable spectrum model: one is in analytic format; the other is in tabulated format[1]. While the tabulated format requires pre-calculated model spectra according to grids of model paramters, we adopt the analytic format to implement our spectrum model, by which on-the-fly spectrum calculation is performed by summing up spectra of indivial volumes, i.e., $S_\nu = \Sigma s_{\nu,i} = \Sigma n_{e,i} n_{H,i} V_i \Lambda_\nu(T_i)$, where $n_{e,i}$, $n_{H,i}$ and T_i are constant within volume V_i and are to be supplied. Using the analytic format, we can conveniently generate model spectra for arbitary projected radii R_1 and R_2, with the price of more computational effort on-the-fly. We perform the following steps to make the spectrum calculation effective. We first divide the sphere with inner to outer radii $R_1 - R_v$ into a number of thin shells, with radius

---

[1]http://heasarc.gsfc.nasa.gov/docs/xanadu/xspec/manual/node59.html

r_i and thickness Δr. Within each shell, the volume V_i contributes to the projected spectrum is the proportion of the shell overlaid by the projected annular region. V_i as a function of R_1, R_2, Δr and r_i can be expressed analytically as,

$$V_i = \frac{4\pi}{3}(h_{21}^{3/2} + h_{12}^{3/2} - h_{11}^{3/2} - h_{22}^{3/2}),$$

$$h_{jk} = max\{h_j^2 - R_k^2, 0\}, \quad j, k = 1, 2 \qquad (A.24)$$

$$h_1 = r_i, \; h_2 = r_i + \Delta r.$$

The gas density and temperature within each shell are constant, i.e., values provided by the wind solution at $r = r_i$. The MEKAL model in XSPEC is made used on the fly to calculate the emissivity $\Lambda_\nu(T_i)$. Individual spectrum $s_{\nu,i}$ is then calculated and the total spectrum is obtained by summing up all $s_{\nu,i}$.

BIBLIOGRAPHY

[1] Allen S.W., Dunn R.J.H., Fabian A.C., Taylor G.B., Reynolds C.S. 2006, MN-RAS, 372, 21

[2] Almy, R. C., McCammon, D., Digel, S. W., Bronfman, L., & May, J. 2000, ApJ, 545, 290

[3] Athanassoula E. & Beaton R.L. 2006, MNRAS, 370, 1499

[4] Bajaja E., Hummel E., Wielebinski R., Dettmar R.-J., 1988, A&A, 35

[5] Barmby P., et al. 2006, ApJ, 650, L45

[6] Beaton, R. L., et al. 2007, ApJ, 658, L91

[7] Bell E.F., de Jong R.S., 2001, ApJ, 550, 212

[8] Bender R., et al. 2005, ApJ, 631, 280

[9] Benson A.J., Bower R.G, Frenk C.S., White S.D.W., 2000, MNRAS, 314, 557

[10] Binette L., Magris C.G., Stasinśka G., Bruzual A.G. 1994, A&A, 292, 13

[11] Block D.L., et al. 2006, Nature, 443, 832

[12] Bogdán Á., & Gilfanov M. 2008, MNRAS, 388, 56

[13] Bondi H. 1952, MNRAS, 112, 195

[14] Bottema R., 1989, A&A, 225, 358

[15] Braun R., Thilker D.A., 2004, A&A, 417, 421

[16] Bregman J.N., 1980, ApJ, 237, 280

[17] Bregman J.N., Houck J.C., 1997, ApJ, 485, 159

[18] Bressan A., Granato G.L., Silva L. 1998, A&A, 311, 425

[19] Bridges T.J., Ashman K.M., Zepf S.E., Carter D., Hanes D.A., Sharples R.M., Kavelaars J.J., 1997, MNRAS, 284, 376

[20] Brinks E. 1984, Ph.D. Thesis, University of Leiden

[21] Brown T.M., Ferguson H.C., Davidsen A.F. 1996, ApJ, 472, 327

[22] Brown T.M., Ferguson H.C., Stanford S.A., Deharveng J.-M. 1998, 504, 113

[23] Burstein D., Bertola F., Buson L.M., Faber S.M., Lauer T.R. 1988, ApJ, 328, 440

[24] Buzzoni A., Gariboldi G., Mantegazza L. 1992, AJ, 103, 1814

[25] Cardelli J.A., Clayton G.C., Mathis J.S. 1989, ApJ, 345, 245

[26] Cecil G., Bland-Hawthorn J., Veilleux S., 2002, ApJ, 576, 745

[27] Chang P., Murray-Clay R., Chiang E., Quataert E. 2007, ApJ, 668, 236

[28] Chaves T., Irwin J., 2001, ApJ, 557, 646

[29] Chevalier R.A., Clegg A.W., 1985, Nature, 317, 44

[30] Ciardullo, R., Rubin V.C., Jacoby G.H., Ford H.C., Ford W.K.Jr. 1988, AJ, 95, 438

[31] Ciotti L., Pellegrini S., Renzini A., D'Ercole A., 1991, ApJ, 376, 380

[32] Colbert E.J.M., Heckman T.M., Ptak A.F., Strickland D.K., Weaver K.A., 2004, ApJ, 602, 231

[33] Cowie L.L. & McKee C.F. 1977, ApJ, 211, 135

[34] Crane P.C., Dickel J.R., Cowan J.J. 1992, ApJ, 390, L9

[35] Dahlem M., Weaver K.A., Heckman T.M., 1998, ApJS, 118, 401

[36] David, L. P., Jones, C., Forman, W., Vargas, I. M., & Nulsen, P. 2006, ApJ, 653, 207

[37] del Burgo C., Mediavilla E., Arribas S. 2000, ApJ, 540, 741

[38] Devereux N.A., Price R., Wells L.A., Duric N. 1994, AJ, 108, 1667

[39] Dickey J.M., Lockman F.J., 1990, ARA&A, 28, 215

[40] Di Stefano R., Kong A.K.H., VanDalfsen M.L., Harris W.E., Murray S. S., Delain K.M., 2003, ApJ, 599, 1067

[41] Ellis, S.C., O'Sullivan E., 2006, MNRAS, 367, 627

[42] Englmaier P., & Shlosman I. 2000, ApJ, 528, 677

[43] Ford H.C., Hui X., Ciardullo R., Jacoby G.H., Freeman K.C., 1996, ApJ, 458, 455

[44] Garcia M., et al. 2005, ApJ, 632, 1042

[45] Gil de Paz A., et al. 2007, ApJS, 173, 185

[46] Gilfanov M., 2004, MNRAS, 349, 146

[47] Goldsmith D.W., Habing H.J., Field G.B. 1969, ApJ, 158, 173

[48] Gordon K.D., et al. 2006, ApJ, 638, L87

[49] Goudfrooij P., & de Jong T. 1995, A&A, 298, 784

[50] Grevesse N., Sauval A.J. 1998, Space Science Reviews, 85, 161

[51] Hameed S., Devereux N. 2005, AJ, 129, 2597

[52] Han Z., Podsiadlowski Ph., Lynas-Gray A.E. 2007, MNRAS, 380, 1098

[53] Hernquist, L., 1990, ApJ, 356, 359

[54] Hjellming R.M. & Smarr L.L. 1982, ApJ, 257, L13

[55] Ho L.C., Filippenko A.V., Sargent W.L.W. 1997, ApJS, 112, 315

[56] Ho L.C., Terashima Y., Ulvestad J.S. 2003, ApJ, 589, 783

[57] Hoernes P., Beck R., Berkhuijsen E.M. 1998, IAUS, 184, 351

[58] Humphrey P.J., Buote D.A., 2006, 639, 136

[59] Irwin J.A., Sarazin C.L., Bregman J.N., 2002, ApJ, 570, 152

[60] Irwin J.A., Athey A.E., Bregman J.N., 2003, ApJ, 587, 356

[61] Irwin J., Chaves T., 2003, ApJ, 585, 268

[62] Irwin J., Saikia D.J., English J., 2000, AJ, 119, 1592 .D., 2001, A&A, 377, 759

[63] Jacoby G.H., Ford H., Ciardullo, R. 1985, ApJ, 290, 136

[64] Jarrett T.H., Chester T., Cutri R., Schneider S., Huchra J.P., 2003, AJ , 125, 525

[65] Ji L., Wang Q.D., Kwan, J., 2006, MNRAS, 372, 497

[66] Kennicutt R.C., 1998, ARA&A, 36, 189

[67] Kim D.-W., Fabbiano G., 2003, ApJ, 586, 826

[68] King I.R., et al. 1992, ApJ, 397, L35

[69] Knapen J.H., Hes R., Beckman J.E., Peletier R.F., 1991, A&A, 241, 42

[70] Knapen J.H. 2005, A&A, 429, 141

[71] Knapp G.R., Gunn J.E., Wynn-Williams C.G., 1992, ApJ, 399, 76

[72] Lauer T.R., et al. 1993, AJ, 106, 1436

[73] Lauer T.R., Faber S.M., Ajhar E.A., Grillmair C.J., Scowen P.A. 1998, AJ, 116, 2263

[74] Lehnert M.D., Heckman T.M., Weaver K.A. 1999, ApJ, 523, 575

[75] Li A. & Draine B.T. 2001, ApJ, 554, 778

[76] Li J., Kastner J.H., Prigozhin G.Y., Schulz N.S. 2003, 590, 586

[77] Li Z., Wang Q.D., Irwin J.A., Chaves T., 2006, MNRAS, 371, 147 (Paper I)

[78] Li Z., Wang Q.D., Hameed, S. 2007, MNRAS, 376, 960 (Paper II)

[79] Li Z., & Wang Q.D. 2007, ApJ, 688, L39 (Paper III)

[80] Li Z., Wang Q.D., Wakker B.P. 2008, submitted (Paper IV)

[81] Loewenstein, M., & Mathews, W., 1987, ApJ, 319, 614

[82] Lonsdale C., Helou G., Good J.C., 1989, Cataloged Galaxies and Quasars observed in the IRAS Survey, Jet Propulsion Laboratory

[88] Mannucci F., Della Valle M., Panagia N., Cappellaro E., Cresci G., Mai olino R., Petrosian A., Turatto M., 2005, A&A, 433, 807

[84] Mathews W.G., Baker J.C., 1971, ApJ, 170, 241

[85] Mathews W.G., Brighenti F. 2003, ARA&A, 41, 191

[86] Macchetto F., et al. 1996, A&AS, 120, 463

[87] Maciejewski W. 2004, MNRAS, 354, 892

[88] Mannucci F., et al. 2005, A&A, 433, 807

[89] McKee C.F. & Cowie L.L. 1975, ApJ, 195, 715

[90] McKee C.F. & Cowie L.L. 1977, ApJ, 215, 213

[91] Melchior A.-L., Viallefond F., Guélin M., Neininger N. 2000, MNRAS, 312, L29

[92] Moretti A., Campana S., Lazzati D., Tagliaferri G., 2003, ApJ, 588, 696

[93] Morris M. 1993, ApJ, 408, 496

[94] Narayan R. & Yi I. 1995, ApJ, 452, 710

[95] Navarro J.F., Frenk C.S., White S.D.M., 1996, ApJ, 462, 563

[96] Nayakshin S. & Sunyaev R. 2007, MNRAS, 377, 1647

[97] Nevalaine J., Markevitch M., Lumb D.H., 2005, ApJ, 629, 172

[98] Nieten, Ch., et al. 2006, A&A, 453, 459

[99] Nomoto K., Thielemann F.K., Yokoi K., 1984, ApJ, 286, 644

[100] O'Sullivan E., Ponman T., Collins R.S., 2003, MNRAS, 340, 1375

[101] Ott M., Whiteoak J.B., Henkel C., Wilebinski R., 2001, A&A, 372, 463

[102] Pellegrini S., Baldi A., Fabbiano G., Kim D.-W., 2003, ApJ, 597, 175

[103] Pedersen K., Rasmussen J., Sommer-Larsen J., Toft S, Benson A.J., Bower R.G. 2006, New Astronomy Reviews, 11, 465

[104] Quillen A.C., Frogel J.A., Kenney, J.D.P., Pogge R.W., Depoy D.L. 1995, ApJ, 441, 549

[105] Rasmussen J. 2007, New Astronomy Reviews, 51, 99

[106] Regan M.W. & Mulchaey, J.S. 1999, AJ, 117, 2676

[107] Revnivtsev, M., Sazonov, S., Gilfanov, M., Churazov, E., & Sunyaev, R. 2006, A&A, 452, 169

[108] Revnivtsev M., Churazov E., Sazonov S., Forman W., Jones C. 2007, A&A, 473, 783

[109] Rubin V.C., Burstein D., Ford W.K. Jr., Thonnard N., 1985, ApJ, 289, 81

[110] Rubin V.C. & Ford W.K.Jr. 1971, ApJ, 170, 25

[111] Sakamoto K., Okumura S.K., Ishizuki S., Scoville N.Z. 1999, ApJ, 525, 691

[112] Sanders D.B., Mazzarella J.M., Kim D.-C., Surace J.A., Soifer B.T., 2003, AJ, 126, 1607

[113] Sarzi M., Allard E.L., Knapen J.H., Mazzuca L.M. 2007, MNRAS, 380, 949

[114] Sato, S., Tawara Y., 1999, ApJ, 514, 765

[115] Sazonov S., Revnivtsev M., Gilfanov M., Churazov E., Sunyaev R. 2006, A&A, 450, 117

[116] Sembach K.R. et al. 2003, ApJS, 146, 165

[117] Shirey R., et al. 2001, A&A, 365, L195

[118] Shull J.M. 1979, ApJ, 234, 761

[119] Shull J.M. & McKee C. 1979, ApJ, 227, 131

[120] Singh K.P., White N.E., Drake S.A. 1996, ApJ, 456, 766

[121] Slavin, J., Shull, J.M.,& Begelman, M.C. 1993, ApJ, 407, 83

[122] Sparks W.B., Macchetto F., Golombek D. 1989, ApJ, 345, 153

[123] Snowden S.L., et al. 1995, ApJ, 454, 643

[124] Snowden, S. L., et al. 1997, ApJ, 485, 125

[125] Spitzer L.Jr. 1962, *Physics of Fully Ionized Gases* (New York: Interscience)

[126] Stark A.A. & Binney J. 1994, ApJ, 426, L31

[127] Strickland D.K., Heckman T.M., Weaver K.A., Dahlem M., 2000, AJ, 120, 2 965

[128] Strickland D.K., Heckman T.M., Weaver K.A., Hoopes C.G., Dahlem M., 200 2, ApJ, 568, 689

[129] Strickland D.K., Heckman T.M., Colbert E.J.M., Hoopes C.G., Weaver K.A. , 2004a, ApJS, 151, 193

[130] Strickland D.K., Heckman T.M., Colbert E.J.M., Hoopes C.G., Weaver K.A., 2004b, ApJ, 606, 829

[131] Takahashi, H., Okada, Y., Kokubun, M., & Makishima, K. 2004, ApJ, 615, 242

[132] Tang S., Wang Q.D., 2005, ApJ, 628, 205

[133] Thilker D.A., et al. 2005, ApJ, 619, L79

[134] Toft S., Rasmussen J., Sommer-Larsen J., Pedersen K., 2002, MNRAS, 335, 799

[135] Tremaine S. 1995, AJ, 110, 628

[136] Trinchieri G., Noris L., di Serego Alighieri S. 1997, A&A, 326, 565

[137] Tsunemi H., et al. 2001, ApJ, 554, 496

[138] Tüllmann R., Pietsch W., Rossa J., Breitschwerdt D., Dettmar R.-J., 2006, A&A, 448, 43

[139] van den Bosch, F. C., 2001, MNRAS, 327, 1334

[140] van Dokkum P.G., & Franx M. 1995, AJ, 110, 2027

[141] Voss, R., Gilfanov, M. 2007, A&A, 468, 49

[151] Wada K. 2004, in Carnegie Observatories Astrophysics Series, Vol. 1: Coevolution of Black Holes and Galaxies, ed. L.C. Ho (Cambridge: Cambridge Univ. Press), 187

[143] Wagner S.J., Dettmar R.-J., Bender R., 1989, A&A, 215, 243

[144] Wakker B.P. et al., 2003, ApJS, 146, 1

[145] Wakker B.P. 2006, ApJS, 163, 282

[146] Walterbos R.A.M. & Gräve R. 1985, A&A, 150, L1

[147] Walterbos R.A.M. & Kennicutt R.C.Jr. 1998, A&A, 198, 61

[148] Wang, Q. D. 1997, in IAU Colloq. 166, The Local Bubble and Beyond, ed. D. Breitschwerdt, M. Freyberg, & J. Trümper (Springer: Berlin), 503

[149] Wang Q.D., Immler S., Walterbos R., Lauroesch J. T., Breitschwerdt D.,2001, ApJ, 555, L99

[150] Wang Q.D., Chaves T., Irwin J., 2003, ApJ, 598, 969

[151] Wang Q.D., 2004, ApJ, 612, 159

[152] Wang Q.D., 2005, ASPC, 331, 329

[153] Wang, Q. D. 2007, EAS Publications Series, 24, 59

[154] White R.E., Chevalier R.A., 1983, ApJ, 275, 69

[155] Willingale R., Hands A.D.P., Warwick R.S., Snowden S.L., Burrows D.N., 2003, MNRAS, 343, 995

[156] Wolfire, M. G., McKee, C. F., Hollenbach, D., & Tielens, A. G. G. M. 1995, ApJ, 453, 673

[157] Wyder T.K., et al. 2005, ApJ, 619, L15

[158] Young P.J., 1976, AJ, 81, 807